

AD-A182 021

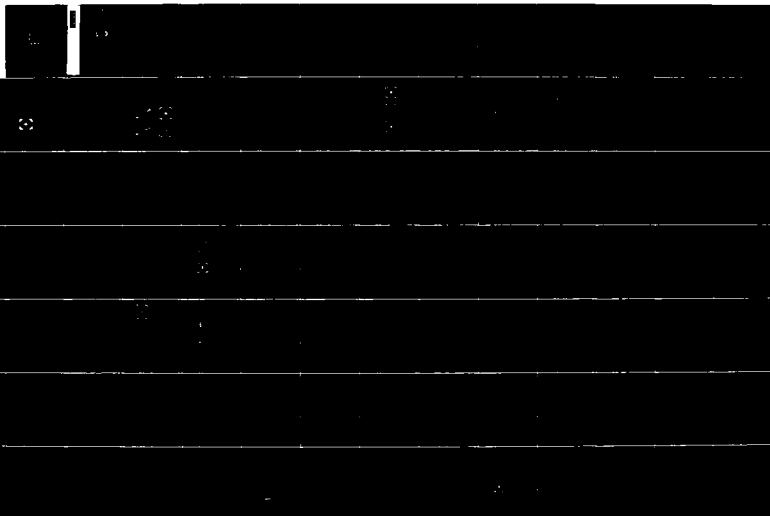
RECIRCULATING ACCELERATOR STUDIES (U) MISSION RESEARCH
CORP ALBUQUERQUE NM I P HUGHES ET AL. 02 JUN 87
AMRC-R-922 N00014-84-C-0078

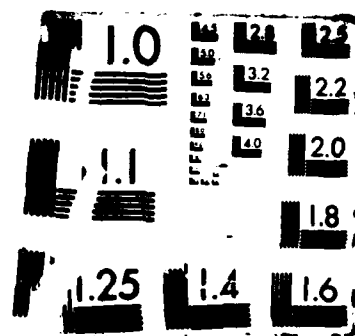
1/2

UNCLASSIFIED

F/G 20/7

NL





AD-A182 021

DTIC FILE COPY

AMRC-R-922
Copy 17

(12)

FINAL REPORT

RECIRCULATING ACCELERATOR STUDIES

Thomas P. Hughes
Brendan B. Godfrey

June 1987

DTIC
ELECTE
JUN 22 1987
S D

Prepared for:

OFFICE OF NAVAL RESEARCH
800 North Quincy Street
Arlington, Virginia 22217

Under:

Contract N00014-84-C-0078

Prepared by:

MISSION RESEARCH CORPORATION
1720 Randolph Road, S.E.
Albuquerque, New Mexico 87106

APPROVED FOR PUBLIC RELEASE; UNLIMITED DISTRIBUTION

87 6 19 027

UNCLASSIFIED

SECURITY CLASSIFICATION OF THIS PAGE

AD-A182021

REPORT DOCUMENTATION PAGE

1a. REPORT SECURITY CLASSIFICATION Unclassified			1b. RESTRICTIVE MARKINGS		
2a. SECURITY CLASSIFICATION AUTHORITY			3. DISTRIBUTION/AVAILABILITY OF REPORT Approved for public release; distribution unlimited.		
2b. DECLASSIFICATION/DOWNGRADING SCHEDULE			4. PERFORMING ORGANIZATION REPORT NUMBER(S) AMRC-R-922		
6a. NAME OF PERFORMING ORGANIZATION Mission Research Corporation		6b. OFFICE SYMBOL (if applicable) AMRC		5. MONITORING ORGANIZATION REPORT NUMBER(S)	
6c. ADDRESS (City, State, and ZIP Code) 1720 Randolph Road, S.E. Albuquerque, New Mexico 87106			7a. NAME OF MONITORING ORGANIZATION		
8a. NAME OF FUNDING/SPONSORING ORGANIZATION Office of Naval Research		8b. OFFICE SYMBOL (if applicable)		7b. ADDRESS (City, State, and ZIP Code)	
8c. ADDRESS (City, State, and ZIP Code) 800 North Quincy Street Arlington, Virginia 22217			9. PROCUREMENT INSTRUMENT IDENTIFICATION NUMBER N00014-84-C-0078		
10. SOURCE OF FUNDING NUMBERS			PROGRAM ELEMENT NO.		
			PROJECT NO.		
11. TITLE (Include Security Classification) Final Report -- Recirculating Accelerator Studies			TASK NO.		
12. PERSONAL AUTHOR(S) Thomas P. Hughes and Brendan B. Godfrey			WORK UNIT ACCESSION NO.		
13a. TYPE OF REPORT Final		13b. TIME COVERED FROM 1Jan85 to 31Mar87		14. DATE OF REPORT (Year, Month, Day) 1987 June 02	
15. PAGE COUNT 97					
16. SUPPLEMENTARY NOTATION					
17. COSATI CODES			18. SUBJECT TERMS (Continue on reverse if necessary and identify by block number)		
FIELD	GROUP	SUB-GROUP	Modified Betatron		
			Negative Mass Instability		
			Stellatron		
			Quadrupole Focusing		
			Solenoidal Lens Betatron		
19. ABSTRACT (Continue on reverse if necessary and identify by block number)					
<p>Results of stability calculations for three types of high current betatron (modified betatron, stellatron, solenoidal lens betatron) are presented. For the modified betatron, stability is strongly dependent on the internal poloidal rotation frequency of the beam. When this frequency is close to zero, high-mode numbers are easily stabilized. For the NRL betatron parameters, the beam is predicted to become unstable when it accelerates above 1 MeV. For a 10 kA beam, several kiloamps remain circulating after saturation of the instability. High energy simulations of the modified betatron show saturation without loss of current.</p> <p>Calculations for the UCL stellatron show that background ions have a strong stabilizing effect on the negative-mass instability, due to increased transverse focusing. The energy threshold for onset of instability agrees with experimental observation.</p>					
20. DISTRIBUTION/AVAILABILITY OF ABSTRACT <input type="checkbox"/> UNCLASSIFIED/UNLIMITED <input checked="" type="checkbox"/> SAME AS RPT. <input type="checkbox"/> DTIC USERS			21. ABSTRACT SECURITY CLASSIFICATION Unclassified		
22a. NAME OF RESPONSIBLE INDIVIDUAL			22b. TELEPHONE (Include Area Code)		22c. OFFICE SYMBOL

DD FORM 1473, 84 MAR

83 APR edition may be used until exhausted.
All other editions are obsolete.SECURITY CLASSIFICATION OF THIS PAGE
UNCLASSIFIED

19. Concluded

An electromagnetic three-wave interaction is found to occur in the stellatron. Its growth rate can be very large, but parameters can be chosen to move it to short wavelengths where thermal effects should stabilize it.

An analytic dispersion relation for the solenoidal lens betatron is obtained using a multiple-length-scale averaging method. The ~~UMA~~ betatron is predicted to be stable at and slightly above its injection energy. Simulation for higher energy show a strong instability which saturates with some loss of current. Simulations of 10 kA beams in a solenoidal lens betatron show similar results, suggesting that most of the current can survive the instability.

CONTENTS

<u>Section</u>		<u>Page</u>
I	INTRODUCTION	1
II	MODIFIED BETATRON ACCELERATOR	2
	1. NEGATIVE-MASS INSTABILITY ON A COLD BEAM	2
	2. EFFECT OF SPREAD IN CIRCULATION FREQUENCIES	4
	3. BEAM STABILITY AT HIGH ENERGIES	12
	4. RESONANCES IN THE MODIFIED BETATRON AT LOW ENERGIES	18
III	STELLATRON ACCELERATOR	23
	1. RESULTS RELATED TO THE UCI STELLATRON	23
	2. ELECTROMAGNETIC INSTABILITY DUE TO THE HELICAL FIELD	25
IV	SOLENOIDAL LENS BETATRON	29
	1. BEAM TRANSPORT	29
	2. BEAM STABILITY IN THE IAPBT BETATRON	32
	3. HIGH CURRENT BEAM STABILITY	37
V	CONCLUSIONS	40
	REFERENCES	42
	APPENDIX A. ELECTROMAGNETIC INSTABILITY IN A QUADRUPOLE-FOCUSING ACCELERATOR	A-1
	APPENDIX B. EQUILIBRIUM AND STABILITY PROPERTIES OF THE SOLENOIDAL LENS BETATRON	B-1
	APPENDIX C. STABILITY OF THE SOLENOIDAL LENS BETATRON	C-1
	APPENDIX D. PUBLICATIONS, TECHNICAL REPORTS, CONFERENCE PROCEEDINGS, AND PRESENTATIONS WRITTEN UNDER THIS CONTRACT	D-1



Accession For	
NTIS CRA&I	<input checked="" type="checkbox"/>
DTIC TAB	<input type="checkbox"/>
Unannounced	<input type="checkbox"/>
Justification	
By	
Distribution/	
Availability Codes	
Dist	Avail and/or Special
A-1	

ILLUSTRATIONS

<u>Figure</u>		<u>Page</u>
1	Growth rates of the negative-mass instability for parameters typical of the NRL betatron	3
2	Plot of the two sides of Eq. (3) for a 10 kA, $\gamma = 12$ beam	6
3	Energy histories of the $\ell = 4$ negative-mass instability on a 10 kA, $\gamma = 12$ beam with initial radius $r_b = 2$ cm in (a) and $r_b = 3.5$ cm in (b)	7
4	Particle plots taken during the nonlinear stages of the simulations shown in Fig. 3. For (a), the initial beam radius is $r_b = 2$ cm and in (b), the initial beam radius is $r_b = 3.5$ cm	8
5	Energy histories and particle plots for simulations of the $\ell = 20$ negative mass instability on a 10 kA, $\gamma = 12$ beam. The initial beam radius is 1.7 cm in (a), 2 cm in (b) and 3 cm in (c)	10
6	Plot of the two sides of Eq. (3) for parameters typical of the NRL betatron. In (a) the beam parameters are 3 kA, $\gamma = 7$, and in (b) the parameters are 1 kA and $\gamma = 4$. In each case, a 2.5 kG toroidal field is assumed	11
7	Instability growth rates of the $\ell = 20$ mode for a 10 kA beam in a 1 kG toroidal field	13
8	Particle plots illustrating the nonlinear saturation of the $\ell = 20$ instability on a $\gamma = 50$ beam	14
9	Energy history of the $\ell = 20$ instability on a $\gamma = 20$ beam with an initial radius of 1 cm, showing two distinct slopes	16
10	Nonlinear state of the $\ell = 20$ instability on a $\gamma = 20$ beam with an initial radius of 1 cm	17
11	Plot of betatron tunes versus energy for typical NRL betatron parameters, showing low integer resonances	20
12	Amplification of betatron oscillations due to an $\ell = 2$ resonance in a 2 kA, $\gamma = 3$ beam. In (a), the error in the vertical field is 1%, and in (b) the error is 4%	21

ILLUSTRATIONS (Concluded)

<u>Figure</u>		<u>Page</u>
13	Growth rates of the $\ell = 20$ negative-mass instability for typical stellatron parameters. The solid line is for a stellatron field such that the helical field parameter $\epsilon = 0.7$, while the dashed line is for $\epsilon = 0$	24
14	Growth rates of the $\ell = 1$ negative-mass instability for parameters typical of the UCI stellatron, illustrating the large effect of ion focusing on the growth rate and transition energy	26
15	Qualitative picture of the modes which interact to produce the 3-wave electromagnetic instability in a stellatron	27
16	Particle orbit in the UNM solenoidal-lens betatron	31
17	Growth rates of the $\ell = 5$ negative mass instability in the UNM solenoidal-lens betatron	33
18	Particle plot taken during the nonlinear stage of the $\ell = 15$ negative-mass instability for UNM betatron parameters	36
19	Comparison of simulation growth rates for the $\ell = 20$ mode on a 10 kA beam with analytic growth rates obtained for a conventional betatron (dashed line) and by extrapolation of the smoothed focusing result (solid line)	38
20	Nonlinear development of the $\ell = 20$ negative mass instability on a 10 kA beam in a solenoidal lens betatron. In (a), the beam energy is $\gamma = 7$ and in (b), $\gamma = 12$	39

I. INTRODUCTION

For about the past six years, high-current betatrons of various designs have been the subject of experimental and theoretical investigations. This interest stems from the potential for compact, high-power beam generation which these machines offer.

To operate a high-current betatron successfully, one must be able to inject the beam onto a closed, recirculating orbit, and maintain beam stability for the duration of the acceleration cycle. The latter may vary from tens of microseconds to several milliseconds. Depending on the application, it may then be necessary to extract the beam from the device.

During the period of our contract with the Office of Naval Research (01 November 1983 - 31 March 1987), we have concentrated on the question of beam behavior after injection, because this behavior determines such key parameters as the maximum operating current, and the length of the acceleration cycle. During the period 01 November 1983 - 31 December 1984, we developed the analytic and computational tools to study the equilibrium and stability of the circulating electron ring. This work was described in detail in Ref. 1, and will be referred to as needed. In the period 01 January 1985 - 31 March 1987, which is covered in this report, our emphasis was on applying these methods to experimental machines currently in operation.

The experiments for which we have performed specific calculations are the Modified Betatron Accelerator at the Naval Research Laboratory [2], the Stellantron at UC Irvine [3], and the Solenoidal Lens Betatron at the University of New Mexico [4]. This report is organized into three main sections describing the results for each of these devices. Publications, Conference Proceedings and Presentations, and Technical Reports written during this contract are listed in Appendix D.

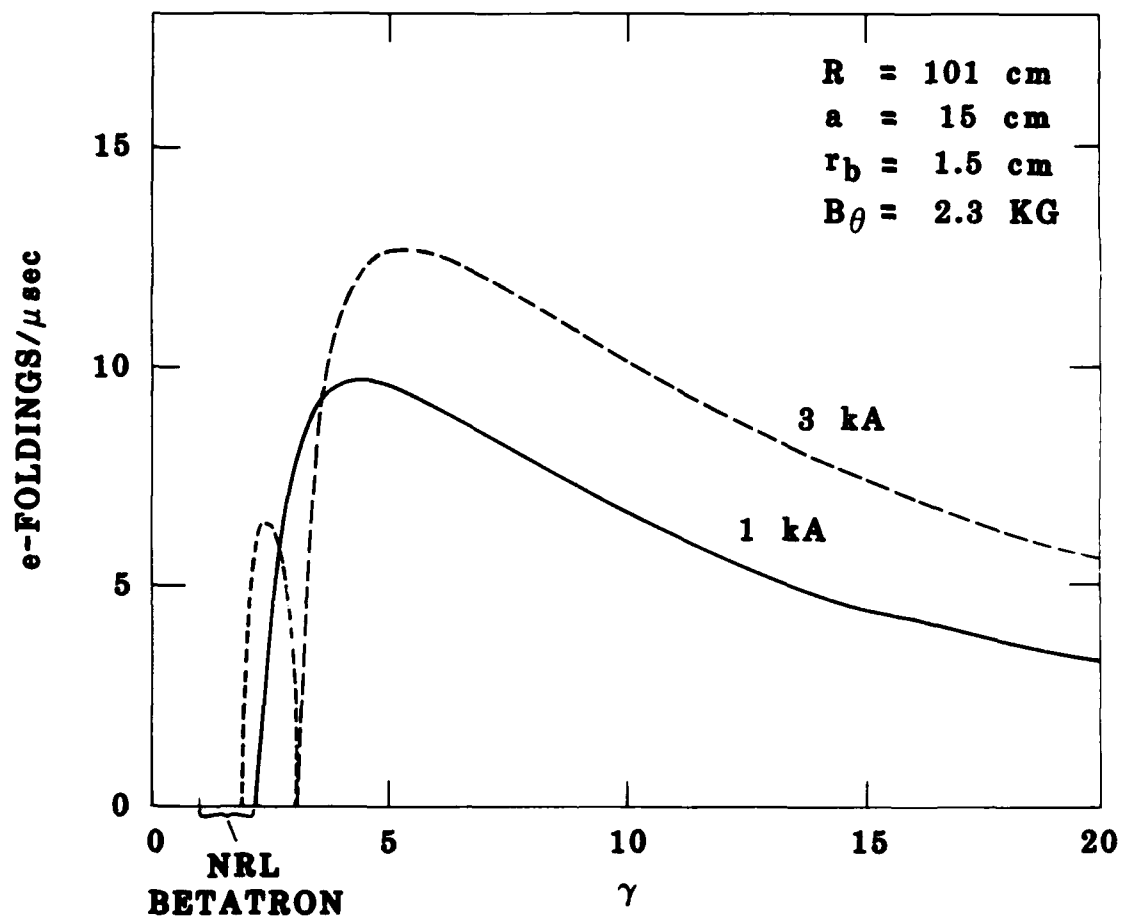
II. MODIFIED BETATRON ACCELERATOR

1. NEGATIVE-MASS INSTABILITY ON A COLD BEAM

The modified betatron adds a toroidal magnetic field to the conventional betatron configuration. In this way, the space-charge limit on the confinable current is considerably increased. The most important collective instability for this device is the negative-mass instability, which causes toroidal clumping and transverse kinking of the beam. In Ref. 1, we derived a dispersion relation for this instability which agrees accurately with cold-beam numerical simulations. In Fig. 1, this dispersion relation is applied to the parameters of the modified betatron at NRL. The present status of this machine is that a 1 kA, 0.8 MeV beam has been successfully trapped in the combined vertical and toroidal magnetic fields for periods up to 10 μ sec. During this time, the beam executes on the order of 500 major revolutions. The observed stability is in agreement with the prediction of Fig. 1. Due to space-charge depression of the injected beam energy, the actual value of the relativistic factor γ for the circulating ring is about 1.6 [5]. This puts the beam below the "negative-mass transition energy", which is given by

$$\gamma_t = \left(\frac{4\nu R^2}{a^2} \right)^{1/3} \quad (1)$$

where ν is Budker's parameter, R is the major radius, and a is the torus minor radius. This gives $\gamma_t = 2.1$ for a 1 kA beam, in agreement with Fig. 1. In the absence of stabilizing measures, the beam will become unstable above this energy. The peak growth for the $\ell = 1$ instability occurs around $\gamma = 4$, and the mode would become nonlinear in a time on the order of 1 μ sec. We have not simulated the nonlinear development of the negative-mass instability for a 1 kA beam. For 10 kA beams, our simulations show strong kinking of the beam at low energies leading to considerable current loss (see Fig. 4a below, and Ref. 6).



VG-740

Figure 1. Growth rates of the negative-mass instability for parameters typical of the NRL betatron.

2. EFFECT OF SPREAD IN CIRCULATION FREQUENCIES

One proposal to reduce or eliminate the negative-mass instability involves a spread in particle circulation frequencies [7]. Some spread in circulation frequencies is always present due to finite beam radius, but since the beam rotates poloidally [8], the frequency spread is only of order $(r_b/R)^2$, where r_b is the beam radius. For a given beam radius, one obtains maximum frequency spread when the beam particles do not oscillate transversely, as discussed in Ref. 1. One can achieve this by introducing an energy spread on the beam, or by making the poloidal rotation frequency small enough. The latter occurs naturally near the so-called diamagnetic-paramagnetic transition energy, where the poloidal rotation changes direction [8].

For the low-current conventional betatron, it is possible to derive analytically the effect of a spread in circulation frequencies. For the case of a beam with a uniform current density profile, one finds [see Appendix C, Eqs. (34)-(38)] that the growth rate goes to zero for a beam radius such that

$$\frac{\ell r_b}{R^2} c > \Gamma_0 \quad (2)$$

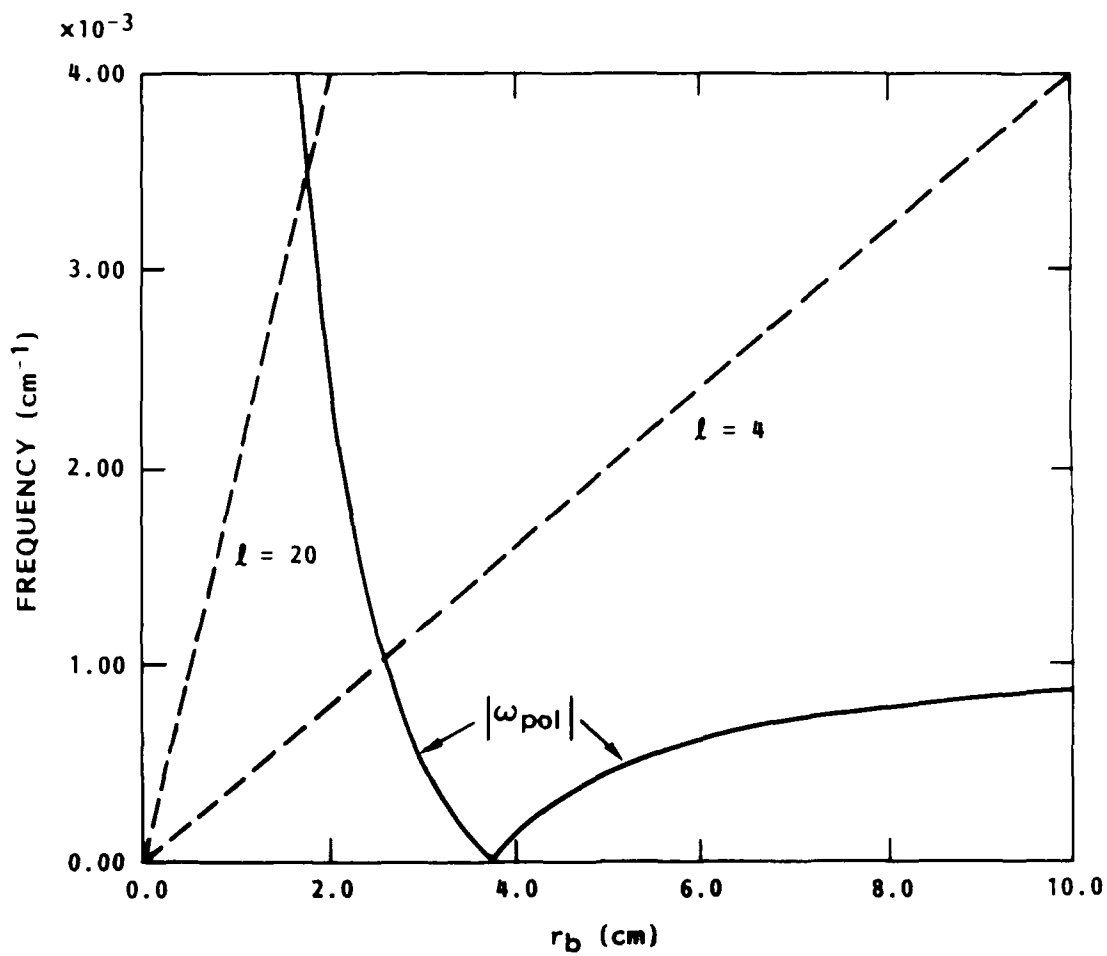
where Γ_0 is the growth rate for a cold beam and ℓ is the toroidal mode number. If the beam has a finite poloidal rotation frequency ω_{pol} , then one can argue heuristically that Eq. (2) is still the condition for stability provided, that, in addition

$$\frac{\ell r_b}{R^2} c > |\omega_{pol}| \quad (3)$$

This extra condition ensures that a disk of particles initially at one toroidal location will become smeared out over several wavelengths during one poloidal rotation period.

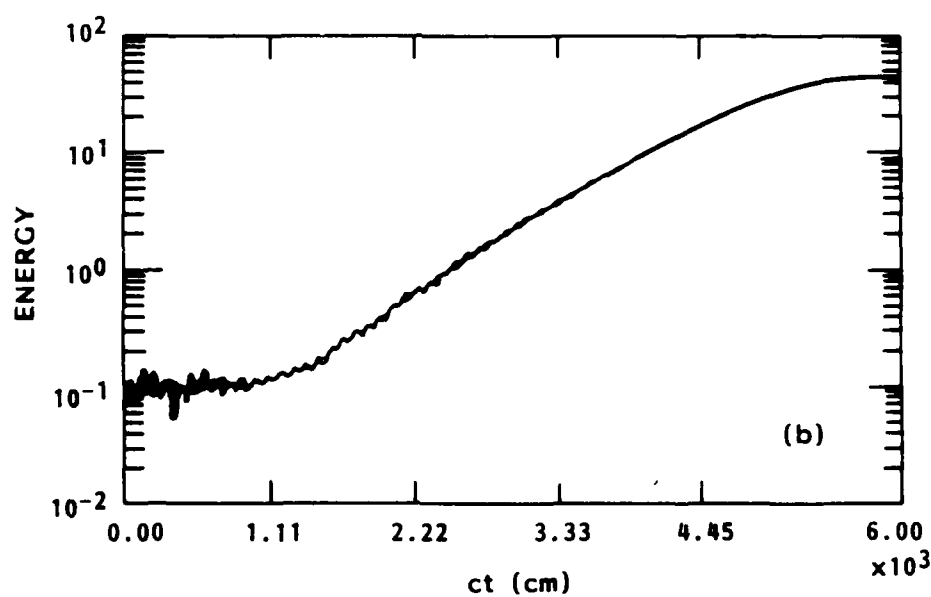
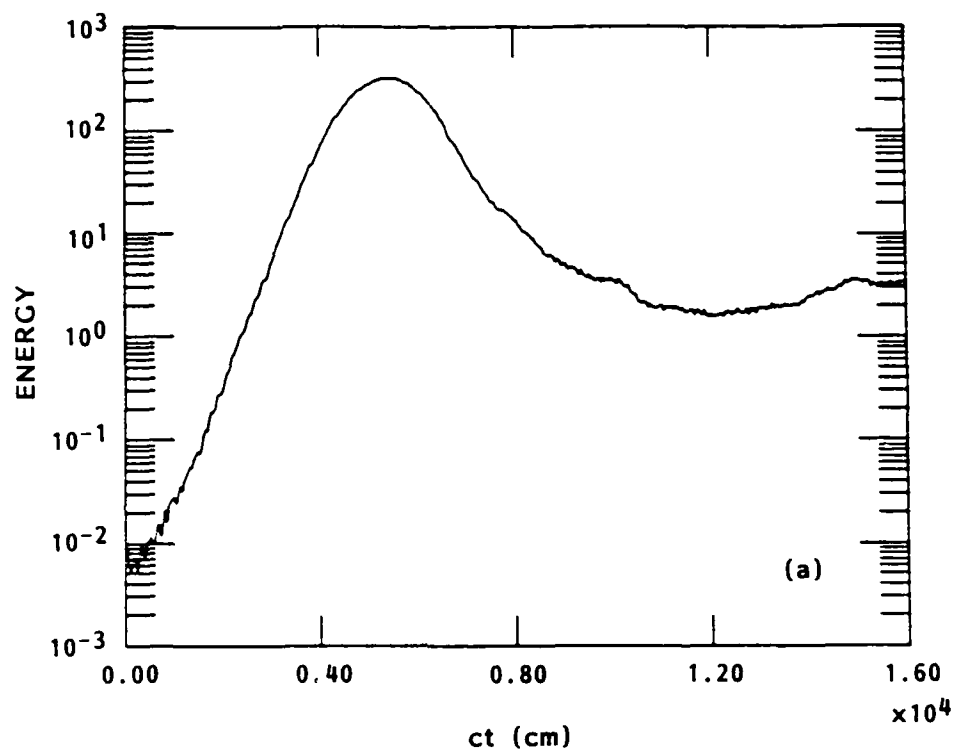
We have performed numerical simulations to test the applicability of Eqs. (2) and (3) to the modified betatron, for which we have not attempted a rigorous derivation of these criteria. We looked at cases in which the beam current and energy are kept fixed, but where the poloidal rotation frequency of the beam is varied. This is accomplished by changing the beam radius. The two sides of Eq. (3) are plotted versus beam radius in Fig. 2 for a 10 kA, $\gamma = 12$ beam. For a beam radius of 2 cm, Eq. (3) is strongly violated for low ℓ modes (we have chosen $\ell = 4$ for this example). Thermal effects are therefore expected to be negligible. This is indeed what we find in the simulation. As shown in Fig. 3a, the instability grows at the predicted cold growth rate. A particle plot made near the end of the linear growth is shown in Fig. 4a. Nine disks of particles are used to resolve one wavelength of the instability. Initially, these disks have zero thickness, but a spread in circulation frequencies causes them to smear out toroidally. Consistent with the observed cold beam growth rate, the disks in Fig. 4a show little spreading. Soon after the stage in Fig. 4a, about 3/4 of the current is lost to the walls. Parenthetically, we remark that this simulation illustrates that the toroidal magnetic field is a mixed blessing for beam stability. While it cuts the growth rate of the instability significantly from what one would obtain without it, it also inhibits the radial motion which tends to saturate the instability by producing a spread in circulation frequencies. Note that the distortion of the beam in Fig. 4a is primarily in the z direction, and so does not contribute to stability.

In contrast to the case just discussed, Eq. (3) is well satisfied when the beam radius is increased to 3.5 cm, so that the poloidal rotation may be effectively ignored (see Fig. 2). Substituting the cold beam growth rate into Eq. (2), we find that marginal stability is predicted. In a simulation for this beam radius, however, we see a finite growth rate of about half the cold growth rate, as shown in Fig. 3b. Thus, Eq. (2) somewhat underestimates the beam radius required for stability in the modified betatron. The instability causes the beam to distort in a manner similar to the small-radius case, as shown in Fig. 4b. However, the instability



R-922

Figure 2. Plot of the two sides of Eq. (3) for a 10 kA, $\gamma = 12$ beam.



R-922

Figure 3. Energy histories of the $\lambda = 4$ negative-mass instability on a 10 kA, $\gamma = 12$ beam with initial radius $r_b = 2$ cm in (a) and $r_b = 3.5$ cm in (b).

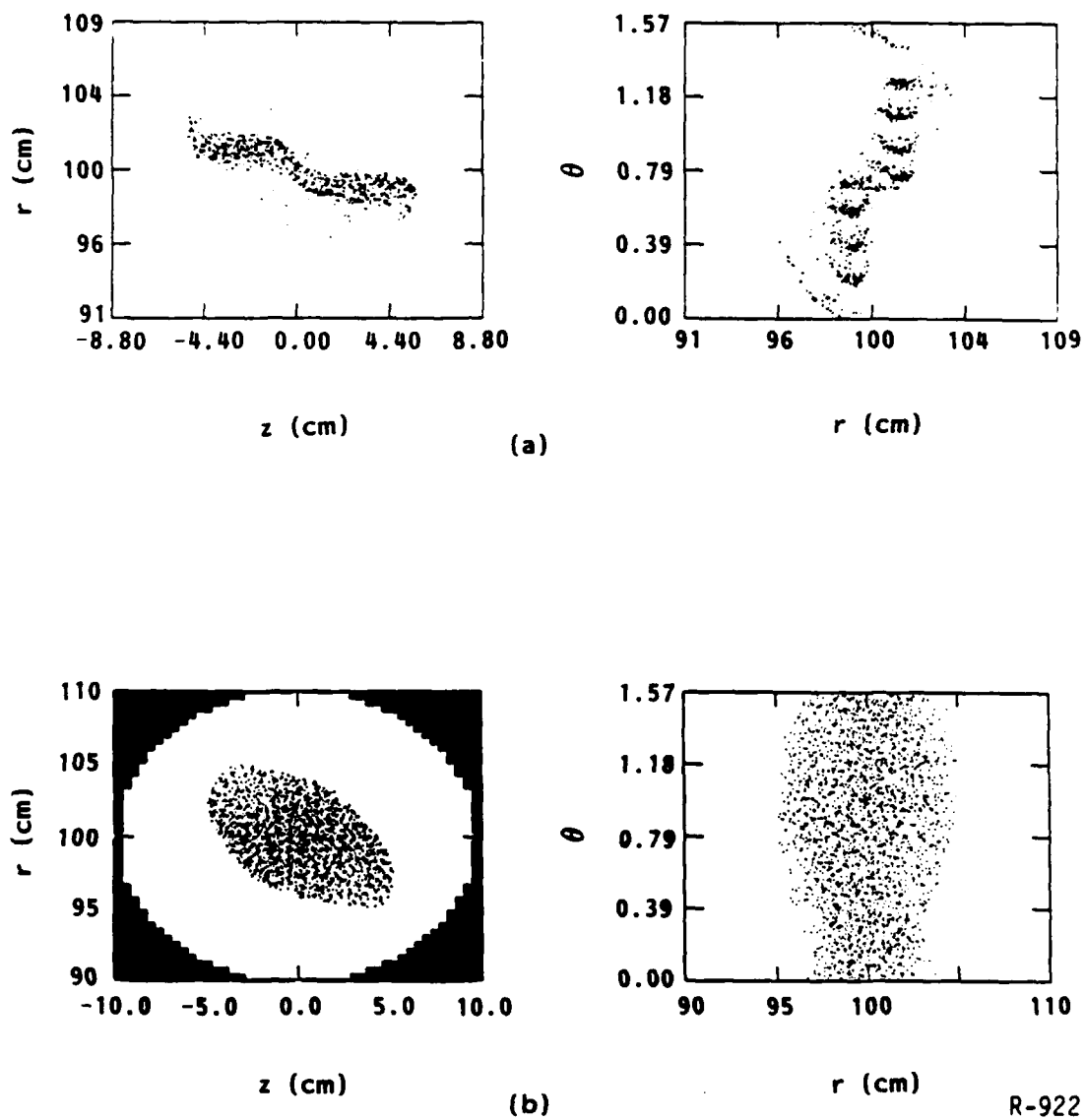


Figure 4. Particle plots taken during the nonlinear stages of the simulations shown in Fig. 3. For (a), the initial beam radius is $r_b = 2$ cm and in (b), the initial beam radius is $r_b = 3.5$ cm.

saturates at a much lower level for the larger beam radius. This leads us to believe that the beam is close to marginal stability initially, and that the small energy spread created by the instability is sufficient to stabilize it without loss of current.

We have run a similar series of cases for the $\ell = 20$ mode. These runs illustrate again the importance of satisfying Eq. (3) in order to get the full benefit of finite beam radius stabilization. For a 1.7 cm beam radius, we see from Fig. 2 that Eq. (3) is not satisfied for the $\ell = 20$ mode. A particle simulation shown in Fig. 5a confirms that the instability grows at the cold beam growth rate, $\Gamma_0 = 2.9 \times 10^{-3} \text{ cm}^{-1}$. Increasing the beam radius to 2.0 cm puts us in a regime where Eq. (3) is only weakly satisfied. We observe growth of the instability at roughly half of the cold value, as shown in Fig. 5b. The wavy energy curve seems to be characteristic of cases where Eq. (3) is weakly satisfied. Note that Eq. (2) predicts stability for the 2 cm beam ($\ell r_b/R^2 = 4 \times 10^{-3} \text{ cm}^{-1}$). The non-linear development is very similar to that of the 1.7 cm beam.

Increasing the beam radius further to 3 cm results in Eq. (3) being well satisfied, and Eq. (2) becomes satisfied by a factor of two ($\Gamma_0 c = 2.9 \times 10^{-3} \text{ cm}^{-1}$, $\ell r_b/R^2 = 6 \times 10^{-3} \text{ cm}^{-1}$). In a simulation for this radius, some erratic growth is seen (Fig. 5b), but not enough to measure a reliable growth rate. The peak perturbed field energy in Fig. 5b is only 0.2% of the equilibrium field energy. The beam radius increases slightly, but no current loss is observed.

Finally, we present some results for parameters closer to the NRL experiment than the above cases. We performed a simulation of the $\ell = 20$ mode near the peak of the growth curve in Fig. 1 for a 3 kA, $\gamma = 7$ beam. The two sides of Eq. (3) are plotted in Fig. 6a. We choose a radius of 2 cm, which is on the order of the experimentally measured value. For this radius, Eq. (3) is marginally satisfied, and Eq. (2) is satisfied by about a factor of three ($\Gamma_0 c = 1.3 \times 10^{-3} \text{ cm}^{-1}$, $\ell r_b/R^2 = 4.0 \times 10^{-3} \text{ cm}^{-1}$). The growth rate observed in the simulation is erratic, and on the order of

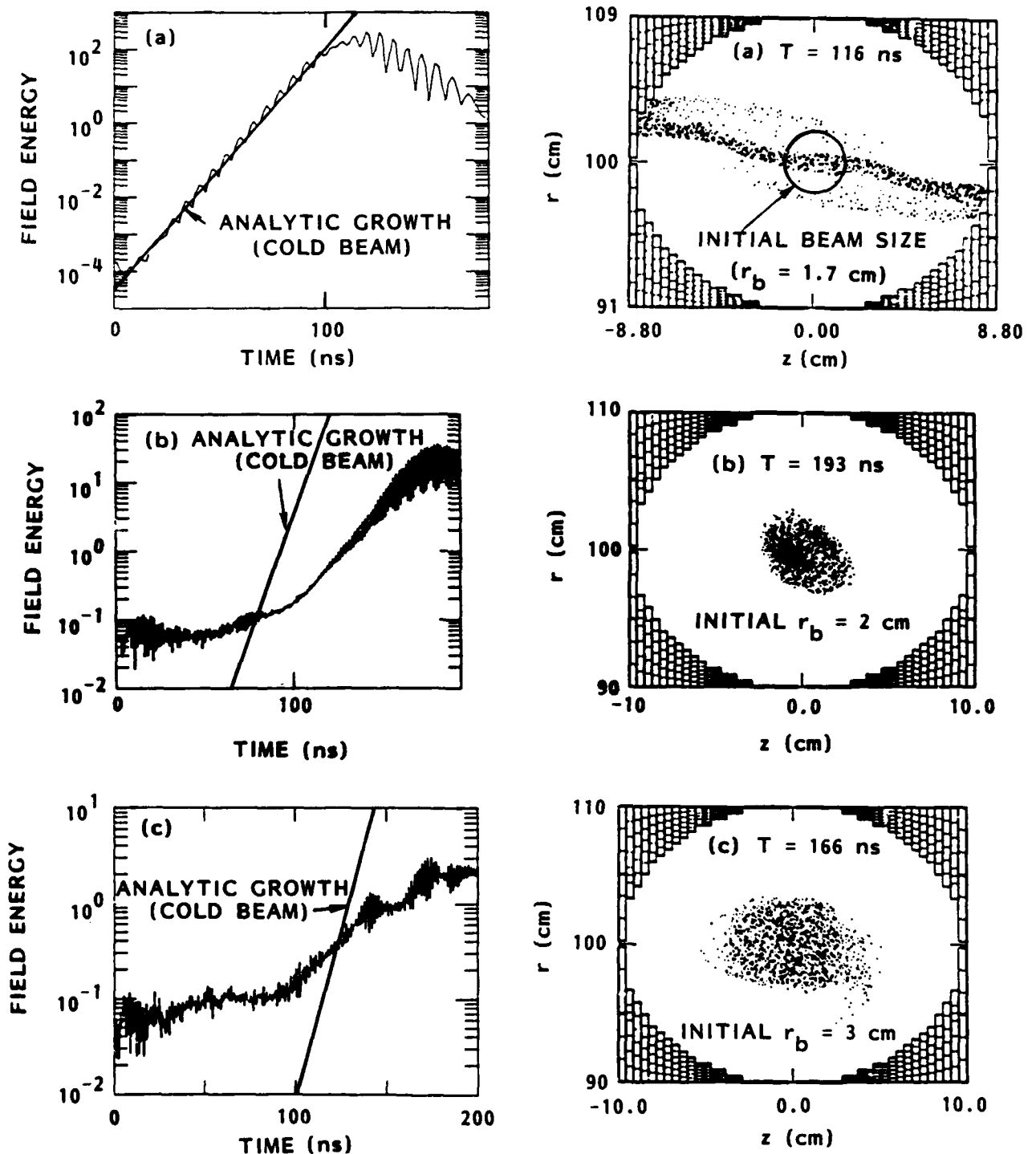
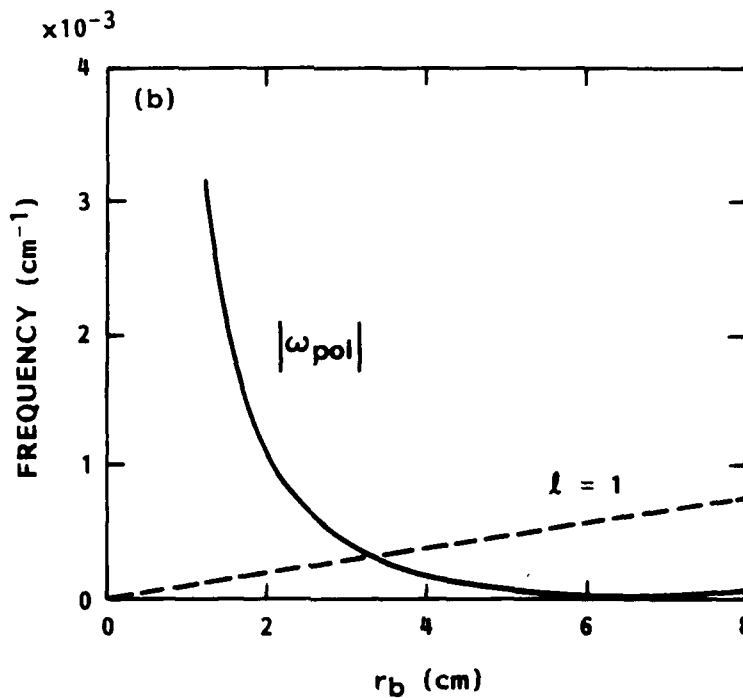
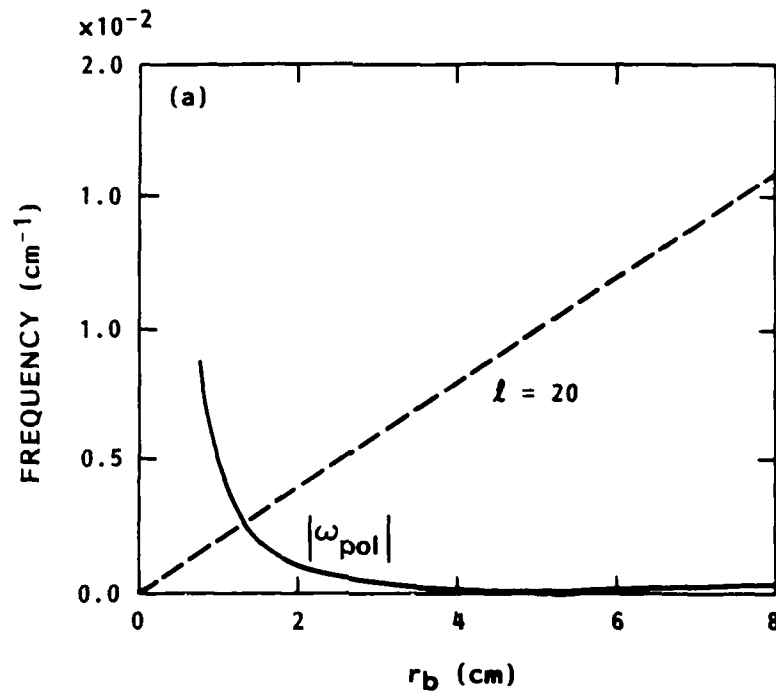


Figure 5. Energy histories and particle plots for simulations of the $l = 20$ negative mass instability on a 10 kA, $\gamma = 12$ beam. The initial beam radius is 1.7 cm in (a), 2 cm in (b) and 3 cm in (c).



R-922

Figure 6. Plot of the two sides of Eq. (3) for parameters typical of the NRL betatron. In (a) the beam parameters are 3 kA, $\gamma = 7$, and in (b) the parameters are 1 kA and $\gamma = 4$. In each case, a 2.5 kG toroidal field is assumed.

$3.6 \times 10^{-4} \text{ cm}^{-1}$, much less than the cold growth rate. If Eq. (3) were better satisfied, e.g., $r_b \geq 3 \text{ cm}$, the $\ell = 20$ mode would likely be completely stable.

In Fig. 6b, we show the two sides of Eq. (3) for a 1 kA beam in a 2.5 kG toroidal field at an energy of $\gamma = 4$, which corresponds roughly to the peak of the 1 kA growth rate curve in Fig. 1. We see that for low ℓ -numbers, Eq. (3) is not satisfied for $r_b \leq 2 \text{ cm}$. We therefore would expect to see some growth of the negative-mass instability at these mode-numbers in the NRL experiment. The nonlinear development of the instability is not known for a 1 kA beam current. Given the large minor radius of the drift-tube (15 cm), it is possible that the instability may saturate without loss of current.

3. BEAM STABILITY AT HIGH ENERGIES

A novel prediction of the analytic dispersion relation derived in Ref. 1 is that the character of the negative mass instability for high ℓ numbers changes above a certain energy. "High ℓ " in this context typically means $\ell > 12$ [1]. A representative growth curve is shown in Fig. 7 ($\ell = 20$, $I = 10 \text{ kA}$, $B_0 = 1 \text{ kG}$). Above $\gamma = 20$, the usual nonresonant negative mass instability gives way to a resonant interaction between the longitudinal and transverse modes of the beam. We performed a number of simulations in this regime to test the analytic predictions. The results, shown in Fig. 7, are in reasonably good agreement with theory. A common feature of the simulations for $\gamma > 20$ is that the beam radius increases in the nonlinear state, but no current loss occurs. The nonlinear state of the beam in the $\gamma = 50$ simulation is shown in Fig. 8. A steady state transverse profile is not reached in the time of the simulation. However, the energy in the perturbed fields decreases by about a factor of 30 from its peak value during the nonlinear saturation, as the bunches of charge become smeared out. The relative ease with which the modes stabilize nonlinearly can be attributed in part to their relatively low growth rates, and to the fact that little transverse kinking of the beam is produced by the

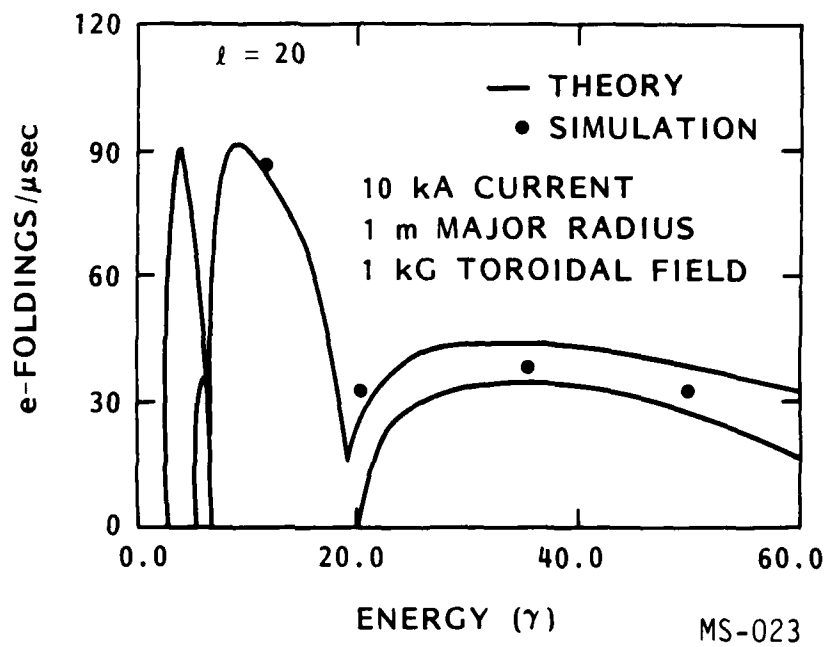
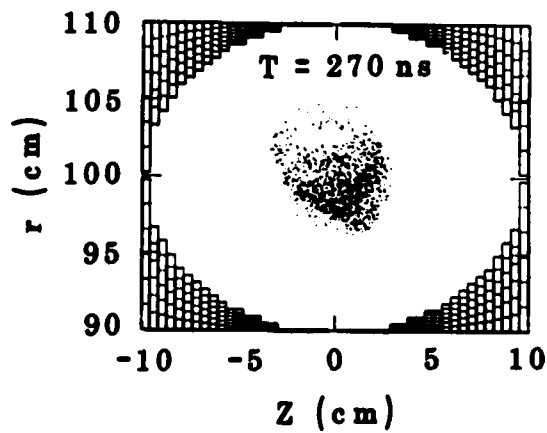
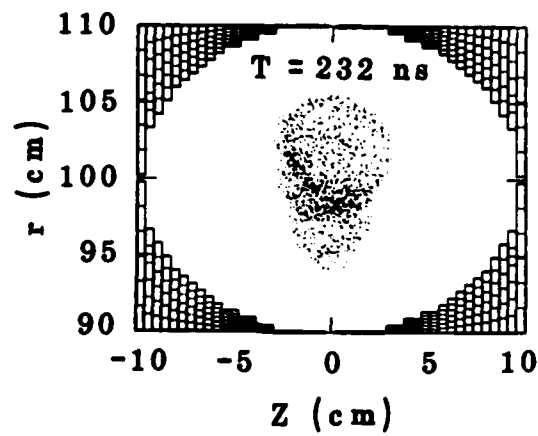
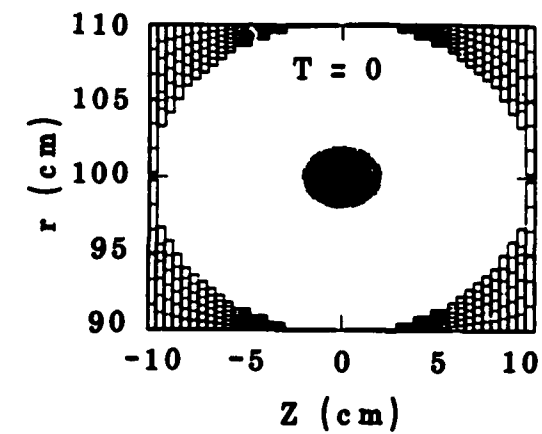


Figure 7. Instability growth rates of the $l = 20$ mode for a 10 kA beam in a 1 kG toroidal field.



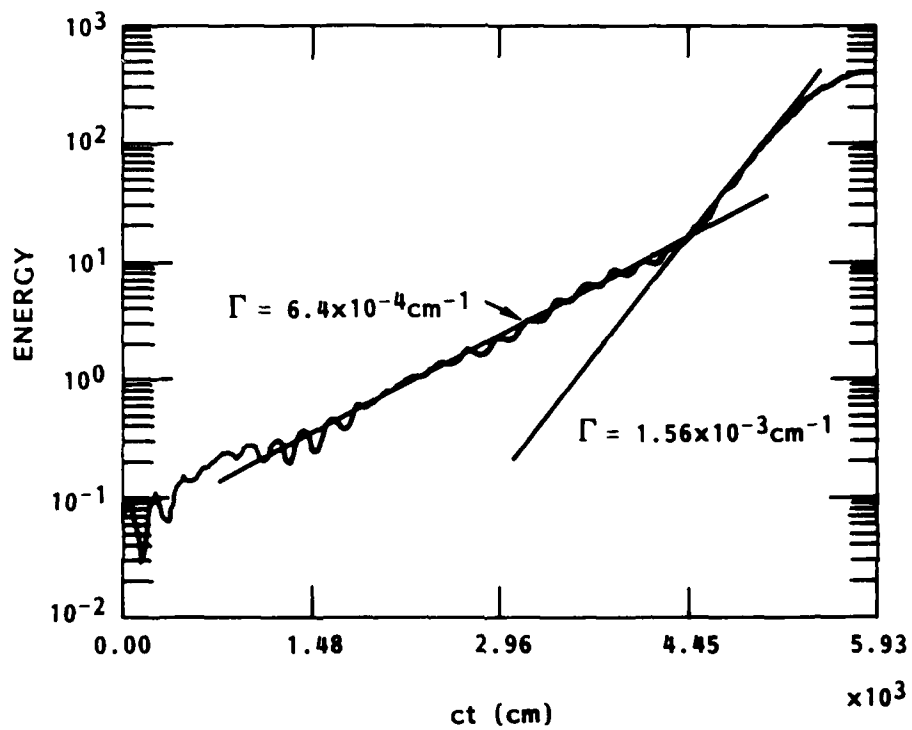
VG-696

Figure 8. Particle plots illustrating the nonlinear saturation of the $k = 20$ instability on a $\gamma = 50$ beam.

instability, unlike the negative-mass instability. This is discussed further below.

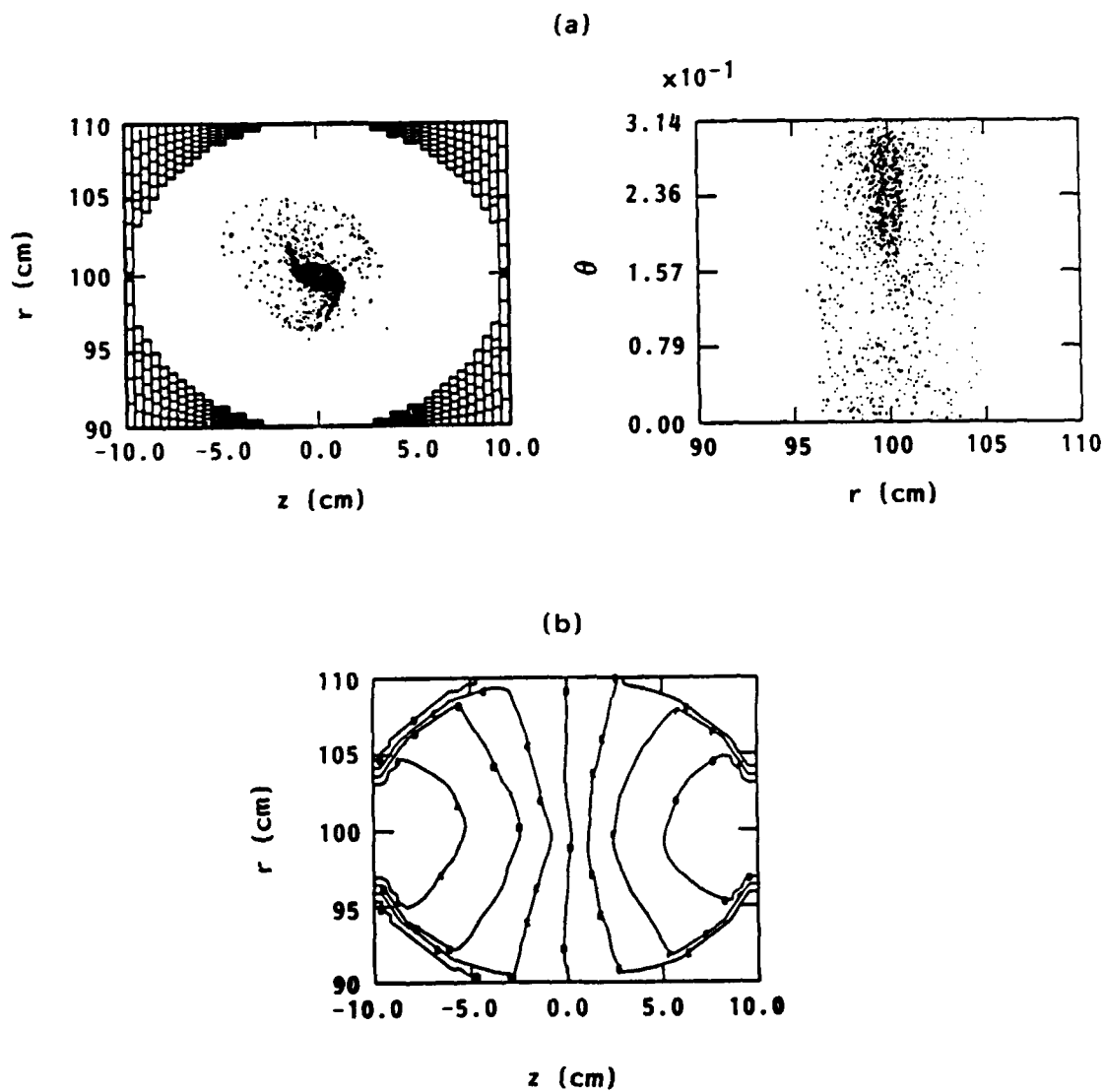
For the simulations at $\gamma = 35$ and 50 , the two sides of Eq. (3) are comparable in magnitude, so that it is difficult to predict how much damping from circulation frequency spread is present in the simulations. If Eq. (3) were well satisfied, then Eq. (2) would predict stability for each of the simulations for $\gamma > 20$. Based on the results in Figs. 4b and 5b, it is perhaps surprising that there is not a larger discrepancy between the cold beam growth rates and the simulation results.

For the simulation at $\gamma = 20$, Eq. (3) is reasonably well satisfied, so that we would certainly have expected the thermal effects to have a more significant effect than is evident from Fig. 7. Since the shape of the analytic curve in this region is sensitive to small changes in the beam energy, we also performed simulations at $\gamma = 19.7$, and $\gamma = 20.5$, but obtained the same growth rate as for $\gamma = 20$, namely, $r_0 = 1.1 \times 10^{-3} \text{ cm}^{-1}$. Next, we sought to decrease whatever thermal effects might be present by reducing the beam radius from 2 cm to 1 cm. This made the beam rotate faster in the poloidal direction. The growth curve for this beam at $\gamma = 20$ is shown in Fig. 9. Note that there are two distinct slopes, giving growth rates of $6.3 \times 10^{-4} \text{ cm}^{-1}$ and $1.56 \times 10^{-3} \text{ cm}^{-1}$. It is tempting to identify the lower growth rate with the dip in growth rate at $\gamma = 20$ in Fig. 7. It may be that the instability grows at the analytically predicted rate at low amplitudes, and that a type of mode-locking takes over as the amplitude gets large. In this light, it may be significant that in each of the 2 cm beam runs around $\gamma = 20$ there is a relatively long period ($\sim 100 \text{ ns}$) at the start of the simulations where very little growth is seen. At $\ell = 20$, the resonant denominator in the dispersion relation due to the TE_{11} mode is starting to have a noticeable effect on the beam behavior, even though we are not at exact resonance. This is evident from the TE_{11} -like structure of the contour plot of the perturbed magnetic field B_θ shown in Fig. 10b, which is taken from the nonlinear stage of the $\gamma = 20$, $r_b = 1 \text{ cm}$ simulation. It is indeed the proximity of the TE_{11} mode resonance which is



R-922

Figure 9. Energy history of the $\ell = 20$ instability on a $\gamma = 20$ beam with an initial radius of 1 cm, showing two distinct slopes.



R-922

Figure 10. Nonlinear state of the $\ell = 20$ instability on a $\gamma = 20$ beam with an initial radius of 1 cm.

responsible for the change in the character of the negative-mass instability referred to above.

For the 1 cm beam case, there is strong longitudinal bunching of the beam in the nonlinear state, as shown in Fig. 10a. This contrasts with the 2 cm beam runs, where the perturbations saturate at a much lower level. It also contrasts with the nonlinear development at $\gamma = 12$, shown in Fig. 4a, where there is considerable transverse kinking of the beam. Such pronounced transverse kinking is characteristic of the negative-mass instability. The different nonlinear behavior is evidence that the instability for $\gamma > 20$ is not a negative-mass instability. It is possible to have longitudinal bunching without much transverse kinking since the equilibrium position of the beam depends on $\gamma + \phi$, where ϕ is the electrostatic potential of the beam; $\gamma + \phi$ can remain fixed as the beam bunches.

We also ran a 3 cm radius beam at $\gamma = 20$. Equations (2) and (3) predict stability, but we observe a growth rate of $8.2 \times 10^{-4} \text{ cm}^{-1}$, only slightly smaller than the 2 cm rate. The mode saturates at approximately the same level as the 2 cm runs. Finally, we ran a 2 cm beam case where, instead of a slow $E \times B$ mode equilibrium, we ran the beam in the Brillouin limit. In this limit, the beam is rotating at the Larmor frequency, $\Omega_0/2\gamma$, and the particles are given whatever temperature is required to give force balance. This results in a beam with little spread in particle frequencies. We observe a low initial growth rate of $4.2 \times 10^{-4} \text{ cm}^{-1}$, (cf. the 1 cm radius case described above) and the perturbations saturate at an energy level about an order of magnitude lower than for the slow $E \times B$ equilibrium. A comparable increase in beam radius is observed, however, whether due to the instability, or to slow (perhaps numerical due to the fast rotation) changes in the beam equilibrium.

4. RESONANCES IN THE MODIFIED BETATRON AT LOW ENERGIES

In addition to the collective instabilities discussed above, the modified betatron is prone to single-particle resonances. These occur when

one of the transverse oscillation frequencies is an integer multiple of the circulation frequency, ω_0 :

$$\Omega_{\pm} = l\omega_0 \quad (4)$$

Errors in the applied magnetic fields then result in transfer of energy from the longitudinal direction to the transverse direction. The transverse frequencies are given by the expressions

$$\begin{aligned} \Omega_+ &= \left(\omega_r^2 + \Omega_\theta^2/4\gamma^2 \right)^{1/2} + \frac{\Omega_\theta}{2\gamma} \approx \frac{\Omega_\theta}{\gamma} \\ \Omega_- &= \left(\omega_r^2 + \Omega_\theta^2/4\gamma^2 \right)^{1/2} - \frac{\Omega_\theta}{2\gamma} \approx \frac{\omega_r^2}{\Omega_\theta/\gamma} \end{aligned} \quad (5)$$

where ω_r^2 is the focusing force due to betatron focusing and self-fields. For the beam centroid motion, ω_r^2 is given by $(1/2 - n_s r_b^2/a^2)\omega_0^2$, where n_s is the self-field index ($\approx 2\gamma R^2/\gamma^3 r_b^2$). At low energies, the low frequency Ω_- is less than ω_0 , so that resonance is impossible, while the fast frequency Ω_+ is much greater than ω_0 , giving a weak, high order resonance. For the motion of particles within the beam, on the other hand, $\omega_r^2 = (1/2 - n_s)\omega_0^2$, and the slow frequency can be a few times larger than ω_0 , giving rise to a low order resonance. (The fast frequency is still much larger than ω_0 .) The ratio $|\Omega_-|/\omega_0$ is plotted as a function of energy in Fig. 11 for parameters relevant to the NRL betatron (1-3 kA, $B_0 = 2.5$ kG, $r_b = 1$ cm). Near the present injection parameters, which yield a 1 kA ring with $\gamma = 1.5$ -2.0, there are a number of low order resonances. Their effect on the beam seems to be rather weak, however. We show in Fig. 12 the effect of errors of 1% and 4% in the vertical field on a particle near the $l = 2$ resonance in a 2 kA beam. The particle is started near the origin, and its betatron motion is amplified to just 0.5 cm for the 4% error. It is not possible for the motion reach an amplitude much larger than the beam radius since the potential well due to the self-fields outside the beam is strongly anharmonic. Also, the cases shown in Fig. 12 are not self-consistent in

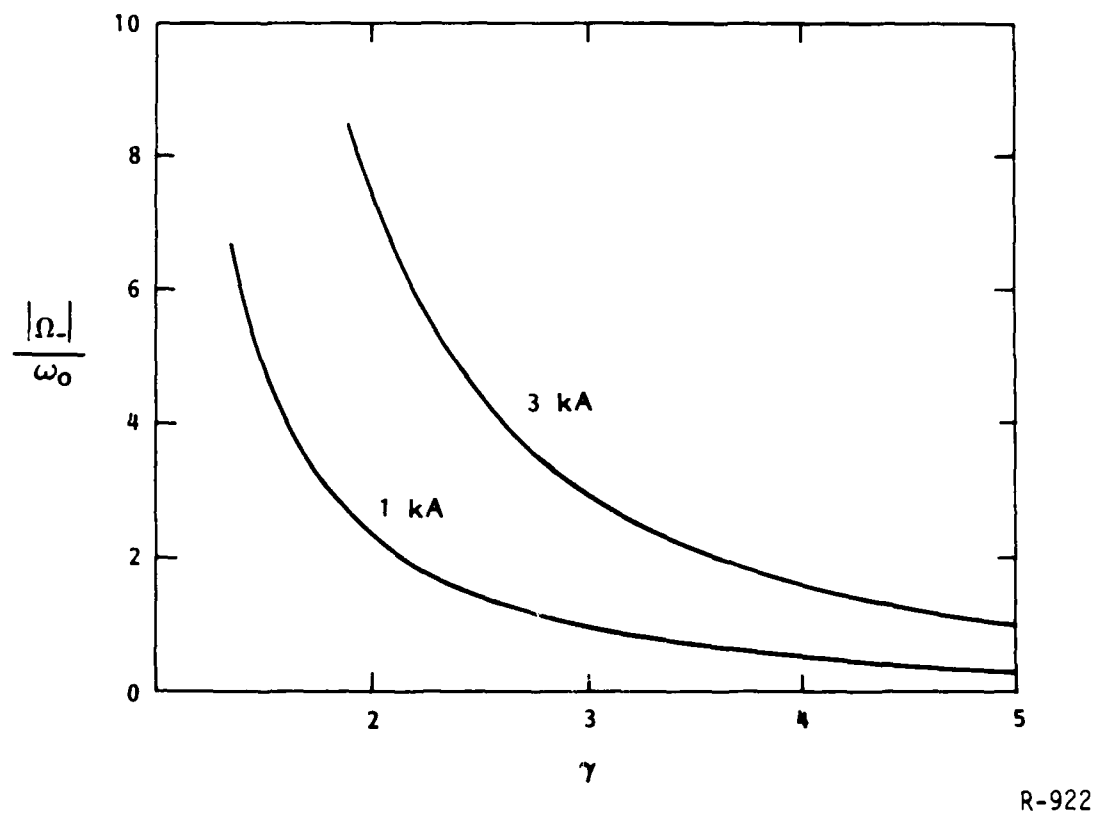
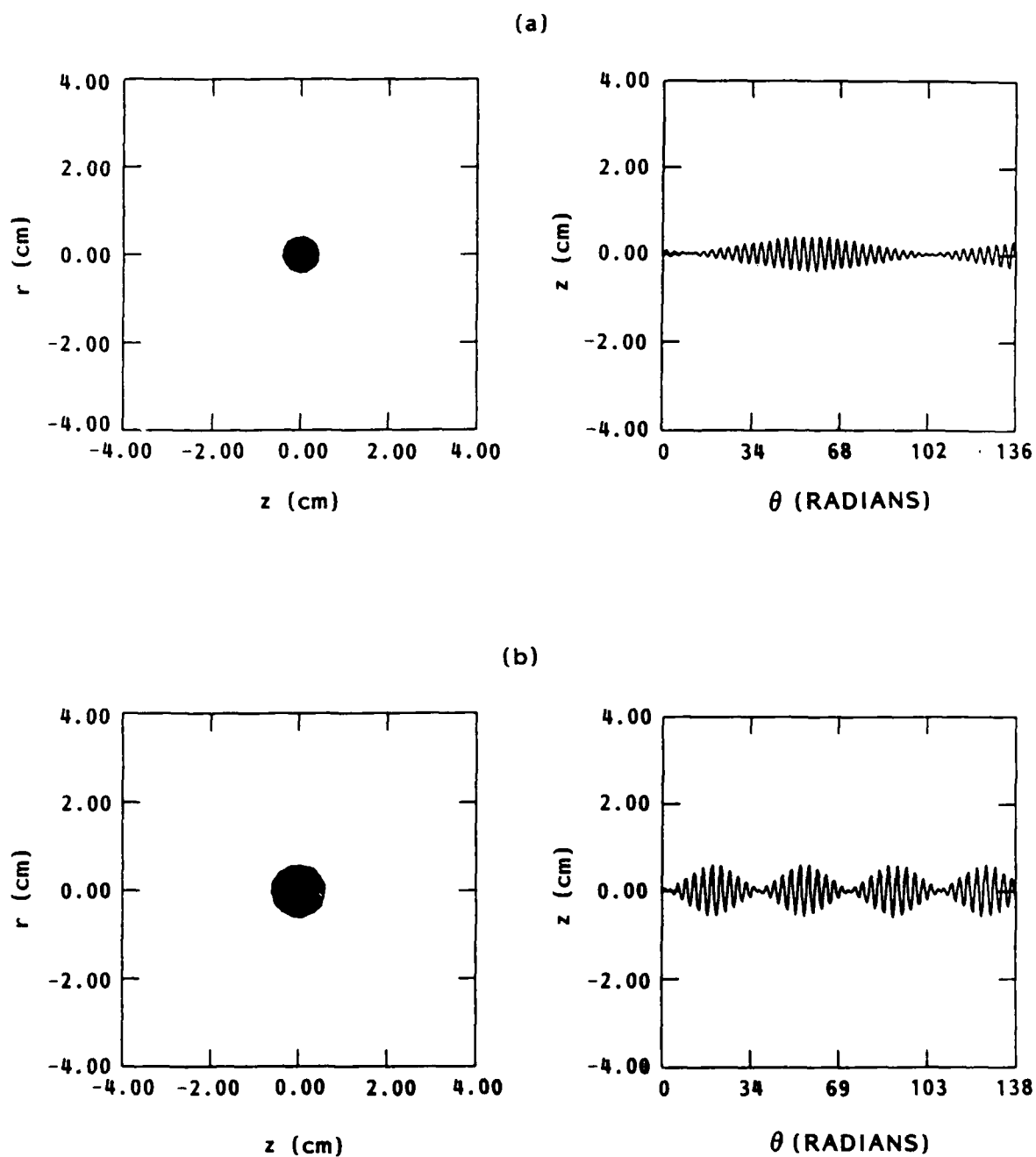


Figure 11. Plot of betatron tunes versus energy for typical NRL betatron parameters, showing low integer resonances.



R-922

Figure 12. Amplification of betatron oscillations due to an $\ell = 2$ resonance in a 2 kA, $\gamma = 3$ beam. In (a), the error in the vertical field is 1%, and in (b) the error is 4%.

that the space-charge of the beam is held fixed while the test particle is being advanced. In a self-consistent case, the whole beam would expand, thereby changing ω_r^2 and detuning the resonance. We therefore believe that these resonances may contribute to some heating of the beam, but are unlikely to be responsible for the gradual current loss observed in the experiment [2].

III. STELLATRON ACCELERATOR

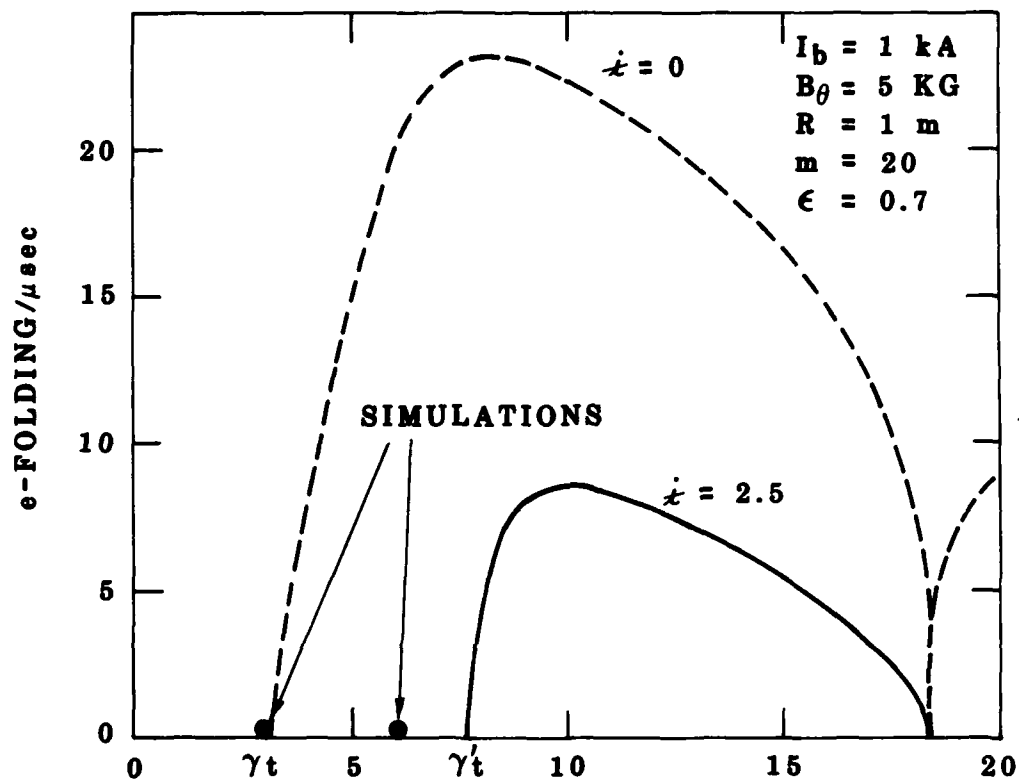
1. RESULTS RELATED TO THE UCI STELLATRON

The stellatron accelerator adds a helical quadrupole to the modified betatron design. The main effect of this is to increase the energy acceptance of the device. This helps to suppress the negative-mass instability by inhibiting transverse motion of the beam. It also pushes up the transition energy at which the effective mass of the particles becomes negative [9]. As reported in Ref. 1, our simulation results support these conclusions. In Fig. 13, we show results of two simulations confirming the increase in the transition energy relative to the modified betatron. The stellatron growth rates in this figure were obtained by putting the smoothed approximation for the quadrupole focusing obtained by Chernin [9] into the modified betatron dispersion relation obtained in Ref. 1.

The UC Irvine stellatron has succeeded in accelerating significant amounts of charge from rest up to 10 MeV [10]. The peak current is over 1 kA up to about 4 MeV and gradually drops off, leaving a few hundred amperes at 10 MeV.

We have applied the dispersion relation derived in Ref. 1, modified as discussed above, to the parameters of this experiment. In addition to the quadrupole focusing, however, we need to take account of the fact that the UCI beam is charge-neutral. This is because it is created by runaway acceleration from an initially stationary plasma. The runaway fraction is thought to be on the order of 100% [10]. Thus the ions, in addition to providing space-charge neutralization, also provide transverse focusing of the electron beam, in the manner of IFT (ion-focused transport). The transverse focusing frequency becomes

$$\omega_r^2 \rightarrow \omega_r^2 + \gamma^2 n_s \omega_0^2 \quad (6)$$



VG-740

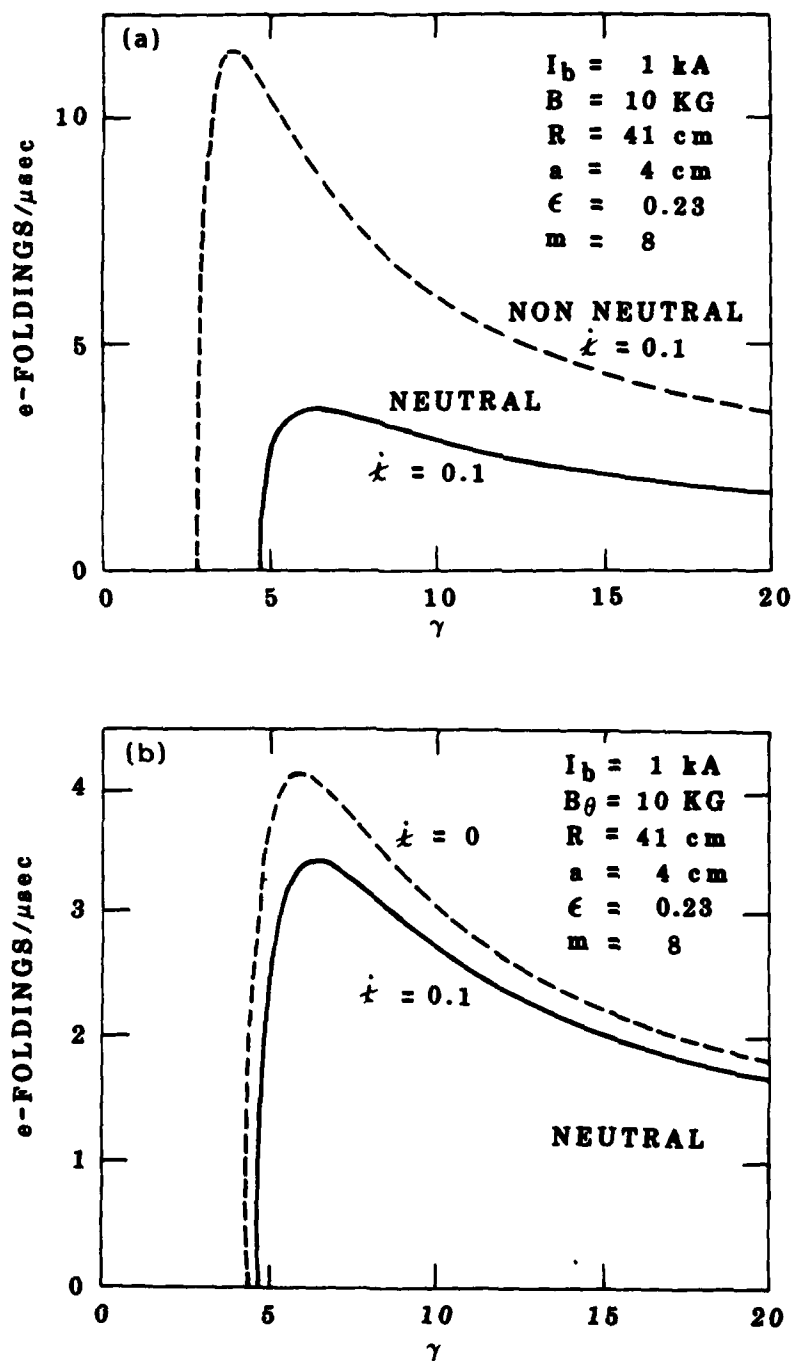
Figure 13. Growth rates of the $\ell = 20$ negative-mass instability for typical stellatron parameters. The solid line is for a stellatron field such that the helical field parameter $\epsilon = 0.7$, while the dashed line is for $\epsilon = 0$.

When we include the additional focusing term in the dispersion relation, we find that its effect on the beam stability is greater than the effect of the helical quadrupole, as shown in Fig. 14. In Fig. 14a, we see that introducing the ions makes a significant difference in the peak growth rate, and in the transition energy. In Fig. 14b, on the other hand, we see that applying the helical quadrupole has little effect. (The helical field is essential to generate the beam initially, however.) This result was suggested by Ishizuka [10], and is in agreement with the experimental findings. Disruption of the beam accompanied by strong rf oscillations at harmonics of the circulation frequency is seen early in the acceleration cycle. This is thought to be due to the onset of the negative mass instability as the beam goes through the transition energy. The transition energy is observed to increase with the beam current, which is consistent with the ion-focusing picture. For a 1 kA beam, the onset of instability is observed at around 2 MeV, in agreement with the prediction from Fig. 14.

2. ELECTROMAGNETIC INSTABILITY DUE TO THE HELICAL FIELD

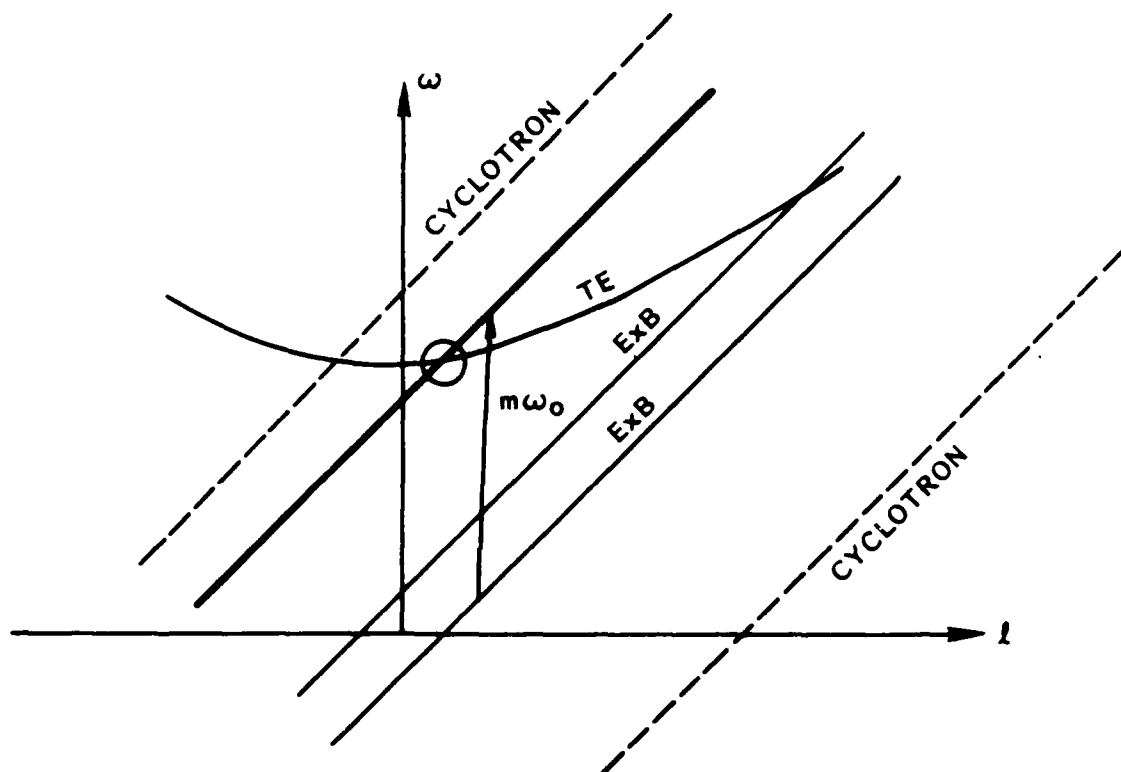
A virulent electromagnetic instability observed in simulations of the stellatron was reported in Ref. 1. We subsequently derived an analytic model of this interaction which is reproduced in Appendix A. The mode is a three-wave coupling resembling the free-electron laser interaction, except that the beam mode involved is transverse rather than longitudinal. Using FEL terminology, the quadrupole field acts as a wiggler and upshifts the slow transverse mode on the beam so that it can intersect the lowest electromagnetic mode, the TE_{11} mode. This is illustrated qualitatively in Fig. 15.

The analytic model given in Appendix A gives reasonably good agreement with the simulation results. For high currents and strong focusing, the growth rates can be very large. A simulation of a 10 kA, 3.3 MeV beam showed disruption of the beam in just one turn around the 1 m radius device. We have seen linear growth of the instability in simulations with currents as low as 300 A.



VG-740

Figure 14. Growth rates of the $l = 1$ negative-mass instability for parameters typical of the UCI stellatron, illustrating the large effect of ion focusing on the growth rate and transition energy.



R-922

Figure 15. Qualitative picture of the modes which interact to produce the 3-wave electromagnetic instability in a stellatron.

We have looked at the 3-wave instability for the parameters of the UCI stellatron (see Fig. 14), and find that growth is predicted in the energy range 2.5-3.5 MeV, with the intersection in Fig. 15 occurring at about $\ell = 18$. The predicted growth rate is quite large, about 30 e-foldings/ μ sec. At this point we do not know whether any of the current loss in the experiment can be attributed to this instability. Thermal effects have not been included in the theory, and at high ℓ -numbers may stabilize the mode. A quadrupole focusing experiment being mounted at PSI has been deliberately designed to push the intersection in Fig. 15 out to high ℓ -numbers [11].

IV. SOLENOIDAL LENS BETATRON

1. BEAM TRANSPORT

The solenoidal lens betatron is a strong-focusing device with solenoids of alternating polarity placed around a torus [4]. As the beam travels around, it rotates poloidally at the Larmor frequency, changing its direction of rotation from one solenoid to the next. A device of this type has been constructed at the Institute for Accelerator and Plasma Beam Technology (IAPBT) at the University of New Mexico.

We have simulated beam transport in a solenoidal lens betatron using both the exact fields for finite-length solenoids, and a sinusoidal approximation to the fields, with similar results. The simulations, described in Appendix B, demonstrate the higher mismatch tolerance of the device relative to the modified betatron. Recent experiments on the machine have convincingly shown this property by being able to transport current around 180 degrees without any vertical field [4]. This tolerance is considerably larger than that seen in the simulations in Appendix B because the experimental injection energy is just 300 kV instead of 1 MeV, so that the centrifugal force on the beam is substantially smaller. If this large energy acceptance is to be maintained as the beam is accelerated, then the solenoidal fields must be ramped in synchronism with the beam energy. This can be seen from the expression for the momentum compaction factor

$$\alpha = \left(\frac{1}{2} - n_s r_b^2 / a^2 + \frac{1}{8} \frac{B_0^2}{B_z^2} \right)^{-1} \quad (7)$$

where B_0 is the amplitude of the solenoidal field and B_z is the vertical field. This equation can be simplified if we assume that the beam radius is matched to the solenoidal field, and that the beam is space-charge dominated, i.e., the emittance is negligible in the force balance equation.

Since the beam is injected from a cathode shielded from magnetic fields, then it is always in the Brillouin limit (assuming it is matched), so that the force-balance equation is

$$\frac{1}{2} - n_s + \frac{1}{8} \frac{B_0^2}{B_z^2} = 0 \quad (8)$$

Substituting this into Eq. (7) we obtain

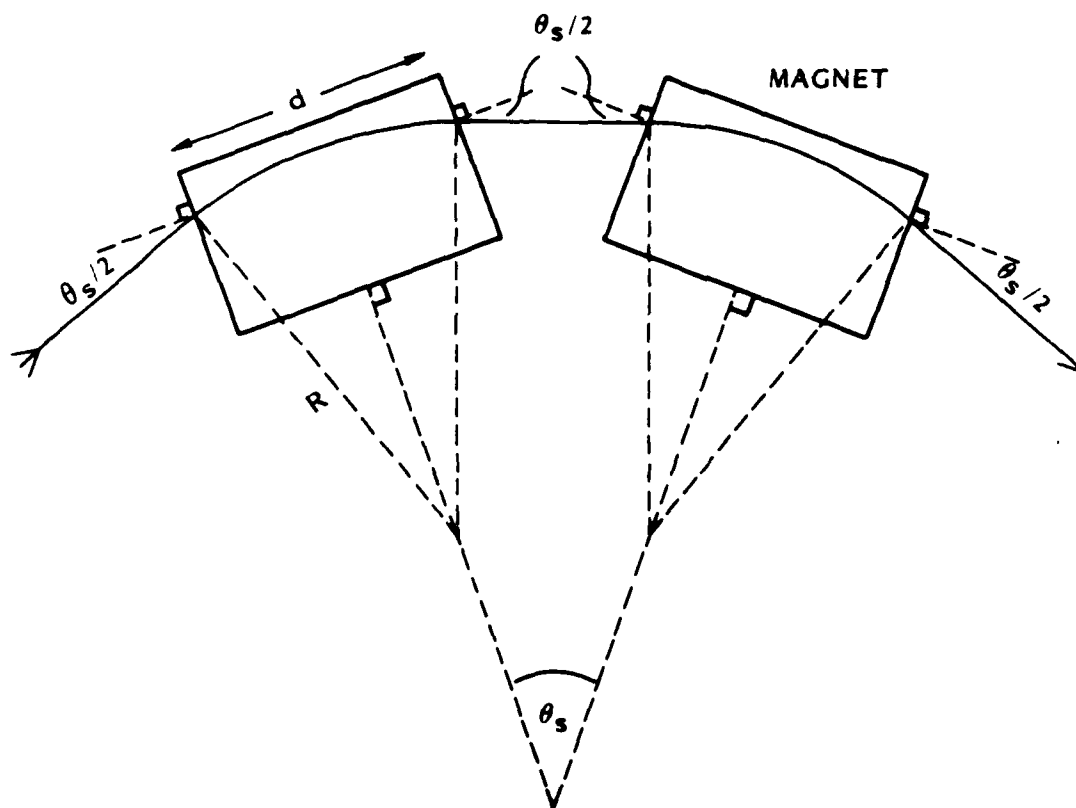
$$\alpha^{-1} = \left(1 - \frac{r_b^2}{a^2}\right) \left(\frac{1}{2} + \frac{1}{8} \frac{B_0^2}{B_z^2}\right) \quad (9)$$

Since B_z is proportional to the beam energy, the compaction factor rapidly approaches the weak-focusing limit if B_0 is not increased. In Eqs. (7)-(9) we have assumed $1 - n = 1/2$ where n is the external field index. However, the the external index in the IAPBT betatron is essentially equal to unity, as will be shown below. Thus, in the weak focusing limit, there is no transverse focusing on the beam. It will therefore be necessary to provide some significant solenoidal focusing throughout the acceleration. One important benefit of keeping the ratio B_0/B_z constant is that no orbital resonances are crossed. Such resonances were a severe problem in previous solenoidal lens betatron experiments by dePackh [12].

We can show geometrically that the external field index in the IAPBT betatron is effectively unity. The vertical field coils for the experiment are wound on cylindrical mandrels as shown in Fig. 16. Unlike the usual sector magnet [13], the ends are not canted. From Fig. 16, we see that the requirement for an equilibrium orbit is

$$\theta_{in} = \theta_{out} = \theta_s/2 \quad (10)$$

where θ_{in} , θ_{out} are the entering and exiting angles of the orbit at each magnet, and θ_s is the angle from the center of one magnet to the center of the next. This means that the radius of curvature of a particle inside the magnets must be



R-922

Figure 16. Particle orbit in the UNM solenoidal-lens betatron.

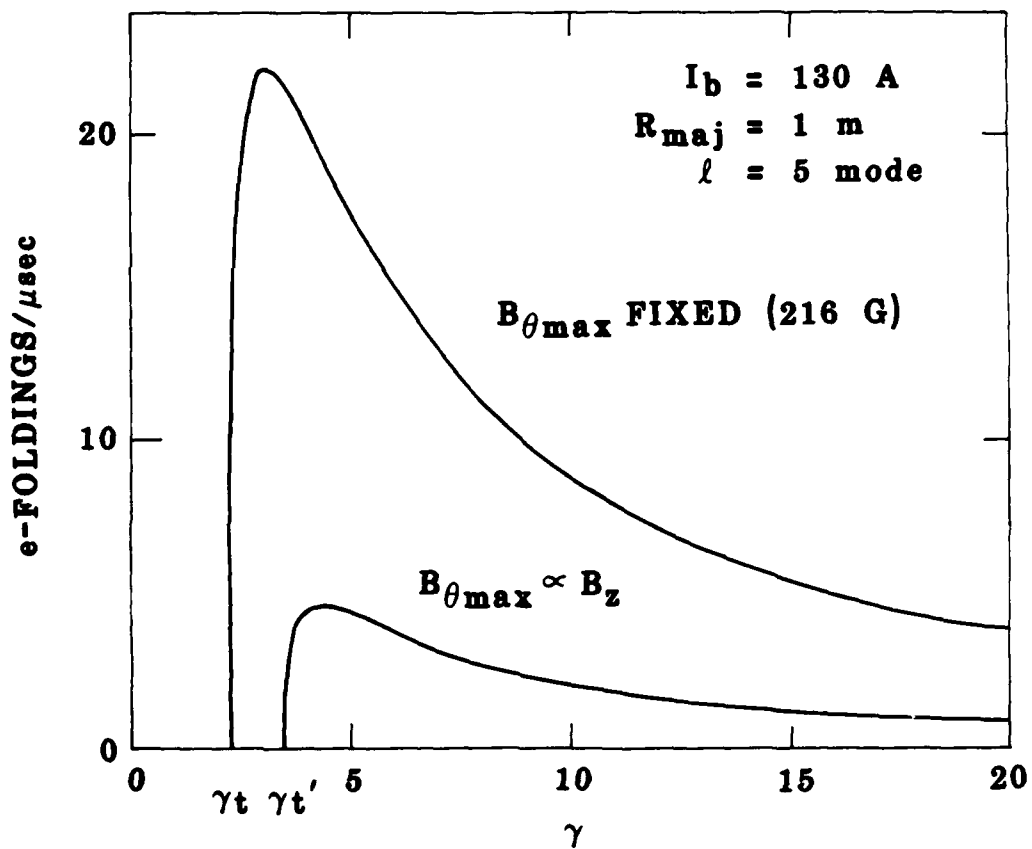
$$R = \frac{d}{2 \sin^{-1} \theta_s / 2} \quad (11)$$

where d is the length of the magnets. The vertical magnetic field has been experimentally measured to be uniform over a radial interval of ± 2 cm from the axis [13]. Thus, for a given particle energy, the equilibrium orbit conditions (10) and (11) can be satisfied for a continuum of radial particle positions. Intuitively, this follows from the fact that the path length inside the magnetic field is the same for all orbits satisfying Eq. (10), regardless of the length of the orbit circumference (see Fig. 16).

2. BEAM STABILITY IN THE IAPBT BETATRON

A general treatment of stability of the solenoidal lens betatron is complicated by the lack of toroidal symmetry in the equilibrium. One can overcome this problem in dealing with toroidal mode-numbers lower than that associated with the solenoidal fields by an averaging procedure. Details of this calculation are given in Appendix C. One finds that the net effect of the solenoidal lenses is to increase the radial and vertical focusing on the beam compared to a conventional betatron. Qualitatively, however, the beam behavior is similar to the conventional betatron in that the transverse oscillations are uncoupled. In the negative-mass simulations described below, we observe little motion along the z direction, unlike the modified betatron.

The analytic model in Appendix C predicts a finite negative-mass transition energy due to the strong-focusing, as in the stellatron [9]. Also like the stellatron, the strong focusing suppresses the peak growth rate of the instability. This is illustrated in Fig. 17, which shows the $\ell = 5$ growth rates for parameters close to those of the IAPBT betatron. These curves were obtained from the dispersion relation of Ref. 1 by setting $B_0 = 0$, and by adding the smoothed focusing effect of the solenoidal lenses into the expression for ω_r^2 :



VG-740

Figure 17. Growth rates of the $l = 5$ negative mass instability in the UNM solenoidal-lens betatron.

$$\omega_r^2 + \omega_r^2 + \frac{1}{8} \frac{B_0^2}{Y^2} \quad (12)$$

(The vertical focusing also increases, but the vertical oscillations decouple for $B_\theta = 0$.) Note that if the solenoidal focusing strength is kept at its initial high value by ramping the solenoidal field with the vertical field, then the peak growth rate is reduced by about a factor of five from the case where the solenoidal field is held fixed.

We have run a number of simulations to compare with the analytic predictions. A sinusoidal approximation to the reversing toroidal field was used, with the wavelength chosen to correspond to 30 solenoids around a 1 m radius torus. In the IAPBT betatron there are 40 solenoids, but 10 of these are on straight sections which we do not simulate here. First, we looked at the $\ell = 5$ mode on a 1 MeV, 100 A beam. The beam radius was 1.75 cm and the pipe radius was 4.5 cm. The peak solenoid field (134 gauss) was chosen to have a matched beam at 1 MeV. Essentially no growth of the instability was seen in a period of 230 ns. The theoretically predicted growth rate is $7.6 \times 10^{-4} \text{ cm}^{-1}$, which would produce about 5.3 e-foldings in 230 ns. (This growth rate is larger than those in Fig. 17 because of the lower solenoidal field.) We attribute the observed stability to the spread in particle circulation frequencies. Since the beam has no net poloidal rotation due to the alternating direction of the toroidal magnetic, Eq. (3) is always satisfied. Thus Eq. (2) should be an approximate stability criterion, as it is for the modified betatron (see Sec. II). Applying Eq. (2) to the present simulations, we obtain $8.75 \times 10^{-4} \text{ cm}^{-1}$ for the right-hand side, which is marginally sufficient for stability.

Assuming this is the correct reason for the lack of growth in the simulation, it is clear that finite beam radius is an important stabilizing mechanism in the IAPBT betatron. However, the beam radius shrinks as the beam is accelerated, particularly if the solenoidal field is ramped with B_z . For the latter case, the beam radius is approximately

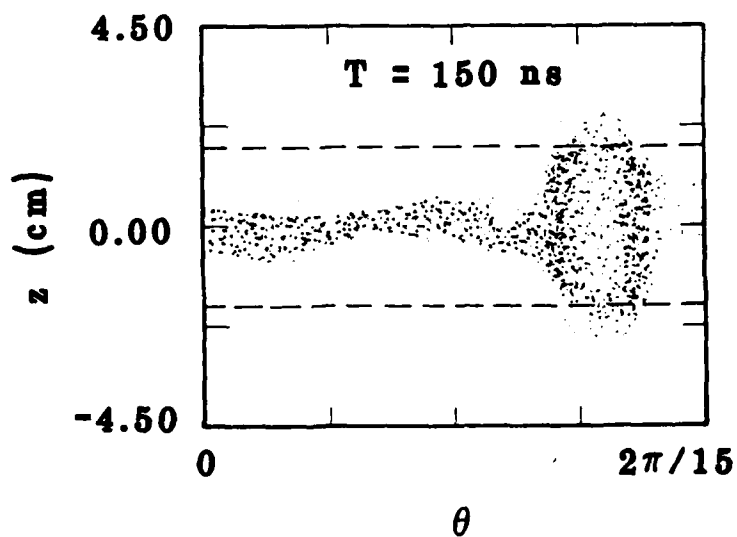
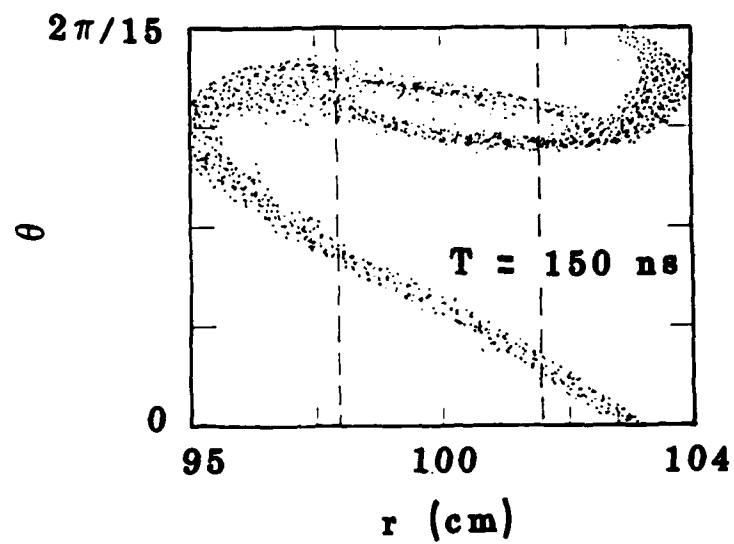
$$r_b = \frac{4}{B_0} \sqrt{\frac{v}{\gamma}} \propto \frac{1}{\gamma^{3/2}} \quad (13)$$

Therefore, we must trade off the increased stability from the strong focusing with the decreased stability due to shrinkage of the beam radius. For the case in Fig. 17, for example, Eq. (13) predicts that the beam radius will shrink from 2 cm at $\gamma = 1.6$ to 0.045 cm at $\gamma = 20$. From Eq. (2), we find that the $\ell = 5$ mode is still just marginally stable at $\gamma = 20$.

The smooth approximation to the focusing force becomes dubious as the mode-number ℓ approaches $N_s/2$, where N_s is the number of solenoids. However, since no approximation is made in the simulations, such modes can be looked at numerically. For the same beam parameters as above, we simulated the $\ell = 15$ ($= N_s/2$) mode, and observed a strong instability, with a growth rate of $2.2 \times 10^{-3} \text{ cm}^{-1}$. A particle plot from the nonlinear stage of the instability (Fig. 18) shows standard negative mass behavior, i.e., radial kinking accompanied by toroidal clumping. The instability has almost saturated at the point reached in Fig. 18, but 1/6 of the current has been scraped off onto the wall. If the wall radius had been larger, the instability might have saturated without current loss.

If we naively apply the analytic dispersion relation to the $\ell = 15$ mode, we obtain a growth rate of $2.2 \times 10^{-3} \text{ cm}^{-1}$, the same as the numerical growth rate. However, the right hand side of Eq. (2) gives $2.6 \times 10^{-3} \text{ cm}^{-1}$, thereby predicting stability due to thermal effects. Thus, it appears that the cold beam growth rate for $\ell = 15$ is significantly larger than that predicted by the analytic theory.

With respect to the negative-mass transition energy, on the other hand, the prediction of the analytic theory does seem to hold even at $\ell = 15$. We have simulated this mode at $\gamma = 1.6$, which is the injection energy for the IAPBT betatron, and observe no instability. The analytic theory predicts stability at least up to $\gamma = 2.2$ (cf. Fig. 17).



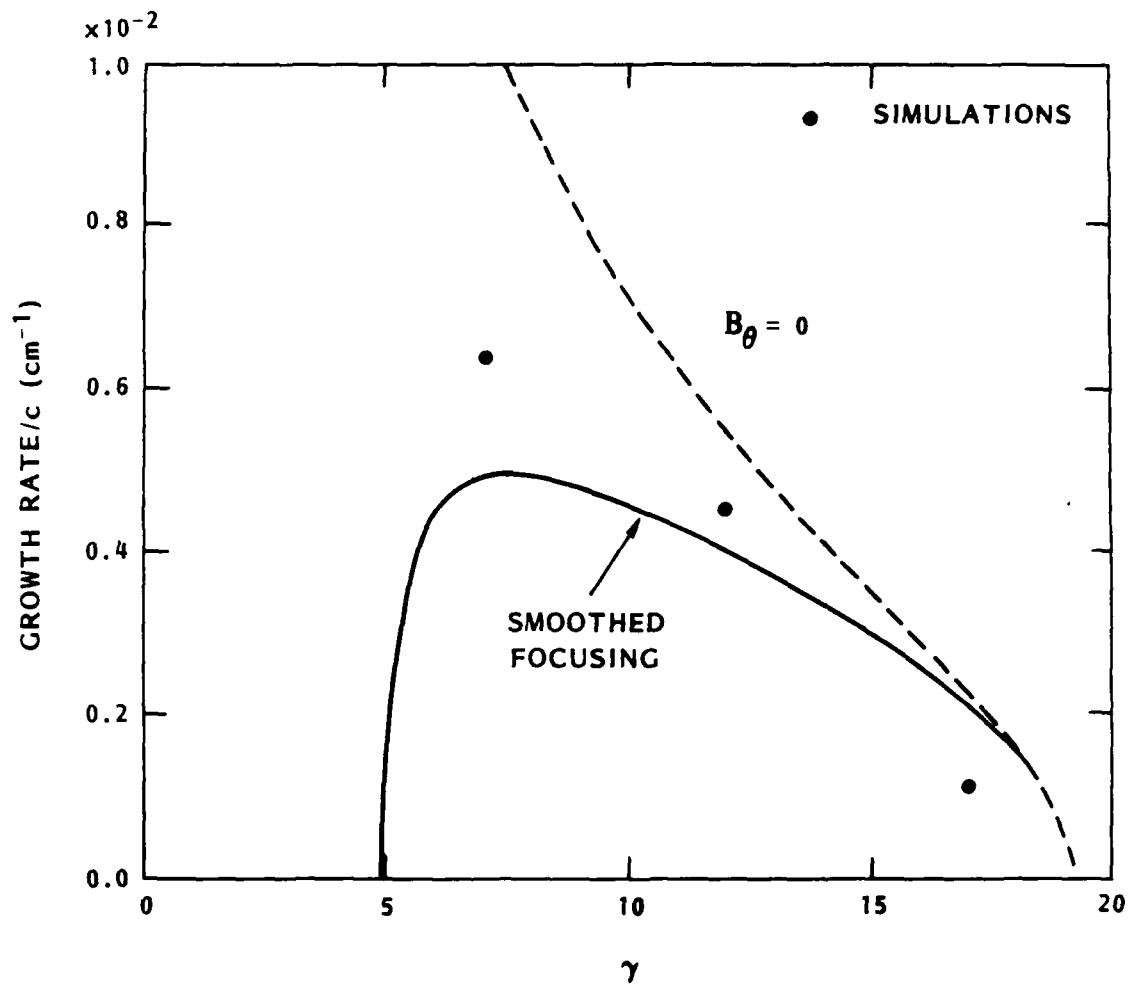
VG-696

Figure 18. Particle plot taken during the nonlinear stage of the $\ell = 15$ negative-mass instability for UNM betatron parameters.

3. HIGH CURRENT BEAM STABILITY

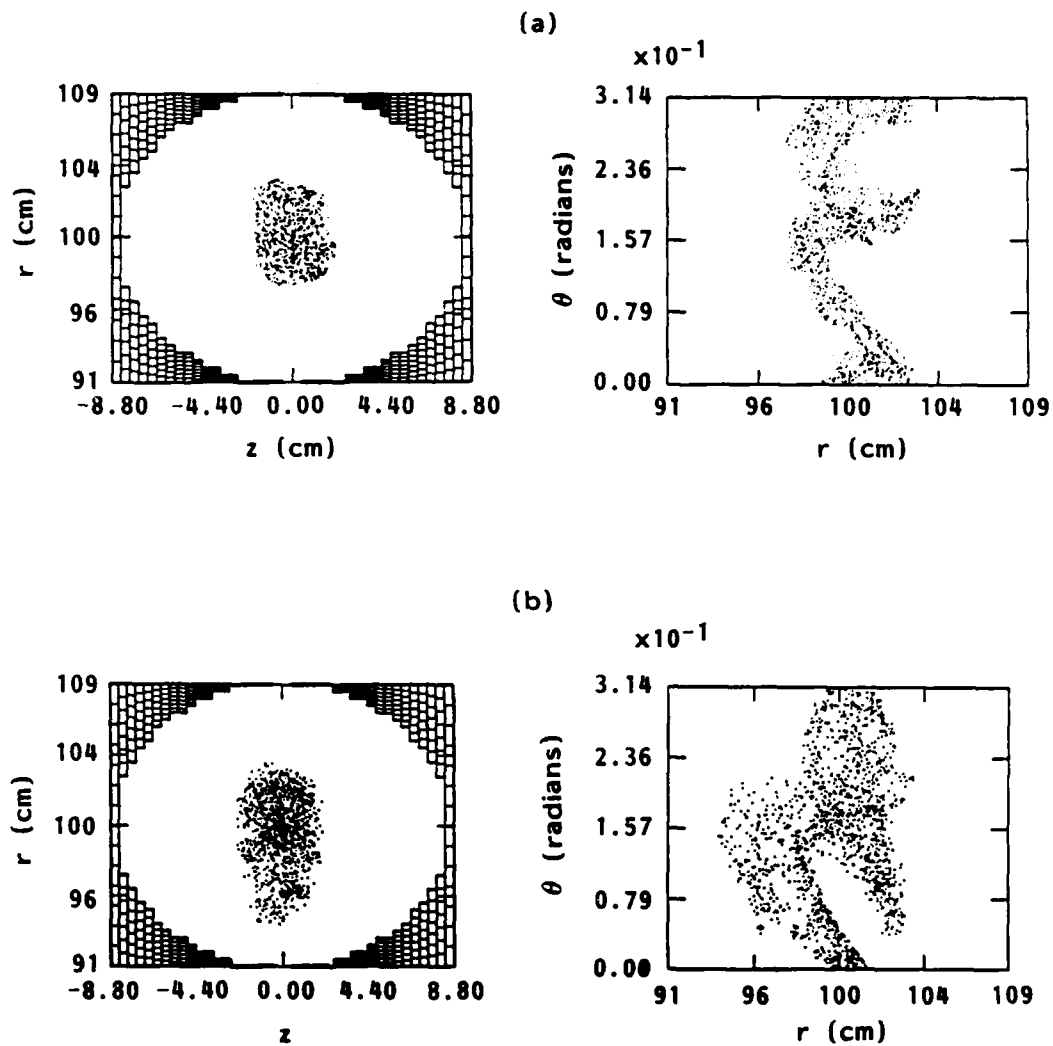
If the IAPBT experiments at 100 A are successful, then higher current experiments will be undertaken. We have performed a number of simulations at 10 kA to investigate negative-mass instability growth in this regime. In each of the simulations, we set the beam radius to 2 cm in order to have reasonably good resolution of the beam on a 50 x 50 mesh. This means that the solenoidal magnetic field necessary to get a matched beam decreases as the energy increases. Thus the linear growth rates, shown in Fig. 19, do not represent those experienced by an accelerating beam where the solenoidal field is kept constant, or ramped up. We assumed 20 solenoids around the torus, and simulated the mode $\ell = N_s = 20$. In Fig. 19, we compare the simulation results with (a) growth rates obtained for a conventional betatron with $B_0 = 0$, and (b) growth rates obtained by applying the smoothed approximation for the solenoidal lenses. As in the 100 A simulations described above, we find that the high- ℓ growth rates are anomalously large when thermal effects are taken into account. Nevertheless, the simulations for $\gamma = 7$ and $\gamma = 12$ both saturate in a manner similar to the 100 A case shown in Fig. 18, with little loss of current. Plots from the nonlinear stage of these simulations are shown in Fig. 20. There is considerable churning of the beam after these plots are taken, and this stage of the instability is probably not well represented by the single-mode simulation scheme. The simulation for $\gamma = 17$ was not run long enough to see saturation.

Experimental results from the UCI stellatron suggest that development of the negative-mass instability does not destroy the beam, and that most of the current can be accelerated beyond the point where the instability saturates. The above simulations suggest that this may also be true for the solenoidal lens betatron.



R-922

Figure 19. Comparison of simulation growth rates for the $\ell = 20$ mode on a 10 kA beam with analytic growth rates obtained for a conventional betatron (dashed line) and by extrapolation of the smoothed focusing result (solid line).



R-922

Figure 20. Nonlinear development of the $\ell = 20$ negative mass instability on a 10 kA beam in a solenoidal lens betatron. In (a), the beam energy is $\gamma = 7$ and in (b), $\gamma = 12$.

V. CONCLUSIONS

We have investigated thermal effects on the negative-mass instability in the modified betatron. For a monoenergetic beam, the stabilization is strongly dependent on the poloidal rotation frequency of the beam. When this frequency is close to zero, we observe total stabilization of the instability at high mode-numbers.

For parameters close to the NRL betatron at 1 kA, our calculations agree with the observed stability of the beam at the injection energy. We predict linear instability at low toroidal mode-numbers as the beam is accelerated above 1 MeV. The nonlinear development of the instability is unknown for a 1 kA beam. Simulations of 10 kA beams show loss of 50% or more of the beam current at low energies. Several kiloamperes remain circulating after the instability has saturated, so that a 1 kA beam may be able to survive without current loss, although deterioration of beam quality is to be expected.

We have simulated beam stability at high energies and high ℓ -numbers, in the regime of the so-called hybrid instability. In all such simulations for 10 kA beams, we observe saturation of the instability without loss of beam current. There is much less transverse kinking of the beam than in the negative-mass instability regime which occurs at lower energies.

Calculations for the UCI stellatron show that the presence of background ions has a larger stabilizing effect on the negative-mass instability than the helical quadrupole field. The predicted energy for onset of the negative-mass instability is in agreement with experimental observations. Most of the beam current is observed to survive the disruption due to the instability, but the effect on beam quality has not been measured.

A three-wave electromagnetic interaction was discovered in the stellatron. For high currents and strong focusing, its growth rate can be very large. However, it is possible to choose parameters such that the

interaction is pushed out to large mode-numbers, where thermal effects may stabilize it.

A theory of the negative-mass instability in the solenoidal lens betatron was derived using a smooth approximation for the focusing effects of the solenoidal lenses. The theory predicts stability for the 100 A UNM betatron from its injection energy, $\gamma = 1.6$, to $\gamma = 2.2$. Above this energy, simulations show a strong negative-mass instability, which produces a transverse kink on the beam with an amplitude comparable to the wall radius. Some current loss results. Simulations with currents up to 10 kA show similar results, suggesting that most of the current can survive the instability.

REFERENCES

1. T. P. Hughes and B. B. Godfrey, AMRC-R-655, Mission Research Corporation, December, 1984 (DTIC No. A151420).
2. J. Golden, R. Mako, L. Floyd, T. Smith, D. Dialetis, S. J. Marsh, and C. A. Kapetanakis, Proc. 1987 Particle Accelerator Conference (Washington, D. C., 1987); Bull. Am. Phys. Soc. 32, 173 (1987).
3. H. Ishizuka, A. Fisher, K. Kamada, R. Prohaska, Y. Song, and N. Rostoker, *ibid.* p. 200.
4. S. Humphries, Jr. and L. K. Len, *ibid.* p. 205.
5. F. Mako, J. Golden, D. Dialetis, L. Floyd, N. King, and C. A. Kapetanakis, Proc. NATO Advanced Study Institute, Pitlochry, Scotland (1986).
6. B. B. Godfrey and T. P. Hughes, Phys. Fluids 28, 669 (1985).
7. P. Sprangle and D. Chernin, Part. Accel. 15, 35 (1984).
8. J. M. Finn and W. M. Manheimer, Phys. Fluids 26, 3400 (1983).
9. D. Chernin, Phys. Fluids 29, 556 (1986).
10. H. Ishizuka, J. Saul, A. Fisher and N. Rostoker, Proc. Beams '86 Conference, p. 722 (Kobe, Japan, 1986).
11. V. Bailey, L. Schlitt, S. Putnam, A. Mondelli and D. Chernin, Proc. 1987 Particle Accelerator Conference (Bull. Am. Phys. Soc. 32, 172 1987).
12. D. C. dePackh, NRL Report 5751 (Naval Research Laboratory, Washington, DC, 1962).
13. J. D. Lawson, The Physics of Charged Particle Beams (Clarendon Press, Oxford, 1978).
14. L. K. Len and S. Humphries, Jr., IAPBT Betatron Project Technical Note 5 (February 20, 1986).

APPENDIX A

ELECTROMAGNETIC INSTABILITY IN A QUADRUPOLE-FOCUSING ACCELERATOR

Electromagnetic instability in a quadrupole-focusing accelerator

Thomas P. Hughes and Brendan B. Godfrey
Mission Research Corporation, 1720 Randolph Road, S. E., Albuquerque, New Mexico 87106

(Received 18 October 1985; accepted 10 February 1986)

The addition of helical quadrupole focusing to a modified betatron configuration is shown to give rise to an electromagnetic instability under certain conditions. The instability arises from a three-wave coupling between the helical field, a transverse mode on the beam, and a transverse-electric waveguide mode. An analytic dispersion relation is derived. Several features of the instability are confirmed using three-dimensional computer simulations.

I. INTRODUCTION

Betatrions and other recirculating accelerator designs have been studied in recent years as compact accelerators for high-current electron beams.¹⁻⁶ Conventional⁷ and modified¹ betatrions require precise matching of the beam energy to the vertical magnetic field if a fixed major radius is to be maintained. To overcome this restriction, strong focusing in the form of a helical magnetic quadrupole has been added to the modified betatron configuration.^{3,8} This considerably increases the tolerance of the device to mismatch. In this paper, we show that helical quadrupole focusing can lead to an electromagnetic instability arising from a three-wave interaction between the static helical field, a transverse mode on the beam, and a transverse-electric (TE) waveguide mode. This behavior is reminiscent of that which occurs in planar geometry in the presence of a rippled magnetic field.⁹ Unlike the free-electron laser instability, which was recently analyzed in the presence of helical quadrupole focusing,¹⁰ longitudinal bunching of the beam plays no significant role in the instability that we describe here. Also, the instability is essentially independent of the radius of curvature of the device. It is thus not related to the negative-mass instability, for example. The main effect of finite radius of curvature is to discretize the toroidal mode numbers. This can be important, since if the instability width is narrow enough, it can fall between two allowed mode numbers and disappear (see Sec. II).

In Sec. II, we give an analytic theory of the instability. In Sec. III, we obtain a simplified dispersion relation that yields an instability criterion. Section IV details comparisons between the analytic theory and three-dimensional particle simulations. Section V gives our conclusions.

In writing down equations, we use convenient units, where the electron charge e , mass m , and velocity of light c are scaled out. Lengths are normalized to $c/\omega_0 \equiv 1$ cm, frequencies to ω_0 , velocities to c , densities to $\omega_0^2 m/4\pi e^2$, and electric and magnetic fields to $mc\omega_0/e$. To get frequencies and growth rates in sec^{-1} , multiply the normalized values by 3×10^{10} .

II. ANALYTIC MODEL OF INSTABILITY

The geometry and coordinate system we use are illustrated in Fig. 1. An electron ring of major radius R and minor radius a circulates around the center of a conducting toroidal cavity whose major and minor radii are R and b , respectively.

The externally applied magnetic fields consist of a vertical field $B_z \propto r^{-s}$, where s is the so-called field index (we assume $s = 1/2$), a solenoidal field B_θ , and a helical quadrupole field B_q . This is the configuration of the stellatron accelerator.³ A configuration where the helical quadrupole field is generated by two current-carrying wires instead of four has also been proposed.⁶ We assume that the beam can be modeled as a string of rigid disks. This means that we follow the transverse motion of the beam centroid, and ignore any internal dynamics. This treatment is valid provided the drift-tube minor radius is much greater than the beam radius, $b \gg a$, since the fields we need to consider have a transverse scale length $\sim b$. We ignore the perturbed θ motion of the beam under the assumption of relativistic stiffness in this direction, i.e., $\gamma \gg 1$, where γ is the beam relativistic factor.

In equilibrium, the matched value of the vertical magnetic field is $B_z = \gamma V_\theta/R$, where V_θ is the toroidal beam velocity. Linearizing about the equilibrium position, we obtain the following equations of motion for the perturbed coordinates \bar{r} , \bar{z} of the beam centroid³:

$$\ddot{\bar{r}} + \frac{1}{2} \Omega_z^2 \bar{r} - \Omega_\theta \dot{\bar{z}} + \mu \Omega_z^2 (\bar{r} \cos m\theta + \bar{z} \sin m\theta) = (-\bar{E}_r - V_\theta \bar{B}_z)/\gamma, \quad (1)$$

$$\ddot{\bar{z}} + \frac{1}{2} \Omega_z^2 \bar{z} + \Omega_\theta \dot{\bar{r}} + \mu \Omega_z^2 (\bar{r} \sin m\theta - \bar{z} \cos m\theta) = (-\bar{E}_z + V_\theta \bar{B}_r)/\gamma, \quad (2)$$

where a dot denotes the total time derivative $\partial/\partial t + (V_\theta/R)\partial/\partial\theta$, $\Omega_z = B_z/\gamma$, $\Omega_\theta = B_\theta/\gamma$, \bar{E} and \bar{B} denote the perturbed self-electric and self-magnetic fields acting on

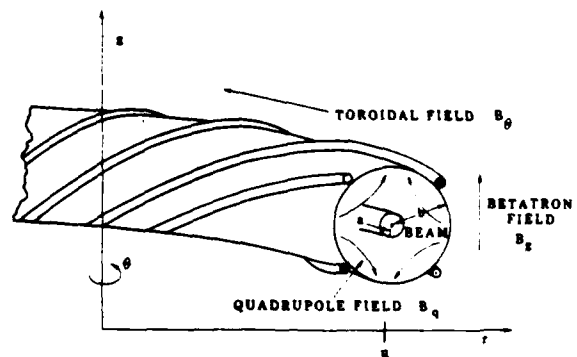


FIG. 1. Geometry of stellatron accelerator showing conducting toroidal cavity and externally applied magnetic fields.

the beam at the perturbed position, and μ denotes the amplitude of the quadrupole field index. The quadrupole field index is a normalized measure of the transverse gradient of the quadrupole field. It is defined by $(R/B_z)(\partial B_{\theta}/\partial r)$ evaluated at $r=R$, and has the form $\mu \cos m\theta$. Letting $\xi \equiv \bar{z} + i\bar{r}$, Eqs. (1) and (2) can be written as

$$\begin{aligned} \dot{\xi} + \frac{1}{2}\Omega_z^2 \xi - i\Omega_\theta \dot{\xi} - \mu\Omega_z^2 e^{-im\theta} \xi^* \\ = -[\tilde{E}_z + i\tilde{E}_r + iV_\theta(\tilde{B}_z + i\tilde{B}_r)]/\gamma, \end{aligned} \quad (3)$$

where $*$ denotes the complex conjugate. To calculate \tilde{E} and \tilde{B} , we use a Green's function approach. Maxwell's equations can be written as

$$\nabla \times \nabla \times \mathbf{E} - \omega^2 \mathbf{E} = i\omega \mathbf{J}, \quad (4)$$

$$\mathbf{B} = -(i/\omega) \nabla \times \mathbf{E}, \quad (5)$$

where we assume an $e^{-i\omega t}$ dependence for the perturbed fields and currents. The solution to Eq. (4) can be written down by using a dyadic Green's function,¹¹ constructed from the solutions to the homogeneous counterpart of Eq. (4). The expressions obtained are infinite series.¹¹ In this paper, we will deal only with the interaction of the beam with the lowest electromagnetic waveguide mode, i.e., the TE_{11} mode. Therefore, we extract from the infinite series for the fields those terms containing the TE_{11} resonance. All other self-field contributions are neglected. This procedure is equivalent to treating the beam as a weak perturbation of the vacuum TE_{11} eigenmode. For example, the expression for the $e^{i\theta}$ component of \tilde{E} , evaluated at the location of the beam is

$$\tilde{E}_r = -v\omega(\omega - l\Omega_z) \bar{r} \frac{J_1}{\eta_{11}^2 + l^2/R^2 - \omega^2} + O\left(\frac{b}{R}\right), \quad (6)$$

where

$$I_\eta^{-1} = \frac{1}{2}(b^2 - \eta_{11}^2) J_1^2(\eta_{11}b)$$

(where J_1 is a Bessel function), η_{11} denotes the lowest root of $J_1'(\eta b) = 0$, and $O(b/R)$ denotes toroidal corrections, which we neglect under the assumption $R \gg b$. Also, v is Budker's parameter, i.e., the number of electrons per unit length of the beam times the classical electron radius. In deriving Eq. (6), we have used the rigid-disk approximation to write $J_r = -\rho \dot{r} = i(\omega - l\Omega_z) \rho \bar{r}$, where ρ is the beam density. Similar expressions are obtained for the other fields.

We now proceed to solve Eq. (3) by writing ξ in the form

$$\xi = \sum_r \xi_r^+ e^{i\theta - i\omega t} + \xi_r^- e^{i\theta + i\omega t}, \quad (7)$$

where $+$, $-$ refer to "forward" and "backward" waves, respectively. Substituting this into Eq. (3), we obtain the coupled equations

$$\begin{aligned} \left(-\Omega_+^2 + \frac{1}{2}\Omega_z^2 - \Omega_+ \Omega_\theta + \frac{\alpha\Omega_+^2}{\omega^2 - \eta_{11}^2 - l^2/R^2}\right) \xi_r^+ \\ - \mu\Omega_z^2 (\xi_{r-m-l}^-)^* = 0, \end{aligned} \quad (8a)$$

$$\begin{aligned} \left(-(\Omega_+ - m\Omega_z)^2 + \frac{1}{2}\Omega_z^2 + (\Omega_+ - m\Omega_z)\Omega_\theta\right. \\ \left.+ \frac{\alpha(\Omega_+ - m\Omega_z)^2}{\omega^2 - \eta_{11}^2 - (l+m)^2/R^2}\right) \end{aligned}$$

$$\times \xi_{r-m-l}^- - \mu\Omega_z^2 (\xi_r^+)^* = 0, \quad (8b)$$

$$\left(-\Omega_-^2 + \frac{1}{2}\Omega_z^2 + \Omega_- \Omega_\theta + \frac{\alpha\Omega_-^2}{\omega^2 - \eta_{11}^2 - l^2/R^2}\right)$$

$$\times \xi_r^- - \mu\Omega_z^2 (\xi_{r+m-l}^+)^* = 0, \quad (8c)$$

$$\begin{aligned} \left(-(\Omega_- + m\Omega_z)^2 + \frac{1}{2}\Omega_z^2 - (\Omega_- + m\Omega_z)\Omega_\theta\right. \\ \left.+ \frac{\alpha(\Omega_- + m\Omega_z)^2}{\omega^2 - \eta_{11}^2 - (l+m)^2/R^2}\right) \\ \times \xi_{r+m-l}^+ - \mu\Omega_z^2 (\xi_r^-)^* = 0, \end{aligned} \quad (8d)$$

where $\Omega_\pm = \omega \mp l\Omega_z$ and $\alpha = vI_\eta/\gamma \approx 8.4v/\gamma b^2$. Note that this is a closed system of equations, in which only mode numbers l and $-m-l$ appear. This is a consequence of the complex-conjugate sign appearing in Eq. (3). Further, note that ξ_r^+ is coupled only to ξ_{r-m-l}^- , and ξ_r^- is coupled only to ξ_{r+m-l}^+ . Thus, the 4×4 matrix of Eq. (8) splits into two 2×2 matrices. The determinant of one 2×2 matrix gives the dispersion relation

$$\begin{aligned} \left(\Omega_+^2 - \frac{1}{2}\Omega_z^2 + \Omega_+ \Omega_\theta - \frac{\alpha\Omega_+^2}{\omega^2 - \eta_{11}^2 - l^2/R^2}\right) \\ \times \left((\Omega_+ - m\Omega_z)^2 - \frac{1}{2}\Omega_z^2 - (\Omega_+ - m\Omega_z)\Omega_\theta\right. \\ \left.- \frac{\alpha(\Omega_+ - m\Omega_z)^2}{\omega^2 - \eta_{11}^2 - (l+m)^2/R^2}\right) - \mu^2 \Omega_z^4 = 0. \end{aligned} \quad (9)$$

The determinant of the other 2×2 matrix can be obtained from Eq. (9) by letting $\omega \rightarrow -\omega$. Having obtained a root for ω from Eq. (9), the corresponding normal mode for ξ can be obtained from Eqs. (8a) and (8b), and is a linear combination of two terms with space-time dependencies $\exp(i\theta - i\omega t)$ and $\exp[-i(m+l)\theta + i\omega t]$, respectively.

Multiplying out the dispersion relation in Eq. (9), we obtain an eighth-degree polynomial in ω . Numerical solution for the sample parameters in Table I gives the set of curves shown in Fig. 2. The parameter ϵ (which is frequently used by stellarator physicists) in Table I is related to μ by $\mu = \epsilon m \Omega_\theta / 2\Omega_z$. The curves can be classified as follows:

Electromagnetic modes:

$$\omega^2 \approx \eta_{11}^2 + l^2/R^2, \quad \eta_{11}^2 + (m+l)^2/R^2,$$

Cyclotron modes:

$$\omega \approx (m+l)\Omega_z + \Omega_\theta, \quad l\Omega_z - \Omega_\theta. \quad (10)$$

Low-frequency transverse modes:

$$\omega \approx (m+l)\Omega_z - \omega_B, \quad l\Omega_z + \omega_B,$$

TABLE I. High-current stellarator parameters used in particle simulations.

Torus major radius	1 m
Torus minor radius	8.4-9.5 cm
Beam major radius	1 m
Beam minor radius	2 cm
Beam current (I)	300 A-10 kA
Beam energy (γ)	7
Toroidal magnetic field	5 kG
Vertical magnetic field	118 G
Quadrupole field (ϵ)	0.7
Quadrupole mode number (m)	14-30

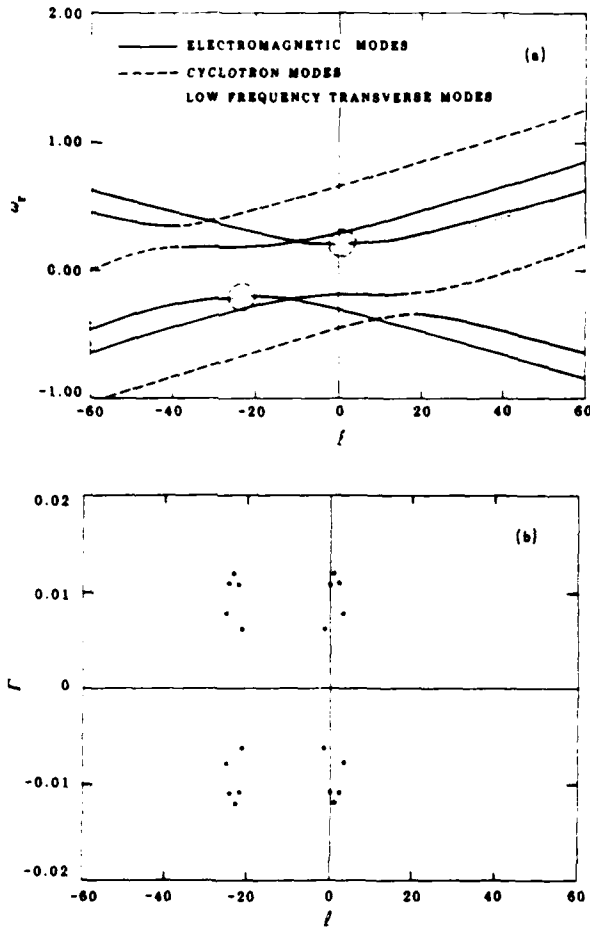


FIG. 2. Frequencies and growth rates, denoted by ω , and Γ , respectively, obtained from Eq. (9) for Table I parameters with $b = 8.8$, $l = 10$ kA, $m = 22$. In (a), the two unstable interactions are circled. In (b), growth rates at integer (allowed) values of l are shown. Multiply ω , Γ by 3×10^{10} to get values in units of sec^{-1} .

$$-2\omega_{11}(\omega_{11} - l\Omega_z)(\omega_{11} - l\Omega_z + \Omega_\theta)\Omega_\theta\delta^2 + \{2\omega_{11}(\omega_{11} - l\Omega_z)(\omega_{11} - l\Omega_z + \Omega_\theta)[(l+m)\Omega_z - \omega_{11}]\Omega_\theta + (\omega_{11} - l\Omega_z)^2\alpha\Omega_\theta - 2\omega_{11}\mu^2\Omega_z^4\}\delta - \alpha(\omega_{11} - l\Omega_z)^2[(m+l)\Omega_z - \omega_{11}]\Omega_\theta = 0. \quad (12)$$

Defining the quantities $\gamma_1, \gamma_2, \gamma_3$ by

$$\gamma_1 = 2\omega_{11}(\omega_{11} - l\Omega_z)(\omega_{11} - l\Omega_z + \Omega_\theta) \times [(l+m)\Omega_z - \omega_{11}]\Omega_\theta, \quad (13)$$

$$\gamma_2 = \alpha(\omega_{11} - l\Omega_z)^2\Omega_\theta, \quad \gamma_3 = 2\omega_{11}\mu^2\Omega_z^4,$$

the condition for instability can be written as

$$(\gamma_1 + \gamma_2 - \gamma_3)^2 < 4\gamma_1\gamma_2, \quad (14a)$$

or, equivalently,

$$(\gamma_1 - \gamma_2 - \gamma_3)^2 < 4\gamma_2\gamma_3. \quad (14b)$$

Equations (12)–(14) allow us to make some more exact statements about the conditions for instability. From Eqs. (13) and (14b), we see that the instability disappears for $\mu = 0$, as one would expect. Equation (14a) shows that $(l+m)\Omega_z > \omega_{11}$ (i.e., $\gamma_1 > 0$) is required for instability (as-

suming $\Omega_\theta > 0$; the case $\Omega_\theta < 0$ is discussed later). This means that the instability turns on when the frequency of the transverse beam mode is somewhat above the TE_{11} eigenfrequency, rather than exactly equal to it. To see how the instability turns off as l increases, we rewrite Eq. (14a) to obtain

$$\mu^2 > (\sqrt{\gamma_1} - \sqrt{\gamma_2})^2 / 2\omega_{11}\Omega_z^4 \quad (15)$$

as the criterion for instability. The term γ_1 is sensitive to the value of l through the factor $(l+m)\Omega_z - \omega_{11}$. As l increases, γ_1 eventually becomes large enough to violate this inequality, and the instability disappears (cf. Fig. 2). Equation (15) also shows that as $\nu \rightarrow 0$ (so that $\gamma_2 \rightarrow 0$) and $\mu \rightarrow 0$, the unstable region in l space becomes narrower. If l were a continuous variable, then the instability would persist near $(l+m)\Omega_z = \omega_{11}$ as long as ν and μ were finite. Since l is

where $\omega_B \approx 1/4\Omega_z^2/\Omega_\theta$. These approximate forms are based on the assumption $\Omega_\theta \gg \Omega_z$, which is satisfied for typical stelleron parameters.

It can be shown from Eq. (9), and is apparent from Fig. 2, that the dispersion relation is symmetrical about the line $l = -m/2$ (m is an even integer, equal to twice the number of minor turns the helical conductors make in going one major turn around the torus). More precisely, if we define $l' = l + m/2$, then $\omega \rightarrow -\omega^*$ as $l' \rightarrow -l'$. In the following, we will look only at $l' > 0$. Results for $l' < 0$ follow by symmetry.

Instability occurs as a result of the intersection of the curve $\omega \approx (m+l)\Omega_z - \omega_B$ with the electromagnetic mode $\omega \approx (\eta_{11}^2 + l^2/R^2)^{1/2}$. The instability can be thought of as a parametric process¹² in which the quadrupole field plays the role of a pump wave. If we denote the three interacting modes by subscripts 1,2,3 then we get the following frequencies and mode numbers:

Pump wave:

$$\omega_1 = 0, \quad k_1 = m/R,$$

Electromagnetic wave:

$$\omega_2 = (\eta_{11}^2 + l^2/R^2)^{1/2}, \quad k_2 = l/R, \quad (11)$$

Slow transverse wave:

$$\omega_3 \approx (m+l)\Omega_z, \quad k_3 = (m+l)/R,$$

where we have neglected the small ω_B term in ω_3 . In terms of this picture, instability occurs when the usual matching conditions are approximately satisfied ($\omega_1 + \omega_2 = \omega_3$, $k_1 + k_2 = k_3$). Energy for the instability is provided by the beam via the negative-energy slow transverse mode.

III. DERIVATION OF INSTABILITY CRITERION

An approximate expression for the growth rate can be obtained by letting $\omega = \omega_{11} + \delta$, where $\omega_{11} = (\eta_{11}^2 + l^2/R^2)^{1/2}$, in Eq. (9), and keeping terms to order δ^2 . This gives the quadratic expression

discrete in a toroidal system, however, the unstable region can fall between two integer values of l , and no instability would be seen.

Finally, from Eqs. (12) and (14a), the peak growth rate as a function of μ is found when μ is chosen so that $\gamma_1 + \gamma_2 - \gamma_3 = 0$. The growth rate Γ is then given by

$$\Gamma^2 = \frac{\alpha}{2} \frac{[(m+l)\Omega_z - \omega_{11}](\omega_{11} - l\Omega_z)}{\omega_{11}(\omega_{11} - l\Omega_z + \Omega_\theta)} \quad (16)$$

For the parameters of Fig. 2, this equation predicts $\Gamma = 1.06 \times 10^{-2}$ ($3.18 \times 10^8 \text{ sec}^{-1}$ in cgs units) for $l = 0$, in good agreement with the exact result of 1.12×10^{-2} , which occurs for $\epsilon = 0.8$ ($\mu \approx 380$).

Thus far, we have assumed $\Omega_\theta > 0$. If Ω_θ is negative, then Eq. (14b) shows that the instability disappears. This is to be expected since the slow transverse wave then becomes a fast, positive-energy wave. At the same time, the cyclotron wave $\omega \approx (m+l)\Omega_z + \Omega_\theta$ becomes a slow wave, with the potential for an unstable interaction. We have not examined this case, however, since previous calculations³ have shown that the parameter space in which single-particle orbits are stable shrinks greatly when the sign of Ω_θ is opposite to that of m .

IV. COMPARISON WITH NUMERICAL SIMULATIONS

To verify the above analytic calculations, we have performed three-dimensional numerical particle simulations with the code IVORY.¹³ In IVORY, field quantities are represented on a spatial mesh in the r - z plane, and by Fourier modes in the θ direction. A given field component thus has the form

$$F(r, \theta, z, t) = \sum_n f_n(r, z, t) \cos n\theta + g_n(r, z, t) \sin n\theta. \quad (17)$$

The number of Fourier modes kept in the sum depends on the problem. At a minimum, we must retain those modes that the linear theory indicates are coupled together. In addition, the $n = 0, m$ modes must be kept since the equilibrium fields contain components in these modes. The self-consistent fields of the beam are advanced in time using the full Maxwell equations. Particles are advanced using the full Lorentz force equations. The stellatron fields are computed from analytic expressions.³

In deciding on parameters for the simulations, computing costs constrained us to choose cases that minimize the running time and storage requirements. Thus, we concentrated on cases with large expected growth rates. In addition, we either chose $l = 0$, or chose $m + l$ to be a small integer multiple of l . (Recall that l denotes the TE_{11} wave mode number.) This minimizes the number of particles needed to resolve the different mode numbers. For $l = 0$, for example, we see from Eqs. (11) and (17) that only mode numbers 0, m must be represented in the simulations.

Choosing $l = 0$, we used the parameters in Table I with $b = 8.8$ and a 10 kA beam current, and performed simulations for different values of the quadrupole mode number m . The growth rates obtained are plotted in Fig. 3 versus those obtained from Eq. (9). We also show the growth rate from a

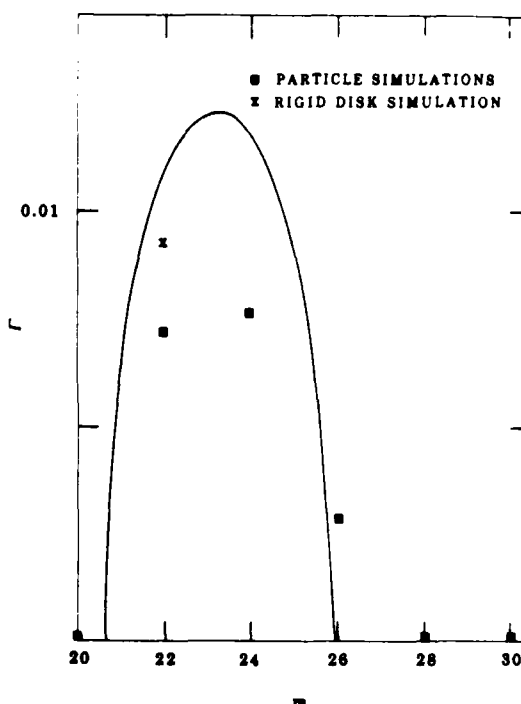


FIG. 3. Growth rates of instability versus quadrupole mode number m (which must be an even integer) for parameters in Table I, and $b = 8.8$, $I = 10$ kA. Theoretical results (solid line) are compared to simulation code results.

simulation for $m = 22$ in which the beam was represented by a string of rigid disks in the code, instead of the more realistic particle representation. There are at least two possible reasons why agreement with the analytic result is better for the rigid disk simulation. First, the initial field energy level is lower for the latter as a result of the absence of internal degrees of freedom of the beam, so that there is a longer visible period of linear growth. In the simulations with particles, the field energy increases only about one order of magnitude over its initial value before saturating, as shown in Fig. 4.

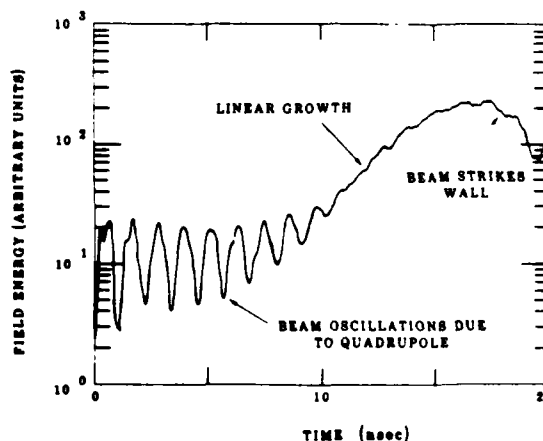


FIG. 4. Energy in $n = 22$ field components (n = toroidal mode number) versus time showing development of $l = 0, m = 22$ instability in Fig. 2. This plot was generated by the simulation code IVORY.

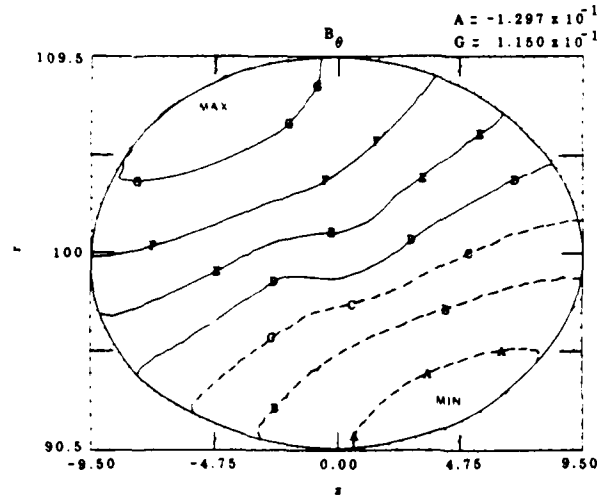


FIG. 5. Contour plot of $n = 0$ component of toroidal self-magnetic field B_θ during early nonlinear growth of an $l = 0$, $m = 20$ instability. The contours have linearly increasing values from A to G . The structure is that of a TE_{11} mode. The distortion of contours in the center is a result of the presence of the beam.

This means that the growth measured may not be truly exponential. Second, in the particle simulations there is a spread in the energy of the particles as a result of space charge, giving rise to a spread in transverse oscillation frequencies. This may have a stabilizing effect.

There is good agreement between simulations and theory as to the turn-on and turn-off of the instability. The TE_{11} cutoff frequency for the drift tube is $\eta_{11} \approx 1.84/b \approx 0.21$. Figure 3 shows that, in agreement with the analytic prediction (Sec. III), instability sets in for $m > \eta_{11}/\Omega_r \approx 21$. No instability is seen during the length of the simulations for $m > 26$ (we ran cases for $m = 28, 30$).

Further evidence of the electromagnetic character of the instability comes from two $l = 0$ simulations where the minor cross section of the drift tube was varied, keeping m fixed. For $m = 20$, $I = 10$ kA, $b = 8.8$ (other parameters as in Table I), no growth was observed, since $m\Omega_r < \eta_{11}$. On increasing the minor radius to 9.5, η_{11} decreased to give $m\Omega_r \geq \eta_{11}$, and strong growth was observed. In addition, a contour plot of the magnitude of the $n = 0$ component of the perturbed B_θ , shown in Fig. 5, shows the $\sin(\phi + \phi_0) \times J_1(\eta_{11}, \rho)$ dependence of a TE_{11} mode. Here, ρ, ϕ are polar coordinates in the plane of Fig. 5, and ϕ_0 is a phase factor.

In order to see whether the aspect ratio of the torus affects the instability, we increased the major radius R first to 10^3 and then to 10^4 , keeping m/R fixed at 0.22 and choosing $l = 0$. No significant change in the growth rate was observed in the simulations. This is in contrast to the negative-mass instability,¹⁴ where the growth rate goes to zero as $R \rightarrow \infty$.

Next, we tested the $\nu^{1/2}$ dependence of the growth rate on the beam current predicted by Eq. (16). The parameters in Table I with $b = 9.0$, $m = 22$ were used to perform simulations at 300 A, 1 kA, and 10 kA beam currents. The results in Fig. 6 show that the predicted scaling is supported by the simulations.

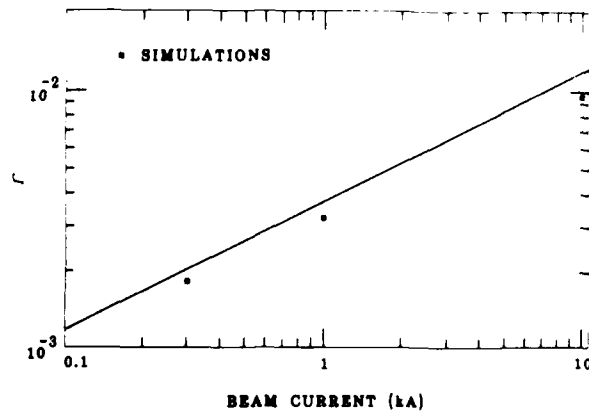


FIG. 6. Growth rate of instability versus beam current for Table I parameters with $m = 22$, $b = 9.0$. Simulation results are compared to theoretical prediction.

Thus far, we have reported on results for $l = 0$. Now, we look at a case for which $l = m = 14$. The dispersion diagram for this case, obtained from Eq. (9), is similar to that in Fig. 2, except that one of the unstable regions occurs around $l = 14$. The simulation parameters used are those in Table I, with $I = 10$ kA, $b = 8.4$ chosen to enhance the growth rate. From Eqs. (11) and (17), we see that mode numbers 0, 14, 28 must be represented in the simulation code. Field energy in the modes $n = 14, 28$ is observed to grow exponentially at a rate $\Gamma = 6.3 \times 10^{-3}$, compared to the analytic rate 7.8×10^{-3} . In this case, it is the $n = 14$ field plots that show a TE mode character similar to that in Fig. 5.

The nonlinear development of the instability is an important issue. To address it completely, many modes would have to be kept in the simulation code, since nonlinear effects give rise to the generation of modes other than those involved in the linear growth stage. However, we believe that the simulation results with just the linear modes present may give a good guide to the nonlinear development of the instability for the following reasons. First, the quadrupole field gives an initial perturbation to the mode number m , so that the fields in this mode are not growing from random noise (see Fig. 4). Second, although wave-wave interactions are not treated correctly if we do not include other modes, the wave-particle interactions are treated nonlinearly. The simulations show that in those cases with large linear growth rates, which we can therefore afford to run to "saturation," the wave amplitude grows until the beam strikes the wall (see Fig. 4). As a result, most of the beam particles are lost, leaving a large-amplitude TE_{11} wave in the drift tube.

Finally, we look at what our analysis predicts for the stellatron experiment presently under way at the University of California at Irvine (UCI).^{15,16} The parameters for this experiment are tabulated in Table II. Because of the low current, the width of the instability is quite narrow, extending over at most one l number. As a result, small changes in parameters can cause the instability to abruptly appear and disappear (cf. Sec. III). We find that the beam is unstable in the region $\gamma = 2.4-2.45$. With a one-turn accelerating voltage¹⁵ of 500 V, the beam would spend sufficient time in this region to undergo 5-6 e foldings. This instability may be

TABLE II. Parameters of UCI stellatron.

Torus major radius	41 cm
Torus minor radius	4 cm
Beam current	200 A
Beam energy	20 kV-4 MeV
Toroidal magnetic field	0-10 kG
Vertical magnetic field	0-400 G
Quadrupole field (ϵ)	0.18
Quadrupole mode-number	12

related to the current disruption seen in some firings during the early part of the acceleration.¹⁶ We emphasize that this is a tentative explanation. It has also been suggested that the negative-mass instability may be responsible for this disruption.¹⁶

V. SUMMARY AND CONCLUSIONS

We have derived a dispersion relation for a parametric electromagnetic instability in a stellatron accelerator. The instability arises from the interaction between the quadrupole winding, a negative-energy transverse wave on the beam, and an electromagnetic waveguide mode. The growth rate of the instability is independent of the radius of the toroidal drift tube. It therefore occurs in straight, as well as toroidal, systems. Three-dimensional numerical simulations of the stellatron have been carried out with the code IVORY. The simulated linear growth rates and conditions for the onset of the instability are in reasonably good agreement with the analytic model. The simulations show strong disruption of the beam in the nonlinear regime, leading to loss of current. Our calculations predict some growth of the instability for the parameters of the UCI stellatron experiment. The instability may be a factor in limiting the beam current in this experiment.

ACKNOWLEDGMENTS

We thank Dr. D. Chernin for useful discussions. This work was funded by the Office of Naval Research.

- ¹P. Sprangle, C. A. Kapetanakis, and S. J. Marsh, *Proceedings of the IVth International Conference on High Power Electron and Ion Beams*, edited by H. J. Doucet and J. M. Buzzi (CNRS, Paris, 1981), p. 803.
- ²C. W. Roberson, *IEEE Trans. Nucl. Sci.* NS-28, 3433 (1981).
- ³C. W. Roberson, A. Mondelli, and D. Chernin, *Phys. Rev. Lett.* 50, 507 (1983).
- ⁴D. P. Taggart, M. R. Parker, H. J. Hopman, R. Jayakumar, and H. H. Fleischmann, *Phys. Rev. Lett.* 52, 1601 (1984).
- ⁵H. Ishizuka, G. Lindley, B. Mandelbaum, A. Fisher, and N. Rostoker, *Phys. Rev. Lett.* 53, 266 (1984).
- ⁶C. Agritellia, C. A. Kapetanakis, S. J. Marsh, A. Prakash, and P. Sprangle, *Bull. Am. Phys. Soc.* 29, 1430 (1984).
- ⁷D. W. Kerst, *Phys. Rev.* 58, 841 (1940).
- ⁸B. Mandelbaum, H. Ishizuka, A. Fisher, and N. Rostoker, *Bull. Am. Phys. Soc.* 29, 1431 (1984).
- ⁹W. M. Manheimer and E. Ott, *Phys. Fluids* 17, 463 (1974).
- ¹⁰B. Levush, T. M. Antonsen, W. M. Manheimer, and P. Sprangle, *Phys. Fluids* 28, 2273, (1985).
- ¹¹C-T. Tai, *Dyadic Green's Functions in Electromagnetic Theory* (Intext Educational, Scranton, PA, 1971). Later work has shown that the Green's function representation in this book is incomplete [e.g., W. A. Johnson, A. Q. Howard, and D. G. Dudley, *Radio Sci.* 14, 961 (1979)]. However, the missing terms do not contain electromagnetic resonances and so do not change our result.
- ¹²V. P. Silin, *Zh. Eksp. Teor. Fiz.* 48, 1679 (1965) [*Sov. Phys. JETP* 21, 1127 (1965)].
- ¹³M. M. Campbell and B. B. Godfrey (private communication).
- ¹⁴B. B. Godfrey and T. P. Hughes, *Phys. Fluids* 28, 669 (1985).
- ¹⁵H. Ishizuka, G. Leslie, B. Mandelbaum, A. Fisher, and N. Rostoker, *Bull. Am. Phys. Soc.* 30, 983 (1985).
- ¹⁶B. Mandelbaum, Ph.D. thesis dissertation, University of California at Irvine, 1985.

APPENDIX B

EQUILIBRIUM AND STABILITY PROPERTIES OF THE SOLENOIDAL LENS BETATRON

EQUILIBRIUM AND STABILITY PROPERTIES OF THE SOLENOIDAL LENS BETATRON

Thomas P. Hughes and Brendan B. Godfrey
Mission Research Corporation, 1720 Randolph Road, S.E.
Albuquerque, New Mexico 87106

Summary

The solenoidal lens betatron¹ uses a series of solenoidal lenses arranged around a race-track shaped drift-tube to provide strong transverse focusing for a high-current electron ring. Equilibrium behavior of the circulating beam is examined for parameters close to those of the University of New Mexico machine currently under construction. The tolerance of the beam to mismatches in the toroidal and vertical fields is evaluated analytically and using a particle simulation code. The linear and nonlinear development of the negative-mass instability in the device is also studied. Stability behavior comparable to that in a conventional betatron (i.e., one with no toroidal magnetic field) is found. Growth rates are compared to those obtained from an analytic model.

Equilibrium Properties

In order to confine and accelerate high currents in a betatron, the conventional weak focusing must be supplemented. In the solenoidal lens betatron (SLB)¹ this is accomplished through the use of periodic solenoidal lenses, as shown in Fig. 1. The SLB thus differs from the "modified" betatron,² for example, which uses a uniform toroidal field. For a matched equilibrium, the beam in the SLB reverses its poloidal rotation at each lens, so that the net poloidal rotation is zero. This requires that the beam be injected from a cathode which is shielded from magnetic flux, so that the beam produced has no canonical poloidal angular momentum. In the region between lenses, the beam rotates at the Larmor frequency, i.e., $\Omega_0/2\gamma$, where Ω_0 is the nonrelativistic cyclotron frequency in the solenoidal field, and γ is the relativistic factor. If the beam emittance is negligible, then force-balance requires

$$\frac{1}{2} - n_s + p^2/4 = 0 \quad (1)$$

where $n_s = 2vR^2/\gamma^3 a^2$, is the self-field index, v is Budker's parameter (beam current divided by 17 kA), R and a are major and minor beam radii, respectively, p is the beam velocity normalized to c , p is the ratio B_0/B_z , where B_z is the vertical betatron field, and B_0 is the solenoidal (toroidal) field between the lenses. We have assumed that the vertical field index is $1/2$. From Eq. (1), we can compute the solenoidal field needed for a matched beam, given the other quantities. Sample parameters for initial experiments at the University of New Mexico (UNM) are: $R = 1$ m, $a = 2$ cm, $\gamma = 3$, $v = 5.9 \times 10^{-3}$ (100 Amps). From these, we compute that $B_0 = 80$ Gauss is required. This result is expected to be accurate in the limit where the thickness of the magnetic cusps is much less than the distance between them. A scenario closer to that envisioned for the UNM device is to have 21 cm long solenoids spaced 10.5 cm apart. There are thus 20 solenoids evenly spaced around the 1 m major radius torus. We model the magnetic fields by using the exact, numerically computed values for finite length straight solenoids. One "cell" of the periodic field is shown

WORK supported by the Office of Naval Research.

in Fig. 2. Simulations of beam behavior in this device are carried out using the electromagnetic particle code IVORY.³ We find that to minimize the envelope fluctuations, the field in the middle of each solenoid must be about 100 Gauss. The discrepancy between this and the analytic result is presumably due to the thickness of the cusps, which lowers the average field value.

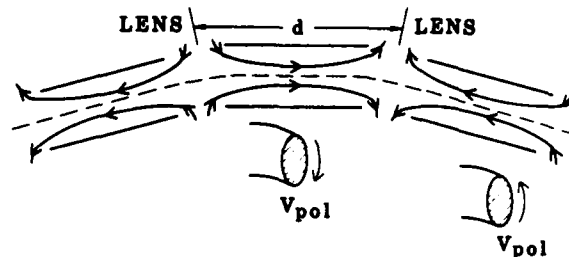


Figure 1. Section of Solenoidal Lens Betatron. The poloidal velocity V_{pol} reverses from one solenoid to the next.

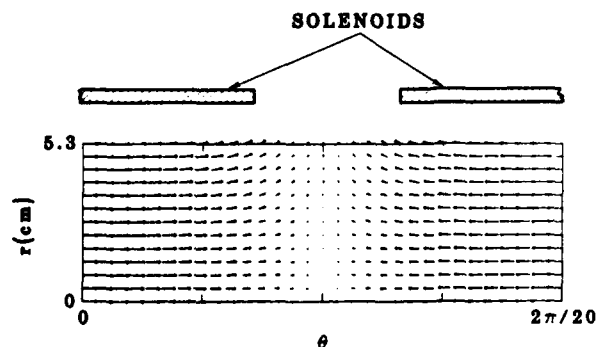


Figure 2. Vector plot of one-half period of toroidal field, showing location of solenoidal windings.

Mismatch in Solenoidal Field

To check the tolerance of the beam to mismatch in the solenoidal field, we run two cases in which the value of B_0 is doubled and halved respectively. In each case, we ensure that the beam has zero canonical poloidal angular momentum. The resulting envelope oscillation amplitudes are shown in Fig. 3. The beam oscillates between radii of 2 cm and 0.5 cm for $B_0 = 200$ Gauss, and between 2 cm and 3 cm for $B_0 = 50$ Gauss. Experimentally, it should not prove difficult to avoid these large mismatches.

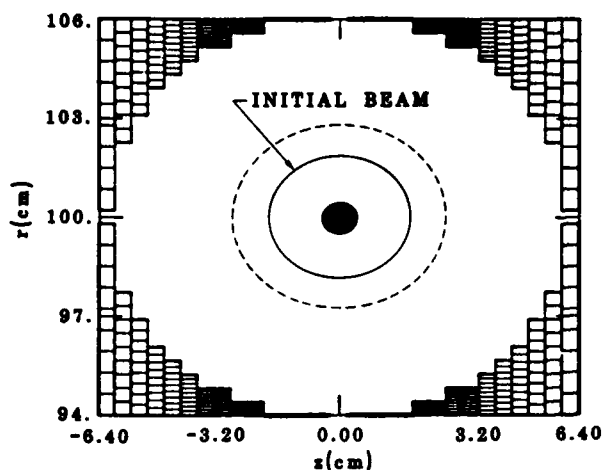


Figure 3. Amplitude of envelope oscillations for (i) $B_0 = 200$ Gauss (inner bullet), (ii) $B_0 = 50$ Gauss (dashed outer line).

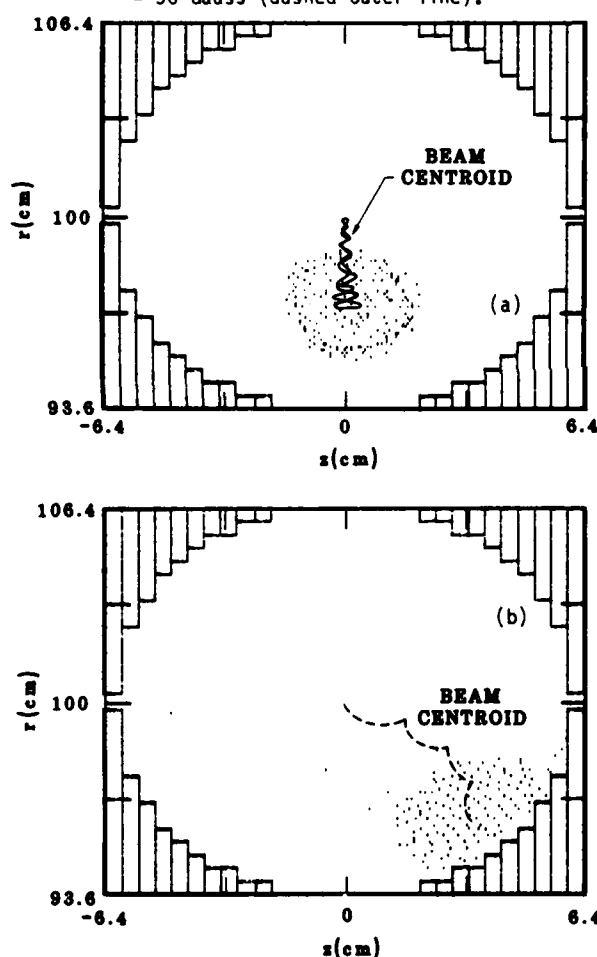


Figure 4. Effect of 1.5% vertical field mismatch in (a) SLB, (b) modified betatron.

Mismatch In Vertical Field

For a given value of the vertical field B_z , the matched major radius of the beam is $r = 8\gamma c/\Omega_z$, where r measures the distance from the major axis of the torus. Transverse oscillations about this radius are determined from the equation,

$$\Delta r + \Delta r \left(\frac{1}{2} - n_s \frac{a^2}{b^2} + p^2/4 \right) \Omega_z^2/\gamma^2 = \frac{\Delta B_z c^2}{B_z R} \quad (2)$$

where b is the minor radius of the drift-tube, and ΔB_z is the mismatch in the vertical field. This equation is valid in the thin-lens limit, in which the solenoidal lenses act as a continuous radial focusing force on the beam. Equation (2) predicts a momentum compaction factor $\alpha = (1/2 - n_s a^2/b^2 + p^2/4)^{-1}$. The effect of a 1.5% vertical field mismatch is shown in the particle simulation in Fig. 4, in which we assume the sample UNM beam parameters given above, and $B_0 = 100$ Gauss. For these parameters, $\alpha = 1$, so that the beam oscillates about an equilibrium major radius of 98.5 cm. For comparison, the momentum compaction factor of the weak-focusing modified betatron is $\alpha = (1/2 - n_s a^2/b^2)^{-1} = 2.5$. In this case a 1.5% mismatch in the vertical field gives the beam an average major radius of 96 cm. As seen in Fig. 4, the oscillation about this position brings the beam in contact with the wall. Even with the improved mismatch behavior of the SLB, however, keeping the vertical field matched to the beam energy to within a few percent will require delicate tuning of the experiment.

Stability Properties

A circulating high-current electron ring may be subject to several types of instabilities, including negative-mass, resistive wall, and, in the case of the SLB, which has accelerating gaps, the beam breakup instability. In addition, single particle orbital resonances may affect beam quality. Here, we concentrate on the negative-mass instability, since it is potentially the most serious collective instability.³ An analytic, high-current theory of this and some closely related instabilities is described in a companion paper.⁴ The theory is directly applicable only to devices in which the toroidal coordinate is ignorable in the equilibrium, such as the modified betatron. However, we use the theory here as a guide in discussing the stability of the SLB. Our numerical results obtained from 3-D simulations using IVORY are not restricted in this respect. However, the number of simulations we can perform, and their length, is small due to computing expenses. We have therefore concentrated on making runs at high currents, where relatively large growth rates are expected.

The first case we look at is a 10 kA, 5.5 MeV beam with $a = 2$ cm, and $R = 1$ m. We find that a solenoidal field of 600 Gauss can transport this beam with minimal (<10%) envelope modulation. The solenoidal lenses have the same configuration as in Fig. 2. The beam is given a small initial perturbation, and the growth of $\lambda = 20$ fields on the beam is followed. The justifications for following just one mode in the simulations are: a) In the linear regime, mode-coupling should be negligible; b) By following one mode, direct comparison with linear theory predictions for that particular mode are possible; c) Since there are 20 solenoids around the torus, the $\lambda = 20$ mode is likely to have a large initial perturbation; d) Computing costs severely limit the number of toroidal modes one can afford to keep. In the simulation just mentioned, we find a rapid linear growth rate of $\Gamma = 1.6 \times 10^8 \text{ sec}^{-1}$. The effect of the instability on the beam as it reaches nonlinear levels is shown in Fig. 5. The behavior is similar to the negative-mass behavior that one would expect to see in a

conventional betatron ($B_\theta = 0$).⁵ The radial deflection of the beam seen in Fig. 5(a) is accompanied by the toroidal bunching in Fig. 5(b). This behavior leads us to compare the linear growth rate with that obtained from theory⁴ for a $B_\theta = 0$ beam. We find that the theoretical growth rate is very close: $1.63 \times 10^8 \text{ sec}^{-1}$. In Fig. 6, we compare results for the SLB at other energies with the theory. For comparison, results for the same beam in a modified betatron with a 1 kG toroidal field are shown. In Fig. 7, the same curves are plotted for a 1 kA beam with $a = 1 \text{ cm}$. For these parameters, we have just one simulation result, at 5.5 MeV, and the growth rate is again seen to be close to the $B_\theta = 0$ result.

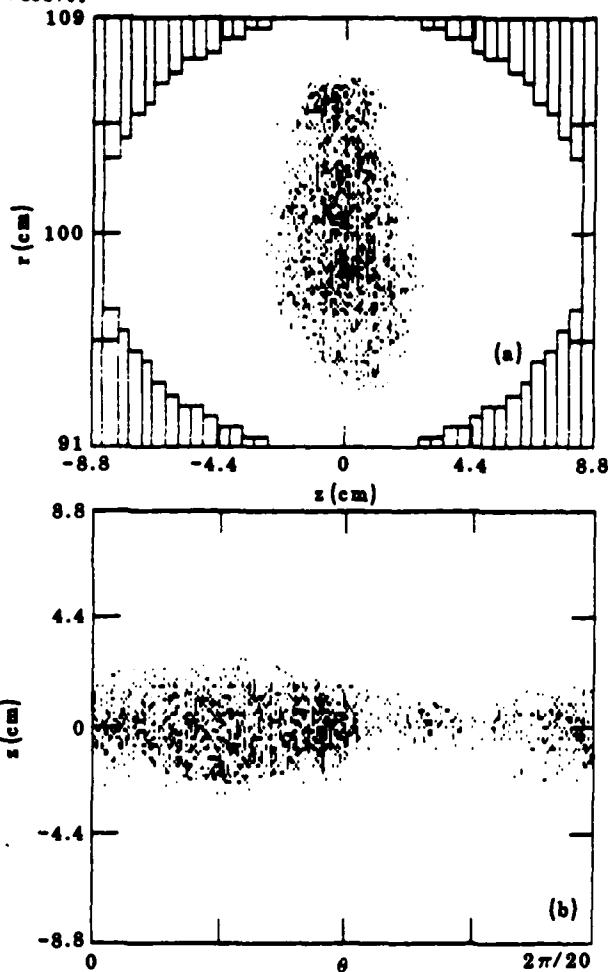


Figure 5. Effect of $l = 20$ negative-mass mode on 10 kA SLB beam. Particles at all θ -positions are plotted in (a).

We must note that the results in Fig. 6 for the case $B_\theta = 0$ are somewhat artificial when $\gamma < 18$. In this regime, weak focusing alone is insufficient to hold the beam together. The analytic model from which the growth rates are obtained uses a rigid disk model of the beam, and so ignores the force balance required within the beam. It is tempting to conclude from the results in Fig. 6 that in the SLB, the strong focusing provides the necessary forces to hold the beam equilibrium together, but that the negative-mass instabilities on the beam behave as if the toroidal field were zero. Further numerical and analytic work will be performed to check this conclusion.

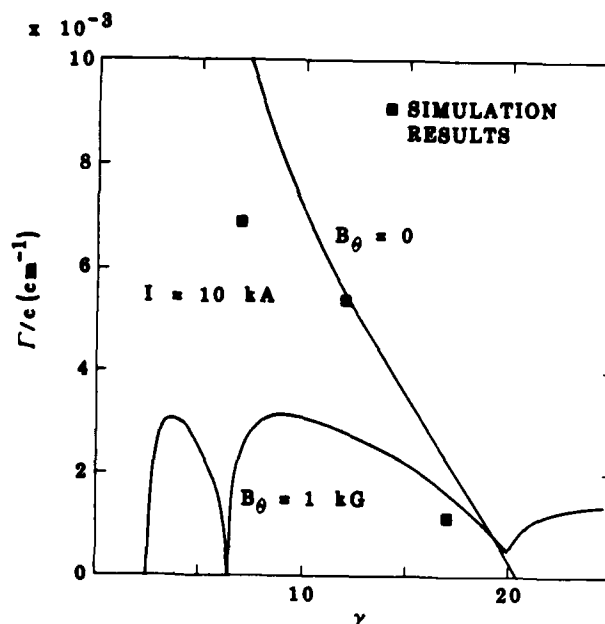


Figure 6. Growth rates of $l = 20$ mode versus energy. Simulation results for SLB, and analytic results for conventional ($B_\theta = 0$) and modified ($B_\theta = 1 \text{ kG}$) betatrons are shown.

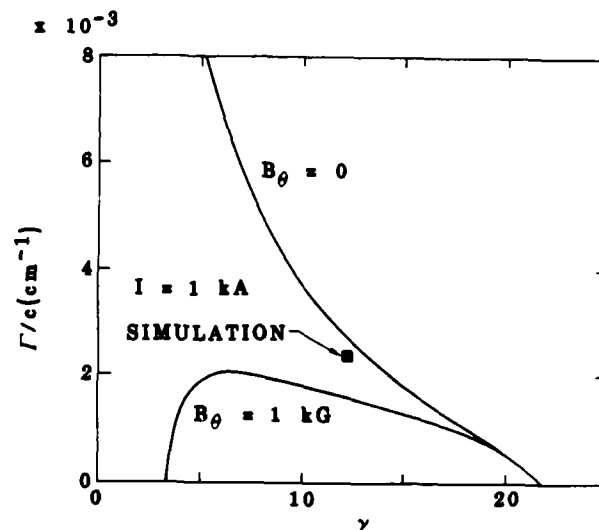


Figure 7. Growth rates of $l = 20$ instability for a 1 kA beam with 1 cm radius. Curves have same meaning as in Fig. 6.

References

1. S. Humphries, Jr. and D. M. Woodall, Bull. Am. Phys. Soc. **28**, 1054 (1983).
2. P. Sprangle, C. A. Kapetanakis, and S. J. Marsh, Proc. 4th Intl. Conf. on High Power Electron and Ion Beams (Palaiseau, France, 1981).
3. T. P. Hughes, M. M. Campbell, and B. B. Godfrey, AMRC-R-524 (Mission Research Corp., 1983); Phys. Fluids **28**, 669 (1985).
4. B. B. Godfrey and T. P. Hughes, this conference.
5. R. W. Landau and V. K. Neil, Phys. Fluids **9**, 2412 (1966).

APPENDIX C

STABILITY OF THE SOLENOIDAL LENS BETATRON

ABSTRACT

The solenoidal lens betatron uses solenoidal focusing to increase the current which can be injected into a betatron. A dispersion relation for the negative-mass instability in this device is derived using a multiple-length-scale method to average over the nonuniform toroidal field. The result qualitatively resembles the dispersion relation for the conventional betatron, but has a finite transition energy and suppressed growth rates. Both effects are due to the solenoidal focusing. It is shown that for a space-charge-dominated equilibrium, finite beam radius has a strong stabilizing influence even in the absence of any energy spread. Results of 3-D numerical simulations confirm the predicted stability at low toroidal mode-numbers. High toroidal mode-numbers show anomalously large growth rates, but saturate in a relatively benign manner.

ACKNOWLEDGMENT

This work was supported by the Office of Naval Research.

CONTENTS

<u>Section</u>		<u>Page</u>
1	INTRODUCTION	C-5
2	BEAM EQUILIBRIUM	C-8
3	NEGATIVE-MASS INSTABILITY	C-12
4	SOLUTIONS TO THE DISPERSION RELATION	C-20
5	STABILIZATION DUE TO FINITE BEAM RADIUS	C-23
6	COMPARISON WITH NUMERICAL SIMULATIONS	C-28
	6.1 IAPBT PARAMETERS	C-28
	6.2 HIGH-CURRENT BEAM STABILITY	C-31
7	SUMMARY AND DISCUSSION	C-34
	REFERENCES	C-36

ILLUSTRATIONS

<u>Figure</u>		<u>Page</u>
1	Conceptual picture of the solenoidal-lens betatron. In the actual device, 40 solenoids are placed around the racetrack	C-6
2	The coordinates used in the analytic derivation are cylindrical (r, θ, z) , and toroidal (ρ, ϕ, θ)	C-8
3	Growth rates of the negative-mass instability obtained from Eq. (31) for the parameters in Table 1	C-22
4	An equilibrium in which there is little transverse oscillation of the particles (as in a) has a much greater frequency spread than an equilibrium in which the radius is determined by the amplitude of betatron oscillations (as in b)	C-23
5	Branch cut in the complex $\omega - l\omega_0$ plane to make the dispersion relation, Eq. (31), analytic. The arrows show the movement of the roots as $G \rightarrow 1$ from above	C-26
6	Energy history of the $l = 15$ mode in a simulation of a 100 A, $\gamma_0 = 3$ beam, showing the linear growth and non-linear saturation	C-29
7	Particle plots $(r-\theta, z-\theta)$ taken during the nonlinear state of the $l = 15$ negative-mass instability on a 100 A, $\gamma_0 = 3$ beam. The dashed lines show the location of the toroidally uniform beam at the start of the simulation	C-30
8	Growth rates of the $l = 20$ negative-mass mode on a 10 kA beam in a solenoidal-lens betatron, plotted versus beam energy. Growth rates are compared to those for a conventional betatron (dashed line) and those obtained using the averaged-focusing approximation (solid line)	C-32
9	Particle plots $(r-z, r-\theta)$ taken during the nonlinear saturation of the $l = 20$ mode on a 10 kA beam. The beam energy is $\gamma_0 = 7$ in (a), and $\gamma_0 = 12$ in (b)	C-33

1. INTRODUCTION

Several types of betatron-like accelerators for high-current charged particle beams are being studied at present [1-5]. In order to overcome the space-charge limit on the current at low energies, these devices apply external magnetic fields in addition to those of the conventional betatron [6]. At the Institute for Accelerator and Plasma Beam Technology (IAPBT) of the University of New Mexico, a device is under construction in which the additional fields take the form of solenoidal lenses [5], as shown in Fig. 1. Forty solenoids of alternating polarity are arranged around a racetrack-shaped drift tube. Thus, in contrast to the "modified" betatron [1], which has a uniform toroidal magnetic field, the toroidal field in the IAPBT betatron alternates in direction from one solenoid to the next, with a magnetic cusp between each pair of solenoids. The advantages of this configuration have been discussed by Humphries et al. [5].

In this paper, we consider the negative-mass instability [7] in the presence of solenoidal lenses. This instability has been shown to be important for high-current electron beams in the modified betatron [8, 9], and stellatron [10], potentially causing serious disruption during the time it takes to accelerate the beam. Derivation of a negative-mass instability dispersion relation for the solenoidal lens betatron is complicated due to the lack of toroidal symmetry. To deal with this problem, we use a multiple-length-scale method to average over the varying solenoidal fields. This leads to a dispersion relation like that for the conventional betatron [7], with a modified transverse focusing term. The nature of the beam equilibrium in the solenoidal lens betatron results in a considerable spread in particle circulation frequencies at low beam energies. We evaluate the stabilizing effect this has on the negative mass instability. The analytic results are compared to three-dimensional particle-in-cell code simulations. These simulations do not make use of the multiple-length-scale approximation and so can be run at short wavelengths where this approximation breaks down.

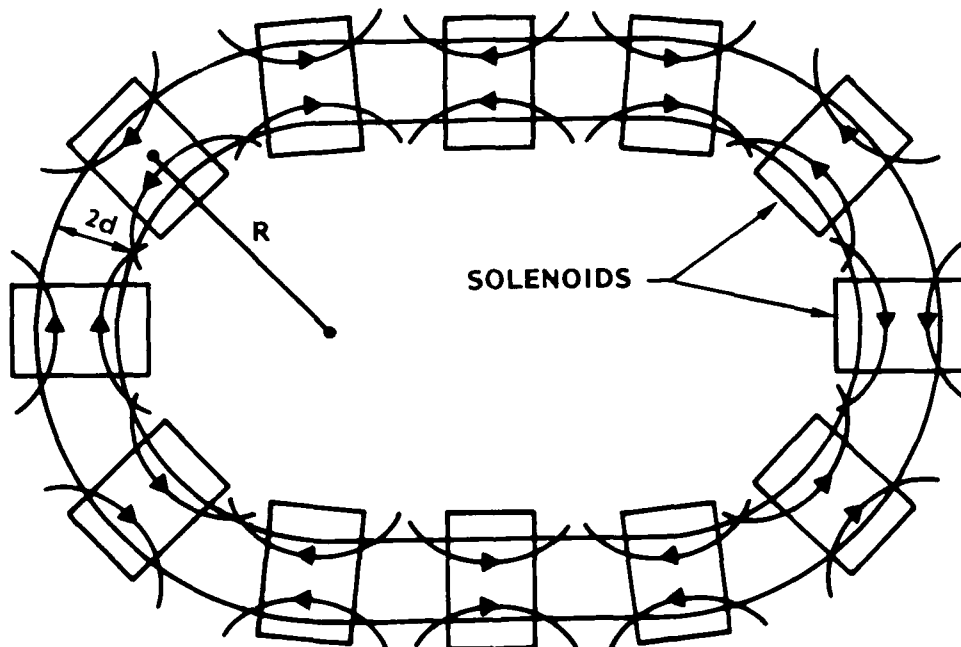


Figure 1. Conceptual picture of the solenoidal-lens betatron. In the actual device, 40 solenoids are placed around the racetrack.

This paper is organized as follows. In Sec. II, we obtain the equations for the equilibrium and small amplitude motion of the beam. In Sec. III, we derive a dispersion relation for the negative-mass instability including the effect the solenoidal lenses. In Sec. IV, we calculate the effect of circulation frequency spread. In Sec. V, we present some results of particle simulations of the negative-mass instability in a solenoidal lens betatron. Our conclusions are given in Sec. VI.

We shall use a system of normalized units which are convenient for electron beam physics problems. A plasma frequency ω_0 is defined such that $c/\omega_0 = 1$ cm, where c is the velocity of light. Then length is normalized to c/ω_0 , time to $1/\omega_0$, velocities to c , densities to $\omega_0^2 m / 4\pi e^2$, electric and magnetic fields to $m c \omega_0 / e$, where e , m are the electronic charge and mass respectively.

2. BEAM EQUILIBRIUM

For the purposes of this paper, we will assume that the accelerator drift-tube is a torus rather than a racetrack. (The IAPBT device has a modular design, and can be configured either as a racetrack or as a torus [5].) The coordinates we use are shown in Fig. 2. The reference orbit is that of a particle at $r = R$, $z = 0$. For this particle,

$$R = \gamma_0 V / B_{z0} \quad (1)$$

where B_{z0} is the value of the vertical field at $r = R$, and γ_0 is the matched particle energy and $V = (1 - 1/\gamma_0^2)^{1/2}$. If we displace the particle from this orbit, then its equations of motion are

$$\begin{aligned} -\frac{\gamma V_\theta^2}{r} + \frac{dp_r}{dt} &= E_r + V_\theta B_z - V_z B_\theta \\ \gamma \frac{V_\theta V_r}{r} + \frac{dp_\theta}{dt} &= E_\theta + V_z B_r - V_r B_z \\ \frac{dp_z}{dt} &= E_z + V_r B_\theta - V_\theta B_r \end{aligned} \quad (2)$$

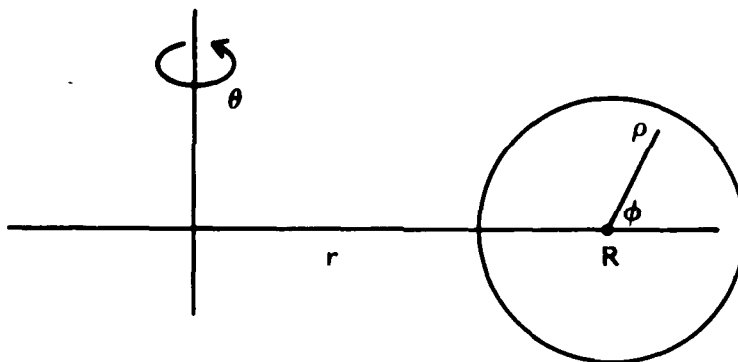


Figure 2. The coordinates used in the analytic derivation are cylindrical (r, θ, z) , and toroidal (ρ, ϕ, θ) .

where the components of the vectors \underline{v} , \underline{p} , \underline{E} , \underline{B} , represent velocity, momentum, electric and magnetic fields, respectively. We now proceed to linearize these equations about the reference orbit in the paraxial approximation [11]. For a particle at position $r = R + \delta r$, $z = \delta z$, the applied fields are [9]

$$\begin{aligned} B_z &= B_{z0}(1 - n\delta r/R) + B_{zs}(\theta) \\ B_r &= -B_{z0} n\delta z/R + B_{rs}(\theta) \\ B_\theta &= B_{\theta s}(\theta) \end{aligned} \tag{3}$$

where n is the external field index $n = -(R/B_{z0})dB_z/dr$ and subscript s denotes terms due to the solenoidal magnets. For the moment, we assume the beam is in a region of uniform toroidal field where B_{rs} , B_{zs} can be neglected. If we assume a Kapchinsky-Vladimirsky (KV) [11] beam equilibrium which has an elliptical cross-section (we will show that this is consistent later) then the self-fields at the particle can be calculated from the static Maxwell's equations:

$$\begin{aligned} E_r &= \frac{n_0 b}{a + b} \delta r \\ E_z &= \frac{n_0 a}{a + b} \delta z \\ B_z^s &= -\frac{n_0 V b \delta r}{a + b} \\ B_r^s &= \frac{n_0 V a \delta r}{a + b} \end{aligned} \tag{4}$$

where a , b are the radii in the r and z directions, respectively, n_0 is the beam density and superscript s denotes "self-field". Combining these equations with the linearizations of Eqs. (2), we obtain

$$\begin{aligned}\delta\ddot{r} + \left(1 - n - \frac{2n_s b}{a + b}\right) \omega_0^2 \delta r + \delta\dot{z} \frac{B_{\theta s}}{\gamma_0} &= 0 \\ \delta\ddot{z} + \left(n - \frac{2n_s a}{a + b}\right) \omega_0^2 \delta z - \delta\dot{r} \frac{B_{\theta s}}{\gamma_0} &= 0\end{aligned}\quad (5)$$

where the quantity $n_s \equiv 2\nu R^2 / \gamma_0^3 \beta_0^2 a b$ is referred to as the self-field index (ν is Budker's parameter). For a self-consistent KV equilibrium, the radii a, b are chosen such that

$$1 - n - \frac{2n_s b}{a + b} = n - \frac{2n_s a}{a + b} \quad (6)$$

To treat the effect of the magnetic cusps, it is convenient to change the coordinate system to the toroidal coordinates shown in Fig. 2 and introduce a vector potential $A_{\phi s}(\theta)$ which describes the solenoidal field. Equations (5) are replaced by

$$\rho - \rho\dot{\phi}^2 + \omega_\rho^2 \rho + \rho\dot{\phi} \frac{B_{\theta s}}{\gamma_0} = 0, \quad (7a)$$

$$\frac{1}{\rho} \frac{d}{dt} [\rho(\rho\dot{\phi} + A_{\phi s})] = 0, \quad (7b)$$

where

$$\omega_\rho^2 = \left(1 - n - \frac{2n_s b}{a + b}\right) \omega_0^2.$$

Equation (7b) can be integrated to obtain

$$L = \rho^2 \dot{\phi} + \frac{\rho A_{\phi s}}{\gamma_0} = \rho^2 \left(\dot{\phi} - \frac{1}{2} \frac{B_{\theta s}}{\gamma_0} \right) = \text{const.}, \quad (8)$$

Since L is a constant, its value is determined by the initial conditions. Experimentally, the beam will be generated using a cathode shielded from magnetic fields [5], so that $L = 0$. Substituting this into Eq. (7a), we obtain

$$\ddot{\rho} + \left(\frac{1}{4} \frac{B_{\theta s}^2}{\gamma_0^2} + \omega_p^2 \right) \rho = 0 \quad . \quad (9)$$

In the limit that the cusps become infinitely sharp, $B_{\theta s}^2$ is a constant over the particle orbit, and Eq. (9) has a stationary solution for

$$\frac{1}{4} \frac{B_{\theta s}^2}{\gamma_0^2} + \omega_p^2 = 0 \quad . \quad (10)$$

This is the condition for a space-charge dominated equilibrium, i.e., one where the emittance is negligible. To be consistent with the assumption of a fixed equilibrium profile, we require that the "phase-advance per solenoid", i.e., the poloidal angle through which the particles rotate on going through one solenoid, be small:

$$\mu_0 = \frac{1}{2} \frac{B_{\theta s}}{\gamma_0} \frac{S}{V} \ll 1 \quad (11)$$

where S is the length of a solenoid. The case $n = 1/2$ is a special one, since $a = b$, and poloidal rotation does not affect the beam profile. In this case, Eq. (11) can be relaxed. Struckmeier and Reiser [12] have shown that $\mu_0 < \pi/2$ is required for envelope stability.

Physically, the equilibrium we have just constructed behaves as follows. In a given solenoid, the beam particles rotate poloidally at the Larmor frequency, $B_{\theta s}/2\gamma_0$. On passing through the magnetic cusp into the next solenoid, the poloidal rotation changes direction. The shape of the beam is elliptical, in general, with radii determined from Eq. (6), and has a uniform density determined from Eq. (10). If the magnetic cusps are not infinitely sharp, then an equilibrium can still be constructed [12], but the radii a, b vary periodically with toroidal angle.

3. NEGATIVE-MASS INSTABILITY

In order to analyse the negative-mass instability, we adopt a simplified model of the beam dynamics. We assume that the beam acts like a rigid body in the transverse direction, so that only the transverse motion of the beam centroid has to be calculated, rather than the transverse motion of each beam particle. Comparisons between a rigid-beam model and three-dimensional particle simulations for the case of the modified betatron [8] have produced good agreement. The physical basis for the model rests on the fact that when the beam minor radius is much smaller than the drift tube minor radius, the perturbed toroidal forces are the same for all particles in a given transverse slice of the beam, and the perturbed transverse forces are linearly proportional to the transverse displacement of each particle in the slice. In the toroidal direction, the model places no restriction on the beam motion. The transverse motion of the beam generates perturbed dipole fields, while toroidal bunching generates perturbed monopole fields.

To obtain the equations for the beam centroid, we start from Eqs. (2). The field quantities which we insert into these equations are evaluated at the center of the beam. It has been shown [8] that for high-current beams, toroidal corrections to the continuity equation and the field equations (i.e., terms of order d/R and higher where d is the wall radius) must be retained in the calculation, particularly for high toroidal mode numbers. A model which uses an exact, though cumbersome, solution to these equations has been derived [13]. The exact model shows that the cylindrical approximation for the field equations gives reasonably good results for low toroidal mode-numbers if a certain replacement is made [Eq. (30)]. Here, we will make use of this simplification in order to avoid the complexities of toroidal corrections.

For low toroidal mode-numbers, the long-wavelength, low-frequency approximation $\omega^2, k^2/R^2 \ll \nabla_{\perp}^2$ (ω, k denote the mode frequency and

wave-number, respectively, and ∇_{\perp}^2 denote the transverse Laplacian) can be used in solving the field equations. Neglecting toroidal corrections and assuming a circular beam cross-section, the solutions for the perturbed transverse self-fields at the perturbed beam centroid position are

$$\begin{aligned}\Delta E_r &= \frac{n_0}{2} \frac{a^2}{d^2} \Delta r \\ \Delta E_z &= \frac{n_0}{2} \frac{a^2}{d^2} \Delta z \\ \Delta B_r^s &= \frac{n_0 V}{2} \frac{a^2}{d^2} \Delta r \\ \Delta B_z^s &= - \frac{n_0 V}{2} \frac{a^2}{d^2} \Delta z\end{aligned}\tag{12}$$

where Δ denotes perturbed quantities, and Δr , Δz denote the transverse displacement amplitudes of the beam centroid. These fields come from the dipole components of $\Delta \underline{E}_{\perp}$ and $\Delta \underline{B}_{\perp}^s$. The monopole components of the transverse fields do not couple to the centroid motion. The monopole component of ΔE_{θ} does enter, however, and can be obtained using the integral form of Faraday's Law,

$$\begin{aligned}\oint \underline{E} \cdot d\underline{l} &= - \frac{\partial}{\partial t} \int \underline{B} \cdot d\underline{S} \\ \rightarrow \Delta E_{\theta}^0 &= - \frac{1}{R} \frac{\partial}{\partial \theta} \int_0^d \Delta E_{\rho}^0 d\rho - \frac{\partial}{\partial t} \int_0^d \Delta B_{\phi}^0 d\rho\end{aligned}\tag{13}$$

where the superscript zero denotes the monopole component. The sources for ΔE_{ρ}^0 , ΔB_{ϕ}^0 are the monopole components of Δn and Δj_{θ} , respectively. The latter are related to the perturbed beam displacement through the continuity equation [8]:

$$\Delta n = - \frac{\partial}{\partial z} n_0 \Delta z - \frac{1}{r} \frac{\partial}{\partial r} r n_0 \Delta r - \frac{\partial}{\partial \theta} n_0 \Delta \theta \quad (14)$$

From this and $\Delta J_\theta = n_0 R \dot{\Delta \theta} + \Delta n V$ where the dot denotes the total time derivative, we obtain the expressions

$$\begin{aligned} \Delta n^0 &= - \frac{\partial}{\partial \theta} n_0 \Delta \theta \\ \Delta J_z^0 &= \frac{\partial}{\partial t} n_0 \Delta \theta \end{aligned} \quad (15)$$

Consistent with our use of the cylindrical approximation, we have neglected toroidal terms in Eq. (15). Substitution into Eq. (14) yields

$$\Delta E_\theta^0 = \frac{1}{4} n_0 a^2 \left(1 + 2 \ln \frac{d}{a} \right) \left(\frac{1}{R^2} \frac{\partial^2}{\partial \theta^2} - \frac{\partial^2}{\partial t^2} \right) \Delta \theta \quad (16)$$

The applied fields are given by Eq. [3], with δr , δz replaced by Δr , Δz . We can now write down the linearized equations of motion for the beam centroid:

$$\begin{aligned} \Delta \ddot{r} + \omega_\perp^2 \Delta r + \Delta \dot{z} \frac{B_{\theta s}}{\gamma_0} - \frac{\Delta V_\theta B_{zs}}{\gamma_0} &= \gamma_0^2 \omega_0 \Delta V_\theta \\ \Delta \ddot{z} + \omega_\perp^2 \Delta z - \Delta \dot{r} \frac{B_{\theta s}}{\gamma_0} + \frac{\Delta V_\theta B_{rs}}{\gamma_0} &= 0 \\ \Delta \dot{V}_\theta &= \frac{\Delta E_\theta}{\gamma_0} \end{aligned} \quad (17)$$

where

$$\omega_\perp^2 = \left(\frac{1}{2} - n_s \frac{a^2}{d^2} \right) \omega_0^2,$$

and we have taken $n = 1/2$ to be consistent with $a = b$ [Eq. (6)]. To solve Eq. (17), we perform a multiple-length-scale analysis to average over the solenoidal lenses. This involves an ordering scheme where the wavelength of the beam mode λ is assumed to be much longer than the period of the

alternating solenoidal fields, i.e., $S/\lambda = O(\epsilon)$, where ϵ is a smallness parameter. Consistent with this, we assume $\partial/\partial t$, ω_0 , ω_\perp are of order ϵ . In addition, we assume, as in the equilibrium equations, that $\mu_0 \ll 1$ [Eq. (11)]. It is convenient to perform the averaging in toroidal coordinates (Fig. 2), in which Eqs. (17) have the form

$$\ddot{\rho} - \rho \dot{\phi}^2 + \omega_\perp^2 \rho + \rho \dot{\phi} \frac{B_{\theta s}}{\gamma_0} = \gamma_0^2 \omega_0 \Delta V_\theta \cos \phi \quad (18a)$$

$$\frac{1}{\rho} \frac{d}{dt} \left[\rho^2 \left(\dot{\phi} - \frac{1}{2} \frac{B_{\theta s}}{\gamma_0} \right) \right] = -\gamma_0^2 \omega_0 \Delta V_\theta \sin \phi \quad (18b)$$

$$\ddot{\zeta} + \omega_0 \Delta \dot{\zeta} - C \left(\frac{\partial^2}{\partial s^2} - \frac{\partial^2}{\partial t^2} \right) \zeta = 0 \quad (18c)$$

where $\zeta = R\Delta\theta$, $s = R\theta$, and $C = 1/4(n_0 a^2)(1 + 2\ln d/a)/\gamma_0^3$. All quantities are expanded in powers of ϵ in the following manner,

$$\rho(s, t) = \rho_0(s_0, s_1, t) + \epsilon \rho_1(s_0, s_1, t) + \dots \quad (19a)$$

$$\phi(s, t) = \phi_0(s_0, s_1, t) + \epsilon \phi_1(s_0, s_1, t) + \dots \quad (19b)$$

$$\zeta(s, t) = \zeta_0(s_0, s_1, t) + \epsilon \zeta_1(s_0, s_1, t) + \dots \quad (19c)$$

where s_0 , s_1 denote the short and long length-scales, respectively. The essence of the multiple-scale method is that s_0 and s_1 are treated as independent variables. The total time derivative d/dt is expanded as $V(\partial/\partial s_0) + \epsilon(d/dt_1)$ where $d/dt_1 = \partial/\partial t + V\partial/\partial s_1$. To zero order in ϵ , Eqs. (18) become

$$V^2 \frac{\partial^2}{\partial s_0^2} \rho_0 - \rho_0 \left(V \frac{\partial \phi_0}{\partial s_0} \right)^2 = 0$$

$$V \frac{\partial}{\partial s_0} \left[\rho_0^2 V \frac{\partial \phi_0}{\partial s_0} \right] = 0$$

$$V^2 \frac{\partial^2}{\partial s_0^2} \zeta_0 - C \frac{\partial^2}{\partial s_0^2} \zeta_0 = 0 \quad (20)$$

From these, we conclude that ρ_0 , ϕ_0 , ζ_0 do not depend on s_0 . Using this information, we obtain to order ϵ ,

$$V^2 \frac{\partial^2 \rho_1}{\partial s_0^2} = 0$$

$$\frac{\partial}{\partial s_0} \left[\rho_0^2 \left(V \frac{\partial \phi_1}{\partial s_0} + \frac{\partial \phi_0}{\partial t} \right) - \frac{1}{2} \frac{B_{\theta s}}{\gamma_0} \right] = 0$$

$$(V^2 - C) \frac{\partial^2}{\partial s_0^2} \zeta_1 = 0 \quad (21)$$

These equations imply that ρ_1 , ζ_1 also do not depend on s_0 . For ϕ_1 , we obtain

$$\phi_1 = \left(\frac{F(t, s_1)}{\rho_0^2} - \frac{\partial \phi_0}{\partial t} \right) s_0 + \frac{1}{2} \int \frac{B_{\theta s}}{\gamma_0} ds_0 + G(t, s_1) \quad (22)$$

where $F(t, s_1)$, $G(t, s_1)$ are arbitrary constants. The secular dependence on s_0 can be removed by choosing

$$F = \rho_0^2 \frac{\partial \phi_0}{\partial t} \quad (23)$$

This choice implies that $\partial \phi_1 / \partial s_0$ depends only on s_0 . Proceeding to order ϵ^2 , we obtain

$$\begin{aligned}
v^2 \frac{\partial^2 \rho_2}{\partial s_0^2} + \frac{\partial^2 \rho_0}{\partial t^2} - \rho_0 \left(\frac{\partial \phi_0}{\partial t} + v \frac{\partial \phi_1}{\partial s_0} \right)^2 + \omega_0^2 \rho_0 + \rho_0 \left(\frac{\partial \phi_0}{\partial t} + v \frac{\partial \phi_1}{\partial s_0} \right) \frac{B_{\theta s}}{\gamma_0} = \\
= \gamma_0^2 \omega_0 \left[\omega_0 \rho_0 \cos \phi_0 + \frac{\partial \zeta_0}{\partial t} \right] \cos \phi_0
\end{aligned} \quad (24a)$$

$$v^2 \frac{\partial^2 \phi_2}{\partial s_0^2} + \frac{\partial}{\partial t} \left(\rho_0^2 \frac{\partial \phi_0}{\partial t} \right) = -\gamma^2 \omega_0 \left[\frac{\partial \zeta_0}{\partial t} + \omega_0 \rho_0 \cos \phi_0 \right] \sin \phi_0 \quad (24b)$$

$$\begin{aligned}
v^2 \frac{\partial^2}{\partial s_0^2} \zeta_2 + \frac{\partial^2 \zeta_0}{\partial t^2} + \omega_0 \left(\frac{\partial}{\partial t} \rho_0 \cos \phi_0 - v \rho_0 \sin \phi_0 \frac{\partial \phi_1}{\partial s_0} \right) \\
- c \left[\frac{\partial^2 \zeta_2}{\partial s_0^2} + \left(\frac{\partial^2}{\partial s_1^2} - \frac{\partial^2}{\partial t^2} \right) \zeta_0 \right] = 0
\end{aligned} \quad (24c)$$

We now average these equations over one period of the magnetic lenses. Subtracting the averaged equations for Eqs. (24b) and (24c) from the unaveraged ones, we obtain

$$\frac{\partial^2 \phi_2}{\partial s_0^2} = \left\langle \frac{\partial^2 \phi_2}{\partial s_0^2} \right\rangle \quad (25a)$$

$$\frac{\partial^2 \zeta_2}{\partial s_0^2} = \left\langle \frac{\partial^2 \zeta_2}{\partial s_0^2} \right\rangle \quad (25b)$$

where the brackets $\langle \rangle$ denote the average. Solving these equations, and removing secularities in the usual way, we find $\partial^2 \phi_2 / \partial s_0^2 = \partial^2 \zeta_2 / \partial s_0^2 = 0$. From Eq. (24b), we note that if we impose the initial conditions $\phi_0 = 0$, $\partial \phi_0 / \partial t = 0$ at $t = 0$, then this equation has the unique solution $\phi_0(t) = 0$. By imposing these initial conditions, and thereby restricting the class of initial conditions for which the analysis is valid, we can set $\phi_0 = 0$ in Eqs. (24). From Eqs. (22) and (24a), we then obtain

$$v^2 \frac{\partial^2 \rho_2}{\partial s_0^2} + \frac{\partial^2 \rho_0}{\partial t^2} + \frac{1}{4} \left(\frac{B_{\theta s}}{\gamma_0} \right)^2 \rho_0 + \omega_{\perp}^2 \rho_0 = \gamma_0^2 \omega_0 \left(\omega_0 \rho_0 + \frac{\partial \zeta_0}{\partial t} \right) \quad (26)$$

By subtracting this equation from its average, it is again straightforward to show that $\langle \partial^2 \rho_2 / \partial s_0^2 \rangle = 0$ (but $\partial^2 \rho_2 / \partial s_0^2 \neq 0$). We thereby obtain the equations for the averaged beam centroid motion:

$$\frac{\partial^2 \rho_0}{\partial t^2} + \left(\omega_{\perp}^2 + \frac{1}{4} \left\langle \frac{B_{\theta s}^2}{\gamma_0^2} \right\rangle \right) \rho_0 = \gamma_0^2 \omega_0 \left(\omega_0 \rho_0 + \frac{\partial \zeta_0}{\partial t} \right) \quad (27a)$$

$$\frac{\partial^2 \zeta_0}{\partial t^2} + \omega_0 \frac{\partial \rho_0}{\partial t} - c \left(\frac{\partial^2}{\partial s_1^2} - \frac{\partial^2}{\partial t^2} \right) \zeta_0 = 0 \quad (27b)$$

$$\phi_0 = 0 \quad (27c)$$

Note that Eqs. (27a) and (27b) have the form of the equations one would obtain if no solenoidal magnetic lenses were present. Thus, to the order we have solved the original equations, the net effect of the solenoidal lenses is to increase the transverse focusing on the beam by an amount proportional to $\langle B_{\theta s}^2 / \gamma_0^2 \rangle$, i.e.,

$$\omega_{\perp}^2 \rightarrow \omega_{\perp}^2 + \frac{1}{4} \left\langle \frac{B_{\theta s}^2}{\gamma_0^2} \right\rangle \equiv \Omega_{\perp}^2 \quad (28)$$

To obtain a dispersion relation from Eqs. (27), we assume that the perturbed quantities vary as $\exp(i\ell\theta - i\omega t)$. In Eq. (27b), we obtain the factor $\ell^2/R^2 - \omega^2$. However, as shown in Ref. [13], when toroidal corrections to the field equations and the continuity equation are kept, we instead obtain the factor $\alpha_1 \ell^2/R^2 - \alpha_2 \omega^2$, where α_1 and α_2 are frequency- and mode-number-dependent expressions approximately equal to unity. In general, we can approximate $\omega = \ell\omega_0$ in evaluating this factor,

$$\alpha_1 \frac{\ell^2}{R^2} - \alpha_2 \omega^2 \approx \frac{\ell^2}{R^2} (\alpha_1 - \alpha_2 V^2) \quad (29)$$

Small differences between α_1 and α_2 can strongly affect the magnitude and even the sign of $\alpha_1 - \alpha_2 V^2$. These effects become increasingly evident as the mode number ℓ increases. However, the averaging procedure we have used is only valid for low mode numbers, and for our purposes, it will be sufficient to set $\alpha_1 = \alpha_2 = 1$ in Eq. (29)

$$\alpha_1 \frac{\ell^2}{R^2} - \alpha_2 \omega^2 \approx \frac{1}{\gamma_0^2} \frac{\ell^2}{R^2} \quad (30)$$

This approximation was made on heuristic grounds by Landau and Neil [7]. The main error introduced is in the asymptotic fall-off of growth rate with γ_0 [13]. The important point here is that much larger errors are introduced by keeping the unmodified factor $\ell^2/R^2 - \omega^2$ in the dispersion relation. Fictitious cutoffs in the growth rate as a function of energy and current are predicted [14].

Using Eq. (28), the dispersion relation obtained is:

$$1 = \frac{\ell^2 C}{R^2 \Omega^2} \left(\frac{1}{\gamma_0^2} + \frac{\omega_0^2}{\Omega^2 - \Omega_I^2} \right) \quad (31)$$

where $\Omega = \omega - \ell \omega_0$.

4. SOLUTIONS TO THE DISPERSION RELATION

By inspection of Eq. (31), we see that there are resonances at $\Omega^2 = 0$ and $\Omega^2 = \Omega_{\perp}^2$, corresponding to the longitudinal and transverse modes of oscillation of the beam. These modes are coupled through the negative-mass effect. For the low ℓ -numbers we are considering, the coupling is non-resonant, i.e., the resonances do not overlap. Thus, for the mode near $\Omega = 0$, we can set $\Omega^2 \ll \Omega_{\perp}^2$, to get

$$\Omega^2 = \frac{\ell^2 C}{R^2} \left(\frac{1}{\gamma_0^2} - \frac{\omega_0^2}{\Omega_{\perp}^2} \right) \equiv -r_0^2 \quad (32)$$

When the right-hand side is negative, we obtain the negative-mass instability. For $B_{\theta s} = 0$, Eq. (32) becomes the expression of Landau and Neil [7] for a monoenergetic beam in a conventional betatron. The condition for instability is

$$\gamma_0 > \left(\frac{1}{2} + \frac{1}{4} \frac{\langle B_{\theta s}^2 / \gamma_0^2 \rangle}{\omega_0^2} \right)^{1/2} \equiv \gamma_{tr} \quad (33)$$

Thus, the strong-focusing effect of the solenoids introduces a finite negative-mass transition energy γ_{tr} below which the beam is stable. This contrasts with the conventional betatron which is unstable at all energies. Further, we note from Eq. (32) that when $\langle B_{\theta s}^2 / \gamma_0^2 \rangle > 1/2$, the growth rate scales as $1/|B_{\theta s}|$, so that the solenoidal focusing strongly suppresses growth of the instability.

As the beam is accelerated, γ_0 increases. We see from Eq. (28) that the effect of the solenoidal focusing rapidly decreases unless $B_{\theta s}$ is increased also. By ramping $B_{\theta s}$ in synchronism with γ_0 , the suppression of growth rates relative to the conventional betatron is maintained. An additional benefit is that the crossing of single-particle resonances is avoided. The obvious drawback is that additional energy is required to drive the solenoids.

In Fig. 3, we show growth rates obtained from Eq. (29) for parameters typical of the IAPBT betatron (Table 1). The curves show the contrast between a case where the solenoidal field is kept fixed at its injection value, and one where it is ramped linearly with γ_0 . Note that the growth rates in both cases are substantial for a device an acceleration time of several tens of microseconds.

TABLE 1. SOLENOIDAL LENS BETATRON PARAMETERS

Torus Major Radius	1 m
Torus Minor Radius	4.5 cm
Beam Major Radius	1 m
Beam Minor Radius (at injection)	-2 cm
Injected Beam Energy	300 kV
Injected Beam Current	-100 A
Solenoidal Field Amplitude (at injection)	-220 Gauss
Number of Solenoids	30

There is a qualitative difference between Eq. (31) and the the corresponding dispersion relation for the modified betatron [1, 9], which has a uniform toroidal field. In Eq. (31) only the radial and toroidal modes of the beam are coupled (cf. Fig. 7). In the modified betatron, the radial beam motion is coupled to the vertical motion (z-direction in Fig. 2) as well as to the toroidal motion.

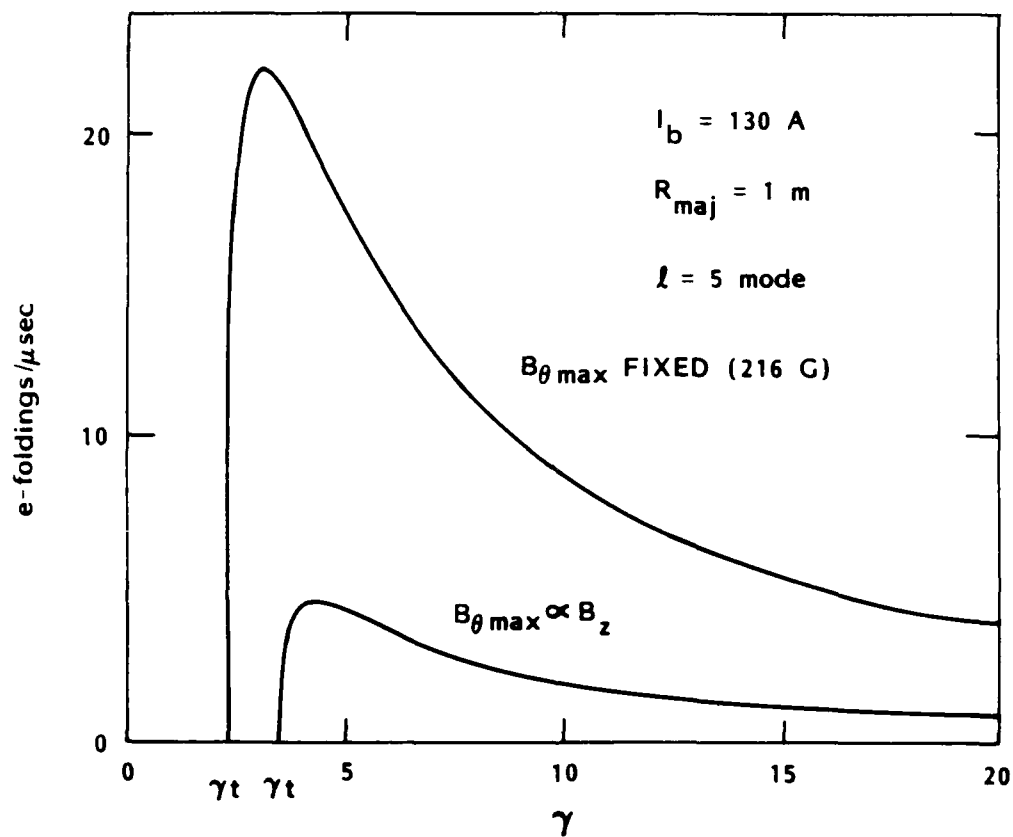


Figure 3. Growth rates of the negative-mass instability obtained from Eq. (31) for the parameters in Table 1.

5. STABILIZATION DUE TO FINITE BEAM RADIUS

In the derivation of Eq. (31), we assumed that all particles rotate about the major axis of the torus at the same frequency, namely, $\omega_0 = V/R$. For a finite radius beam, however, there is a spread in path lengths around the torus. Thus, even if $V = c$ for all particles, there is a spread in rotation frequencies. Taking a uniform density equilibrium of the type discussed in Sec. II, with circular cross-section and small phase advance per solenoid (Eq. 11), it is straightforward to show that the distribution function for the particle rotation frequencies is

$$f(\dot{\theta}) = A [a^2 \omega_0^2 / R^2 - (\dot{\theta} - \omega_0)^2]^{1/2} \quad (34)$$

where A is a normalization constant and $\dot{\theta}$ is the particle rotation frequency. The width of the distribution function is $a\omega_0/R$. This contrasts with the conventional and modified betatrons, where the betatron oscillations of the particles result in a width which is only of order $(a/R)^2$ for a monoenergetic beam (see Fig. 4). For these devices, it is generally

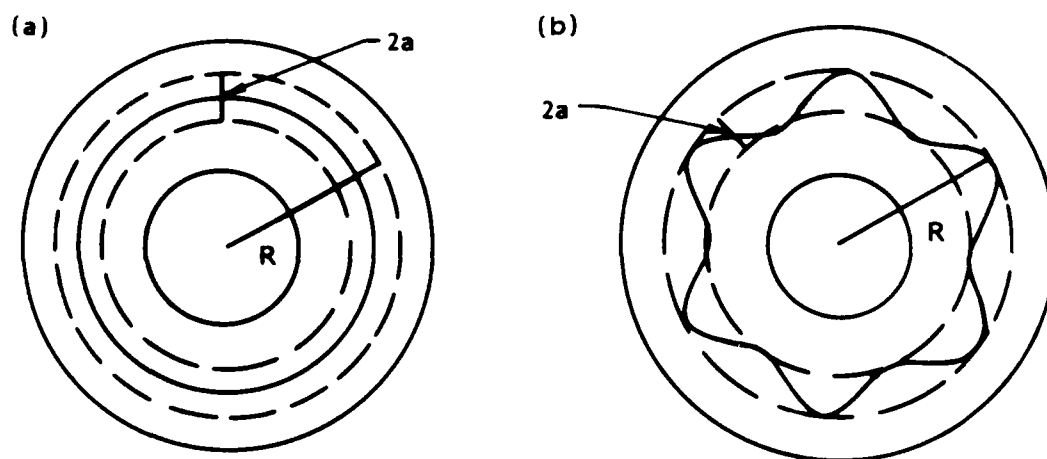


Figure 4. An equilibrium in which there is little transverse oscillation of the particles (as in a) has a much greater frequency spread than an equilibrium in which the radius is determined by the amplitude of betatron oscillations (as in b).

necessary to have an energy spread on the beam to obtain a significant frequency spread [7, 9].

In order to derive a dispersion relation taking frequency spread into account, a kinetic treatment is necessary. Rather than redoing the analysis of Sec. III in the framework of the Vlasov equation, we will make a plausibility argument for adapting the kinetic dispersion relation for the conventional betatron derived by Landau and Neil [7]. As observed in Sec. IV, Eq. (31) can be obtained from the cold beam result of Ref. [7] when the replacement in Eq. (28) is made. The longitudinal motion of the particles is affected by the solenoidal field only to order $(\mu_0 a/S)^2 \ll 1$. Therefore, we expect the influence of the solenoids on the resonance at $\Omega^2 = 0$, which is associated with the instability, to be minimal. In addition, as noted at the beginning of Sec. 4, there is no resonant coupling to the transverse beam modes for low ℓ -numbers. On this basis, we modify the kinetic equation of Ref. [7] according to Eq. (28), we obtain the dispersion relation:

$$1 = - \left[\frac{1}{4} \frac{a^2}{\gamma_0^2} \left(1 + 2\ell n \frac{d}{a} \right) \right] \int \frac{\partial f}{\partial p} \frac{dp}{\Omega + \ell k \tilde{p}} \quad (35)$$

where

$$k = \frac{1}{\gamma_0 R^2} \left(\frac{\omega_0^2}{\Omega_{\perp}^2} - \frac{1}{\gamma_0^2} \right)$$

$p = \gamma \omega_0 R^2 + \tilde{p}$ is the canonical angular momentum, and f is normalized such that $\int f dp = n_0$. The relation between \tilde{p} and $\hat{\theta}$ is $\hat{\theta} = \omega_0 - k \tilde{p}$. Converting Eq. (35) into an integral over $\hat{\theta}$, and inserting the distribution function in Eq. (34), we obtain the dispersion relation

$$1 = G \left[1 + \frac{\Omega}{(\Omega^2 - (\ell a \omega_0 / R)^2)^{1/2}} \right] \quad (36)$$

where

$$G = \frac{2C}{R^2} \left(\frac{\omega_0^2}{\Omega_1^2} - \frac{1}{\gamma_0^2} \right) \left(\frac{R^2}{a^2 \omega_0^2} \right)$$

Equation (36) can be made analytic in the complex ω plane by introducing the branch cut shown in Fig. 5. We find that for $1 < G < \infty$, the beam is unstable with growth rate

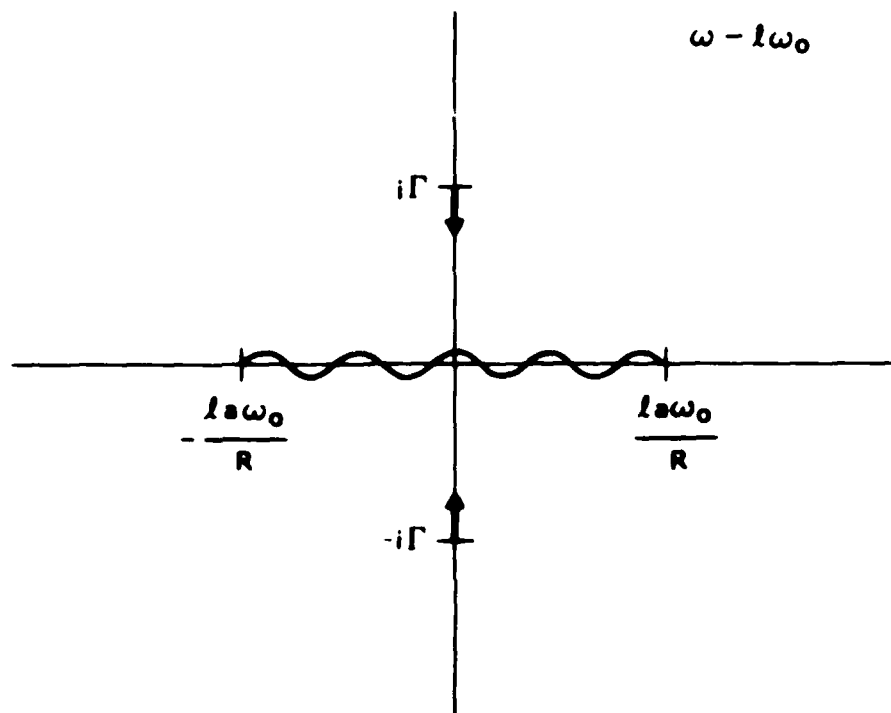
$$\Gamma = \frac{\ell \omega_0 a}{R} \frac{G - 1}{\sqrt{2G - 1}} \quad (37)$$

The zero-frequency-spread growth rate Γ_0 in Eq. (32) can be recovered by letting $a \rightarrow 0$. As G approaches 1 from above, the roots approach the branch cut, as shown in Fig. 5. For $G < 1$, the negative-mass mode disappears, and the beam is stable. The stability criterion can be rewritten

$$\Gamma_0 < \frac{\ell \omega_0 a}{R} \quad (38)$$

This criterion has a physical interpretation in terms of the rotation frequency spread of the particles. Consider two particles, one at $r = R$, and one at $r = R \pm a$, which are initially at the same toroidal angle. Then at marginal stability, these particles will become separated by $1/\ell$ radians in a time $1/\Gamma_0$. This smearing effect prevents clumping of the beam.

We emphasize that the stability criterion just derived is only valid for a cold, space-charge dominated equilibrium of the type described in Sec. II. To apply Eq. (38) to a hot beam, one must calculate an effective radius which excludes the contribution of transverse betatron oscillations to the radius. In the extreme case where the finite beam radius is completely due to betatron oscillations, as in Fig. 4b, the frequency spread is negligible for typical parameters.



R-922

Figure 5. Branch cut in the complex $\omega - l\omega_0$ plane to make the dispersion relation, Eq. (31), analytic. The arrows show the movement of the roots as $G \rightarrow 1$ from above.

Applying Eq. (38) to the cases in Fig. 3, we find that a beam radius of 1.2 cm is sufficient to stabilize the peak growth rate. As the beam is accelerated, its radius shrinks, thereby decreasing the width of the frequency distribution. From Eq. (10) we find

$$a^2 = \frac{8vR^2}{\gamma_0^3 v^2} \left(2 + \frac{\langle B_{\theta s}^2 / \gamma_0^2 \rangle}{\omega_0^2} \right)^{-1} \quad (39)$$

so that the radius shrinks as $\gamma_0^{-3/2}$ if $\langle B_{\theta s}^2 / \gamma_0^2 \rangle$ is held fixed. If $B_{\theta s}$ is held fixed, then the scaling is more complicated at low energy, but quickly goes over to a $\gamma_0^{3/2}$ scaling as γ_0 increases. From Eq. (32), we see that the growth rate Γ_0 also shrinks as $\gamma_0^{3/2}$. Therefore, if the beam is stable just above the transition energy, then it will tend to remain so as the acceleration proceeds. In addition, both sides of Eq. (38) scale linearly with ℓ , so that if one mode is stable then all modes are. As we shall see in Sec. 6.1, this scaling breaks down for large ℓ -numbers.

6. COMPARISON WITH NUMERICAL SIMULATIONS

In order to check the analytic theory, and to study the nonlinear effects of the instability, we carried out a limited number of simulations using the three-dimensional particle-in-cell code IVORY. IVORY has been used successfully to model the negative-mass instability in the modified betatron [8, 13]. The code is fully electromagnetic and advances the complete Lorentz force equations for the particles. A two-dimensional grid is used to represent the transverse plane of the beam, while fields in the toroidal direction are represented by a Fourier sum. This allows us to compare predictions for individual ℓ -numbers directly with theory. For economy, we generally keep ≤ 3 toroidal modes in the simulations. To model the solenoidal lens betatron, a sinusoidally varying toroidal field is used. We use Eq. (10), with $B_{\theta s}^2/\gamma_0^2$ is replaced by $\langle B_{\theta s}^2/\gamma_0^2 \rangle$, to obtain suitable equilibria to initialize the simulations. We find that small-amplitude envelope oscillations are excited due to the fact that the cusps are not infinitely sharp [15].

6.1 IAPBT PARAMETERS

Three simulations were performed for the for the parameters in Table 1. We assumed 30 solenoids around the torus since 10 of the 40 solenoids in the actual device are on straight sections which we do not simulate here. First, we looked at the $\ell = 5$ mode at $\gamma_0 = 3$. The beam radius was chosen to be 1.75 cm, for which the matched amplitude of the solenoidal field is 134 gauss. The simulation was run for 230 ns, during which no measurable growth was observed. The theoretically predicted growth rate is $22.8 \mu s^{-1}$, which would have produced about 5.3 e-foldings in 230 ns. (This growth rate is higher than those shown in Fig. 3 because of the lower solenoidal field.) We attribute the beam stability to the spread in circulation frequencies. The right-hand side of Eq. (38) is $26.2 \mu s^{-1}$, which is marginally sufficient for stability.

The averaging procedure of Sec. 4 breaks down as the mode-number ℓ approaches the mode-number ℓ_s associated with the solenoidal field. For our case, $\ell_s = 15$. Since no averaging is used in the simulation code, however, such modes can be looked at numerically. For the same parameters as the $\ell = 5$ simulation above, we performed a simulation of the $\ell = \ell_s = 15$ mode. We observed a strong instability, with a growth rate of $66 \mu s^{-1}$, as shown in Fig. 6. A particle plot from the nonlinear stage of the instability (Fig. 7) shows typical negative-mass instability behavior, i.e., radial kinking accompanied by toroidal clumping. The instability has almost saturated at the point reached in Fig. 7, but 1/6 of the current has been scraped off onto the wall. If the wall radius had been larger, the instability might have saturated without current loss.

If we naively apply the analytic dispersion relation to the $\ell = 15$ mode, we obtain a growth rate of $66 \mu s^{-1}$, the same as the numerical result. However, Eq. (38) predicts stability due to frequency spread. Thus, it appears that the zero-frequency-spread growth rate for $\ell = 15$ is significantly larger than that predicted by analytic theory. On the other hand,

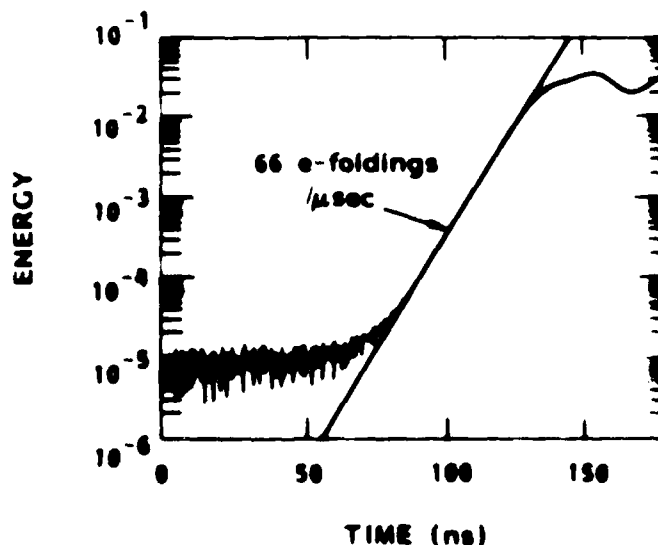


Figure 6. Energy history of the $\ell = 15$ mode in a simulation of a 100 A, $\gamma_0 = 3$ beam, showing the linear growth and nonlinear saturation.

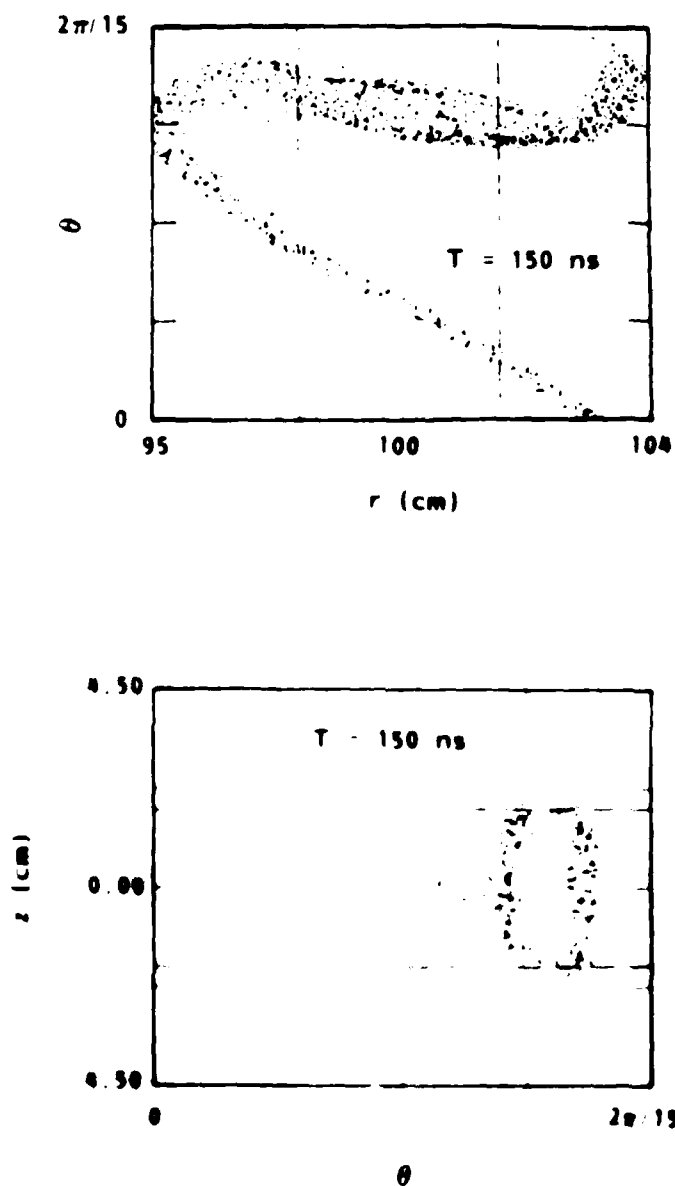


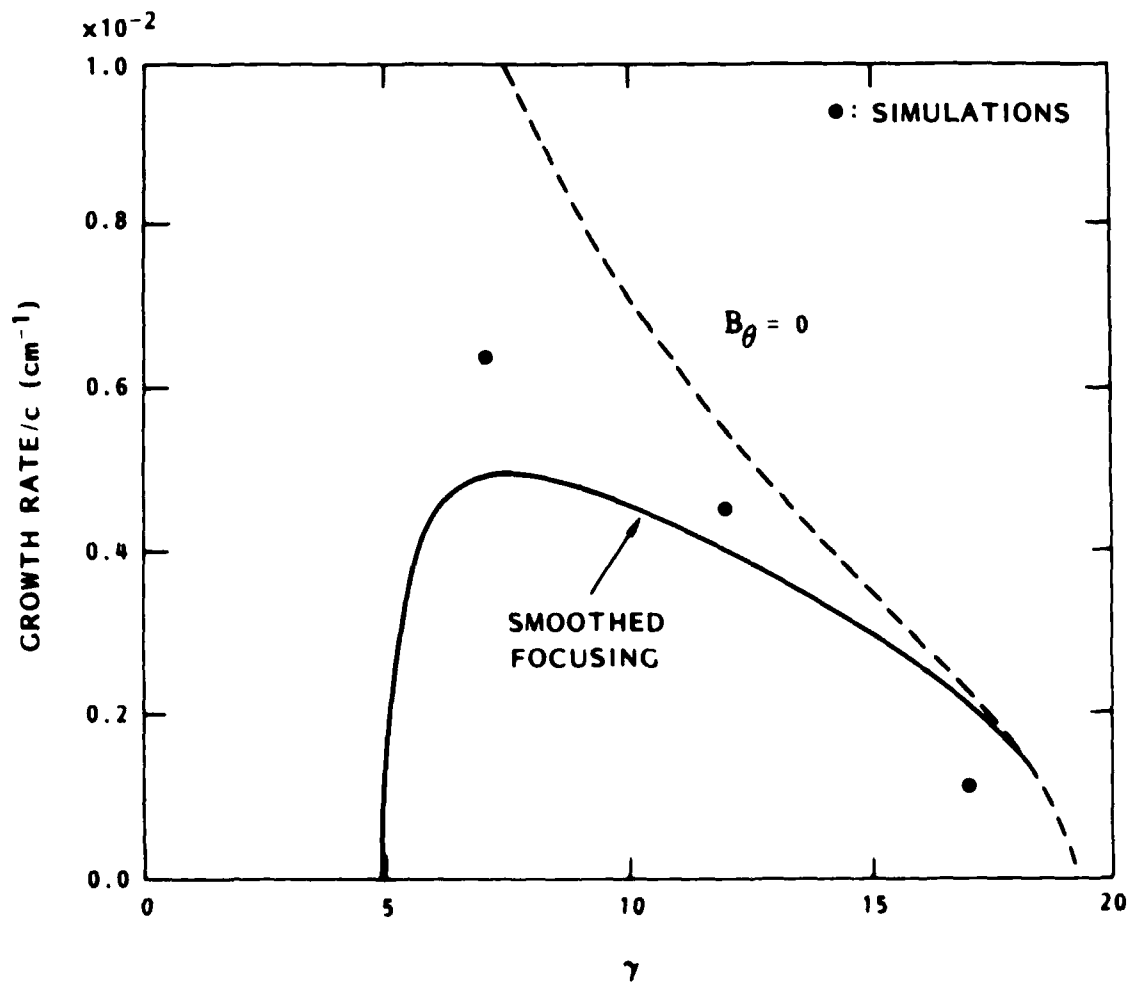
Figure 7. Particle plots (r - θ , z - θ) taken during the nonlinear state of the $l = 15$ negative-mass instability on a 100 A, $v_0 = 3$ beam. The dashed lines show the location of the toroidally uniform beam at the start of the simulation.

the analytic prediction of a negative-mass transition energy appears to be valid even for $l = 15$. We simulated this mode for $\gamma_0 = 1.6$, which corresponds to the injection energy of the IAPBT betatron, and observe no instability. The analytic theory predicts stability up to at least $\gamma_0 = 2.2$ (see Fig. 3).

6.2 HIGH-CURRENT BEAM STABILITY

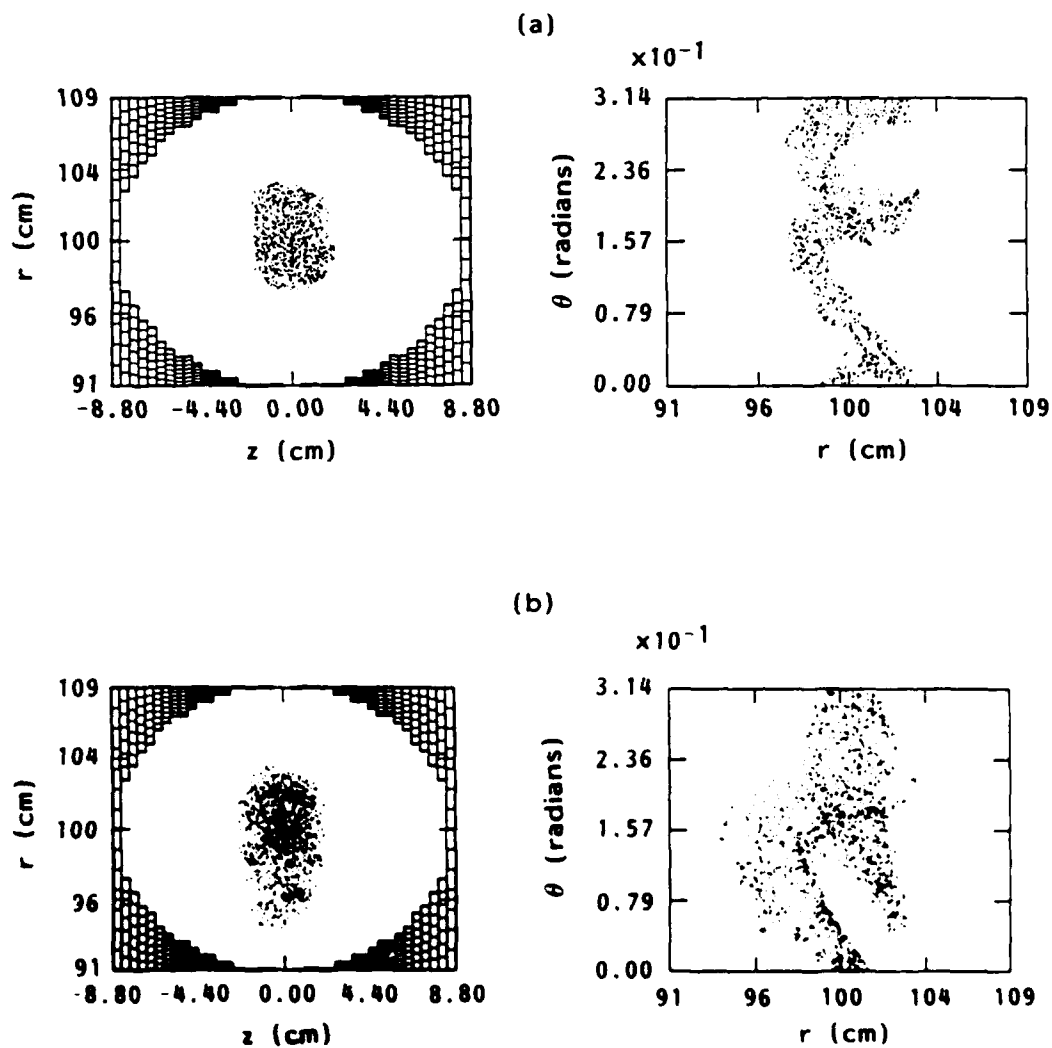
If experiments at 100 A are successful, then higher-current experiments will be undertaken. We have performed three simulations of 10 kA beams to investigate beam stability at high current. We assumed 20 solenoids around a torus with a 1 m major radius, and simulated the mode $l = 2$ $l_s = 20$ (this mode was chosen for reasons of computational economy). In Fig. 8, we compare the simulation results with (a) growth rates obtained for a conventional betatron (no toroidal field) and (b) growth rates obtained by using the averaged approximation for the solenoidal lenses. Because of the high l -number, the curves in Fig. 8 were obtained by inserting Eq. (28) into the exact analytic dispersion relation of Ref. (13) rather than using Eq. (31). In doing the simulations, we set the beam radius to 2 cm in order to have good resolution of the beam on the simulation mesh. This means that the solenoidal field necessary to get a matched beam decreases as the beam energy increases (see Eq. 39). Thus the simulation growth rates shown in Fig. 8 do not represent those experienced by an accelerating beam where the solenoidal field is kept constant, or increased.

As in the 100 A simulations, we find that the high- l growth rates are anomalously large when frequency spread effects are taken into account. Nevertheless, the simulations for $\gamma_0 = 7$, and $\gamma_0 = 12$ both saturate with no loss of current. Plots from the nonlinear stage of these simulations are shown in Fig. 9. There is considerable churning of the beam after these plots were taken, and this stage of the instability is probably not well modeled with a few Fourier modes. The simulation at $\gamma_0 = 17$ was not run long enough to see saturation.



R-922

Figure 8. Growth rates of the $l = 20$ negative-mass mode on a 10 kA beam in a solenoidal-lens betatron, plotted versus beam energy. Growth rates are compared to those for a conventional betatron (dashed line) and those obtained using the averaged-focusing approximation (solid line).



R-922

Figure 9. Particle plots (r - z , r - θ) taken during the nonlinear saturation of the $l = 20$ mode on a 10 kA beam. The beam energy is $\gamma_0 = 7$ in (a), and $\gamma_0 = 12$ in (b).

7. SUMMARY AND DISCUSSION

We have presented an analytic model for the negative-mass instability in the solenoidal-lens betatron. Restricting the analysis to low toroidal mode-numbers, the effect of the solenoidal lenses are averaged over using a multiple-length-scale method. The equations obtained are those of the conventional negative-mass dispersion relation with a modified transverse focusing force. The additional transverse focusing introduces a finite negative-mass transition energy below which the beam is stable. Above this energy, growth rates are suppressed relative to those of the conventional betatron.

The averaged transverse focusing term is used to obtain a kinetic dispersion relation for the solenoidal lens betatron. We find that for a space-charge-dominated equilibrium, it is relatively easy to stabilize the instability with the natural frequency spread due to finite beam radius. This contrasts with other types of betatrons where an energy spread is needed to produce a significant frequency spread.

Results of three-dimensional PIC code simulations of the IAPBT betatron are in agreement with the predicted stability for low k -numbers where the averaging procedure is applicable. For a mode-number equal to the mode-number of the solenoidal lenses, on the other hand, we find that the growth rate is anomalously large. In the nonlinear regime, the instability exhibits a classical wave-breaking saturation mechanism leading to some loss of current.

The prediction of a finite negative-mass transition energy is borne out by the simulation results even for large k -numbers. Thus, the IAPBT betatron is predicted to be stable at its injection energy even in the absence of particle frequency spread.

High-current simulations at high mode-number show large growth rates comparable to what one would obtain in the absence of any toroidal field (i.e., a conventional betatron). However, no current loss is observed during the nonlinear saturation of the instability.

REFERENCES

1. F. Mako, J. Golden, L. Floyd, K. McDonald, T. Smith, and C. A. Kapetanakis, IEEE Trans. Nuc. Sci. NS-32, 3027 (1985).
2. H. Ishizuka, G. Lindley, B. Mandelbaum, A. Fisher, and N. Rostoker, Phys. Rev. Lett. 53, 266 (1984).
3. H. Ishizuka, J. Saul, A. Fisher, and N. Rostoker, Proc. 6th International Conference on High-Power Particle Beams, p. 722 (Kobe, Japan, 1986).
4. A. A. Mondelli and C. W. Roberson, Part. Accel. 15, 221 (1984).
5. S. Humphries, Jr. and D. M. Woodall, Bull. Am. Phys. Soc. 28, 1054 (1983). S. Humphries, Jr., L. K. Len, and C. B. Allen, Rev. Sci. Instrum., to be published.
6. D. W. Kerst and R. Serber, Phys. Rev. 60, 53 (1941).
7. R. W. Landau and V. K. Neil, Phys. Fluids 9, 2412 (1966).
8. B. B. Godfrey and T. P. Hughes, Phys. Fluids 28, 569 (1985).
9. P. Sprangle and D. Chernin, Part. Accel. 15, 35 (1984).
10. D. Chernin, Phys. Fluids 29, 556 (1986).
11. J. D. Lawson, The Physics of Charged Particle Beams (Clarendon, Oxford, 1978).
12. A. Mondelli and D. Chernin, Bull. Am. Phys. Soc. 29, 1431 (1984).
13. B. B. Godfrey and T. P. Hughes, Part. Accel. 21, 173 (1987).
14. H. S. Uhm, R. C. Davidson, and J. J. Petillo, Phys. Fluids, 28, 2537 (1985).
15. T. P. Hughes and B. B. Godfrey, IEEE Trans. Nuc. Sci. NS-32, 2498 (1985).

APPENDIX D

PUBLICATIONS, TECHNICAL REPORTS, CONFERENCE PROCEEDINGS, AND
PRESENTATIONS WRITTEN UNDER THIS CONTRACT

AD-A182 021

RECIRCULATING ACCELERATOR STUDIES(U) MISSION RESEARCH
CORE ALBUQUERQUE NM Y P HUGHES ET AL. 02 JUN 87
AMRC-R-922 N00014-84-C-0078

2/2

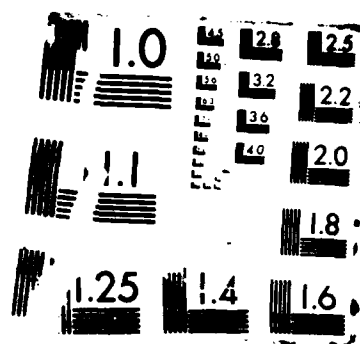
UNCLASSIFIED

F/G 20/7

NL



1-1-1
1-1-1
1-1-1



PUBLICATIONS

"Stability of the Solenoidal Lens Betatron," T. P. Hughes, submitted to Part. Accel., 1987.

"An Improved Negative-Mass-Instability Dispersion Relation for High-Current Modified Betatrons," B. B. Godfrey and T. P. Hughes, Part. Accel. 21, 173, 1987.

"Electromagnetic Instability in a Quadrupole-Focusing Accelerator," T. P. Hughes and B. B. Godfrey, Phys. Fluids 29, 1698, May 1986.

"Long-Wavelength Negative-Mass Instabilities in High Current Betatrons," B. B. Godfrey and T. P. Hughes, Phys. Fluids 28, 669, 1985.

"Instability in an E-Layer With A Strong Azimuthal Magnetic Field," T. P. Hughes and B. B. Godfrey, App. Phys. Lett. 46, 473, 1985.

TECHNICAL REPORTS

"High Current Electron Beam Transport in Recirculating Accelerators," Brendan B. Godfrey and Thomas P. Hughes, AMRC-R-842, NATO Advanced Study Institute (Pitlochry, Scotland), July 1986.

"Estimates of Negative-Mass Instability Growth for the NRL Betatron," T. P. Hughes, AMRC-N-327, 1985.

"Final Report - Modified Betatron Accelerator Studies," T. P. Hughes and B. B. Godfrey, AMRC-R-655, November 1984.

"Single-Particle Orbits in the Stelleron Accelerator," T. P. Hughes and B. B. Godfrey, AMRC-N-284, November 1984.

"Improved Long-Wavelength Dispersion Relation for the Negative Mass Instability in High Current Conventional and Modified Betatrons," B. B. Godfrey and T. P. Hughes, AMRC-R-520, November 1983.

"Stelleron Calculations," T. P. Hughes, B. B. Godfrey, and M. M. Campbell, AMRC-N-251, November 1983.

"Toroidal Self-Field Corrections to the Linear Dispersion Relation for the Negative Mass Instability in a Modified Betatron," B. B. Godfrey, T. P. Hughes, and M. M. Campbell, AMRC-N-249, November 1983.

"Simulations and Theory of Negative Mass Instability in Modified Betatron Accelerators," T. P. Hughes, M. M. Campbell, and B. B. Godfrey, AMRC-N-247, November 1983.

CONFERENCE PROCEEDINGS

"High-Current Electron Beam Transport in Recirculating Accelerators," B. Godfrey and T. Hughes, Proceedings of NATO Advanced Study Institute on High Brightness Accelerators (to be published by Plenum).

"Theory and Simulation of High Current Betatrons," T. P. Hughes, Proceedings of 6th International Conference on High-Power Particle Beams, Kobe, Japan, 1986, p. 815.

"Equilibrium and Stability of the Solenoidal Lens Betatron," T. P. Hughes and B. B. Godfrey, IEEE Trans. Nuc. Sci. NS-32, 2498, 1985.

"Negative-Mass Instability in High-Current Modified Betatrons at Low Energies," B. B. Godfrey and T. P. Hughes, IEEE Trans. Nuc. Sci. NS-32, 2495, 1985.

"Linear and Nonlinear Development of the Negative Mass Instability in a Modified Toroidal Betatron Accelerator," T. P. Hughes, M. M. Campbell, and B. B. Godfrey, Proceedings of Fifth International Conference on High-Power Particle Beams, p. 466 (San Francisco), 1983.

"Analytical and Numerical Studies of the Modified Betatron," T. P. Hughes, B. B. Godfrey, and M. M. Campbell, IEEE Nuc. Sci. 30, 2528-2530, 1983.

CONFERENCE PRESENTATIONS

"Theory and Numerical Simulation of High Current Betatrons," T. P. Hughes, APS Plasma Physics Meeting, 1-5 November 1986, Baltimore, MD (Invited Talk).

"A Negative Mass Stabilization Mechanism for the Modified Betatron," B. B. Godfrey, APS Plasma Physics Meeting, 1-5 November 1986, Baltimore, MD.

"High Current Electron-Beam Transport in Recirculating Accelerators," B. B. Godfrey, NATO Advanced Study Institute, 13-15 July 1986, Pitlochry, Scotland (Invited Talk).

"Theory and Simulations of High Current Betatrons," T. P. Hughes, Beams '86 Conference, 9-12 June 1986, Kobe, Japan.

"Effect of Straight Sections on Stability of Recirculating Accelerators," T. P. Hughes, APS Plasma Physics Meeting, 4-8 November 1985, San Diego, CA.

"Use of a 3-D Simulation Code in the Study of High Current Recirculating Accelerators," B. B. Godfrey, Compact Accelerator Workshop, 23-24 October 1985, Livermore, CA.

"Negative Mass Instability in High Current Modified Betatrons at Low Energies," B. B. Godfrey, and "Equilibrium and Stability of the Solenoidal Lens Betatron," T. P. Hughes, 1985 Particle Accelerator Conference, 13-16 May 1985, Vancouver, BC.

"Stabilization of Negative Mass Instability in the Modified Betatron," T. P. Hughes, APS Plasma Physics Meeting, 29 October - 2 November 1984, Boston, MA.

"Toroidal Self-Field Corrections to the Linear Dispersion Relation for the Negative Mass Instability in a Modified Betatron," B. B. Godfrey, and "Simulations and Theory of the Negative Mass Instability in a Modified Betatron," T. P. Hughes, APS Plasma Physics Meeting, 7-11 November 1983.

**DATA
FILM**